

**Explicit Asymptotic Solutions of $\nu_e + e^-$
Neutrino Networks for Large Sets of
Partial Differential Equations in
Core-Collapse Supernovae**

A Thesis Presented for the
BACHELOR OF SCIENCE IN PHYSICS
THE UNIVERSITY OF TENNESSEE, KNOXVILLE

Raghav Chari

Defended April 19, 2024



© by Raghav Chari, 2024
All Rights Reserved.

Dedication ...

To my friends and family, for their unwavering support, love, and the belief that I could pursue my passion. Special thanks to the endless support my Mother, Father and Savannah Bedell. Most of all to my older brother, Rohith Chari, for his guidance, support, and belief in me.

Acknowledgements

I would like to thank the University of Tennessee, Knoxville's Department of Physics & Astronomy for their support and to all the outstanding professors and mentors within the Department. I am particularly thankful to Dr. Sean Lindsay, whose immense support and guidance has been paramount to my education. I would also like to thank Dr. Eirik Endeve and Dr. Vassilios Mewes from Oak Ridge National Laboratories for their support and guidance throughout my research. I am also deeply grateful to Ph.D. students Adam Cole and Nick Brey for their support and mentorship over the three years of this project. Their contributions have been instrumental to my growth and success. Additionally, I wish to acknowledge Olivia Clark, whose assistance in data analysis has played a critical role in the completion of this project. Most of all I would like to thank Dr. Mike Guidry for the opportunity to work on this project and for his support and guidance as my advisor. This work was also made possible through generous funding from several sources, which have been instrumental to the advancement of this research:

Chari R., Guidry M. (2024). *Enhancing Astrophysical Modeling: Integrating WEAKLIB with Fast Explicit Neutrino Networks for Advanced Large Scale Neutrino Electron Scattering*, Advanced Undergraduate Research Activity (AURA).

Chari R., Guidry M. (2021). *New Approaches to Astrophysical Nucleosynthesis and Neutrino Transport*, Fellowship, Department of Physics and Astronomy, University of Tennessee, Knoxville.

Chari R. (2022, 2023). Undergraduate Research & Fellowships Travel Grants, University of Tennessee, Knoxville.

Abstract

In physics, accurately modeling large-scale phenomena such as core-collapse supernovae, (CCSN), and neutron star mergers are computationally challenging and require solving large sets of partial and ordinary differential equations. Traditional methods used widely in the scientific community are predominantly implicit, which are approximations that often require drastic simplifications and can be computationally inefficient. This thesis presents results on a new software suite titled “Fast Explicit Neutrino Networks” or “FENN”, that introduces a suite of algebraically stabilized explicit methods known as explicit asymptotic for modeling Neutrino Electron Scattering, (NES), presenting a novel approach that combines the stability of traditional methods with enhanced computational efficiency. Initial results show that FENN can deliver accurate solutions for neutrino networks at improved computational speeds. This thesis further covers new results for scaled networks beyond the constraints of standard energy groupings, as well as the dynamics of neutrino interactions such as the scattering of various neutrino flavors—electron neutrinos (ν_e), electron anti-neutrinos ($\bar{\nu}_e$), and muon/tau neutrinos ($\nu_{\mu,\tau}$) as well as their anti-particles ($\bar{\nu}_{\mu,\tau}$)—off electrons.

Contents

List of Tables	viii
List of Figures	ix
1 Introduction	1
2 Mathematical Formulation	4
2.1 Neutrino Electron Scattering	4
2.1.1 Formulation of Neutrino-Electron Scattering	4
2.1.2 Weak Interaction	5
2.1.3 Constructing Energy Bins	7
2.1.4 Matrix Formulation of the NES Model	10
3 Numerical Integration	12
3.1 Numerical Integration Methods for Neutrino Distribution	12
3.1.1 Explicit Asymptotic Method	12
3.1.2 Explicit Forward Euler Algorithm	14
3.1.3 Backward Euler Method	15
4 Integration of WeakLib and FENN	16
4.1 Pipeline Algorithms	16
4.1.1 Data Reading and Transformation	18
4.1.2 Treatment of Φ_{In}	18
4.1.3 Equilibrium Distribution Initialization	19
4.2 Newton-Raphson Method Implementation for Neutrino Scattering Simulations	19
4.2.1 Jacobian Matrix Computation	19
4.2.2 Right-Hand Side Computation	20
4.2.3 Newton-Raphson Iteration	20

4.2.4	Timestep Functions	20
5	Tradeoff of Speed and Accuracy	23
5.1	Single Models	23
5.1.1	Heatmaps	24
5.1.2	A Quantitative Measure of Speed	29
5.2	Energy Grid Definitions	30
5.3	Model Analysis	31
5.3.1	Model 81 Analysis	31
5.3.2	Model 186 Analysis	37
5.3.3	Model 213 Analysis	44
5.3.4	Speed vs Accuracy	50
6	Neutrino Flavors	52
6.1	Introduction to Neutrino Flavors and Electron Scattering	52
6.1.1	$\bar{\nu}_e + e^-$ Scattering	52
6.1.2	$\bar{\nu}_{\mu,\tau} + \mu^-, \tau^-$ Scattering	56
6.1.3	$\nu_{\mu,\tau} + \mu^-, \tau^-$ Scattering	59
7	Scaling with Network Size	63
7.1	Analysis of Scaled Networks	63
7.1.1	Network Size 40	64
7.1.2	Network Size 50	65
7.1.3	Network Size 80	67
7.1.4	Network Size 100	68
7.1.5	Network Size 130	70
7.1.6	Network Size 160	71
7.1.7	Network Size 180	73
8	Conclusion	81
	Bibliography	83
	A Supernova Conditions	86
	Vita	95

List of Tables

5.1	Summary of steps and error for Model 81.	36
5.2	Summary of steps and error for Model 186.	44
5.3	Summary of steps and error for Model 213.	50
5.4	Tolerance Conditions (TolC) for Each Model and Case.	50
5.5	Summary of wall clock times for Models 81, 186, 213	51
7.1	Comparison of Explicit Asymptotic and Backward Euler Steps with Error across Network Sizes.	75
7.2	Comparison of simulation times for explicit asymptotic and LU solver methods across network sizes.	76
7.3	Comparison of computational time and speed up factor for different network sizes . .	76
7.4	Comparison of Simulation Times for Different Implicit Solvers across Network Sizes.	77
	Supernova Conditions	86
A.2	Energy Grid for a 50-Species Network.	93
A.3	Energy Widths for a 50-Species Network.	94

List of Figures

2.1	WeakLib opacities adopted from (Bruenn, 1985).	7
4.1	WeakLib to FENN Integration.	17
4.2	InitializePipelineNES algorithm	18
4.3	The ComputeNextTimeStep function modifies the time step dynamically, responding to the ratio of energy output to energy demand ($E_O \rightarrow E_D$). It reduces the time step when this ratio is too high to preserve the accuracy of the simulation, and it expands the time step when the ratio is low to enhance efficiency.	21
4.4	The computeTimeStep EA function employs an environmental assessment approach, adjusting the time step according to the total changes observed over a time step compared to a predefined tolerance. This method allows the function to modify the time step to maintain simulation precision within set limits.	22
5.1	Dynamics of Model 186 showing Number Density N_i across 40 energy bins vs time and time step vs time. The calculation referenced took 323 explicit steps.	24
5.2	Model 81 Heatmap	25
5.3	Model 186 Heatmap	26
5.4	Model 213 Heatmap	27
5.5	Φ_{In} for one Energy Level	28
5.6	Energy Grid for a 50-species network. Energies are logarithmically spaced from 1–300 MeV.	30
5.7	Energy Widths	31
5.8	Population vs time for Model 81 - Accurate Case.	32
5.9	RMS vs time for Model 81 - Accurate Case.	32
5.10	Time step vs time for Model 81 - Accurate Case.	33
5.11	Population vs time for Model 81 - Intermediate Case.	33
5.12	RMS vs time for Model 81 - Intermediate Case.	34

5.13	Time step vs time for Model 81 - Intermediate Case.	34
5.14	Population vs time for Model 81 - Fast Case.	35
5.15	RMS vs time for Model 81 - Fast Case.	35
5.16	Time step vs time for Model 81 - Fast Case.	36
5.17	Population vs time for Model 186 - Accurate Case.	38
5.18	RMS vs time for Model 186 - Accurate Case.	39
5.19	Timestep vs time for Model 186 - Accurate Case.	39
5.20	Population vs time for Model 186 - Intermediate Case.	40
5.21	RMS vs time for Model 186 - Intermediate Case.	41
5.22	Timestep vs time for Model 186 - Intermediate Case.	41
5.23	Population vs time for Model 186 - Fast Case.	42
5.24	RMS vs time for Model 186 - Fast Case.	43
5.25	Timestep vs time for Model 186 - Fast Case.	43
5.26	Population vs time for Model 213 - Accurate Case.	44
5.27	RMS vs time for Model 213 - Accurate Case.	45
5.28	Time step vs time for Model 213 - Accurate Case.	45
5.29	Population vs time for Model 213 - Intermediate Case.	46
5.30	RMS vs time for Model 213 - Intermediate Case.	47
5.31	Time step vs time for Model 213 - Intermediate Case.	47
5.32	Population vs time for Model 213 - Fast Case.	48
5.33	RMS vs time for Model 213 - Fast Case.	49
5.34	Time step vs time for Model 213 - Fast Case.	49
6.1	Population vs time for Model 186 - TolC = 10^{-4}	53
6.2	RMS vs time for Model 186 - TolC = 10^{-4}	53
6.3	Time step vs time for Model 186 - TolC = 10^{-4}	54
6.4	Heatmap of Scattering Rates for $\bar{\nu}_e + e^-$	55
6.5	Population vs time for Model 186 - TolC = 10^{-4}	56
6.6	RMS vs time for Model 186 - TolC = 10^{-4}	57
6.7	Time step vs time for Model 186 - TolC = 10^{-4}	57
6.8	Heatmap of Scattering Rates for $\bar{\nu}_{\mu,\tau} + \mu^-, \tau^-$	58
6.9	Population vs time for Model 186 - TolC = 10^{-4}	59
6.10	RMS vs time for Model 186 - TolC = 10^{-4}	60
6.11	Time step vs time for Model 186 - TolC = 10^{-4}	60
6.12	Heatmap of Scattering Rates for $\nu_{\mu,\tau} + \mu^-, \tau^-$	61

7.1	Population vs. time for Network Size 40.	64
7.2	Epsilon vs. time for Network Size 40.	64
7.3	Timestep vs. time for Network Size 40.	65
7.4	Population vs. time for Network Size 50.	65
7.5	Epsilon vs. time for Network Size 50.	66
7.6	Timestep vs. time for Network Size 50.	66
7.7	Population vs. time for Network Size 80.	67
7.8	Epsilon vs. time for Network Size 80.	67
7.9	Timestep vs. time for Network Size 80.	68
7.10	Population vs. time for Network Size 100.	68
7.11	Epsilon vs. time for Network Size 100.	69
7.12	Timestep vs. time for Network Size 100.	69
7.13	Population vs. time for Network Size 160.	70
7.14	Epsilon vs. time for Network Size 160.	70
7.15	Timestep vs. time for Network Size 160.	71
7.16	Population vs. time for Network Size 160.	71
7.17	Epsilon vs. time for Network Size 160.	72
7.18	Timestep vs. time for Network Size 160.	72
7.19	Population vs. time for Network Size 180.	73
7.20	Epsilon vs. time for Network Size 180.	73
7.21	Heat map of Scattering Rates for a 180 Size Network	74
7.22	Full wall clock times. Includes times for different implicit solvers, along with polynomial fits to show the trends for each method.	77
7.23	Full wall clock times from 7.22 with polynomial Fits for the first 3 points.	78
7.24	LU solver vs. explicit method comparison. LU solver is used in all calculations from 7.	78
7.25	Full simulation time vs. network Size squared. This can represent the computational cost and general trends for Network Sizes.	79

Chapter 1

Introduction

Realistic simulations of core-collapse supernovae and stellar explosions involve solving sets of non-linear partial and ordinary differential equations related to hydrodynamics, radiation transport, and thermonuclear reactions. This gives stiff systems that are computationally challenging and requires careful choice of numerical methods to make them efficient. (Oran and Boris, 2005; Gear, 1971; Lambert, 1991; Press et al., 1992).

Explicit numerical methods, therefore, are usually simple as they calculate based on the present states without information about future states. Alternatively, implicit methods are typically based on predictions of the states to be made in future iterations and require complex matrix inversions that are computationally expensive.

When it comes to realistic astrophysical systems, explicit methods such as forward Euler struggle with stiff systems of differential equations. This is due to the stability constraints of the method that impose very small timesteps, which are impractical in large-scale simulations.

In a series of papers, the explicit asymptotic method was applied to thermonuclear networks (Guidry, 2012; Guidry et al., 2013b,a; Guidry and Harris, 2013; Guidry et al., 2023; Guidry, 2016; Haidar et al., 2015, 2016; Brey, 2022; Chupryna, 2008; Feger, 2011).

Specifically, in (Guidry, 2012) we can consider the following equations:

$$\begin{aligned}\frac{dy_i}{dt} &= F_i^+ - F_i^- \\ &= (f_1^+ + f_2^+ + \dots)_i - (f_1^- + f_2^-)_i \\ &= (f_1^+ - f_1^-)_i + (f_2^+ - f_2^-)_i + \dots = \sum_j (f_j^+ - f_j^-)_i\end{aligned}\tag{1.1}$$

where $y_i (i = 1 \dots N)$ are species, and t is time. We can denote the fluxes between species i and j by $(f_j^\pm)_i$, and the sum for each variable i for all variables j coupled to i by a non-zero flux $(f_j^\pm)_i$.

Therefore, for an N -species network there will be N equations in the populations y_i . Here (Guidry, 2012) applies an explicit approximation known as the explicit asymptotic to method to Eq. 1.1. Given the differential equations in the form

$$F_i^- = (k_1^i + k_2^i + \dots + k_m^i)y_i \equiv k^i y_i, \quad (1.2)$$

where k_j^i are rate parameters (with the subscript m indicating the total number of these processes) for processes depleting y_i . $\tau_j^i = 1/k_j^i$ are the characteristic timescales defined for this set of equations, the effective total depletion rate and corresponding timescale are

$$k^i \equiv \frac{F_i^-}{y_i}, \quad \tau^i = \frac{1}{k^i}. \quad (1.3)$$

Thus, at timestep t_n the finite-difference approximation is

$$y_i(t_n) = \frac{F_i^+(t_n)}{k^i(t_n)} - \frac{1}{k^i(t_n)} \left. \frac{dy_i}{dt} \right|_{t=t_n}. \quad (1.4)$$

The asymptotic limit where $F_i^+ \simeq F_i^-$ gives the first approximation $y_i^{(1)}(t_n)$ and local error $E_n^{(1)}$,

$$y_i^{(1)}(t_n) = \frac{F_i^+(t_n)}{k^i(t_n)}, \quad E_n^{(1)} \equiv y(t_n) - y^{(1)}(t_n) = -\frac{1}{k(t_n)} \frac{dy}{dt}(t_n). \quad (1.5)$$

For small dy_i/dt , the correction term is

$$\frac{dy}{dt}(t_n) = \frac{1}{\Delta t} (y_i(t_n) - y_i(t_{n-1})) + \frac{1}{\Delta t} (E_n^{(1)} - E_{n-1}^{(1)}) + O(\Delta t). \quad (1.6)$$

Here, $O(\Delta t)$ represents the higher-order terms in the expansion, which are proportional to Δt . These terms are significant when Δt is large, but as Δt approaches zero, their contribution diminishes. This leads to:

$$y_n^{(2)} = \frac{1}{1 + k_n \Delta t} (y_{n-1} + F_n^+ \Delta t), \quad (1.7)$$

for large $k\Delta t$. Implementing an asymptotic algorithm requires defining a critical value κ of $k\Delta t$:

1. If $k^i \Delta t < \kappa$, update the population numerically by the explicit Euler method.
2. If $k\Delta t \geq \kappa$, update the population algebraically using the provided approximation.

The stability of the integration is contingent upon the condition $k^i \Delta t < 1$, with $\kappa = 1$ chosen for demonstration.

However, in this thesis, we will apply them to scaled neutrino networks (larger than standard network sizes) for, specifically, Neutrino Electron Scattering ($\nu_e + e^-$). Energy from neutrinos that are released during a core-collapse supernova is important for a large portion of the supernova. Further, it is believed that the neutrinos released during the core collapse contribute to the shock wave that propagates through the star. While most codes focus on the full neutrino matter interaction such as electron-positron pair creation and annihilation, emission and absorption on nucleons and nuclei, and scattering on nucleons and nuclei, the Neutrino Electron Scattering portion is a large enough portion of this that the results from these methods can be applied to the more general formulation of the neutrino transport problem.

In general, the entirety of the neutrino transport problem is difficult to simulate because of the weak interaction further described in section 2. Kinetic models are required that use the Boltzmann equation that depends on position and momentum coordinates in phase space. Due to the nature of this, implicit methods such as backward Euler are traditionally used.

In (Lackey-Stewart et al., 2024), we applied the explicit asymptotic algorithms (Guidry, 2012) by introducing a novel suite of computational algorithms known as Fast Explicit Neutrino Networks (FENN) that were shown to balance speed and accuracy for the explicit asymptotic methods at a fixed energy grid and bin size. Following this, in a subsequent study introduced for neutrino networks in (Chari et al., 2024), we expand on the foundational work by emphasizing the importance of scalability.

As of the writing of this thesis, scalability has not been applied to this problem in the same way (Guidry, 2012) has applied them in the context of reaction networks. In this thesis, we will compare our results to validate the fixed network sizes in (Lackey-Stewart et al., 2024), as well as extend them to network sizes up to 180 species.

Chapter 2

Mathematical Formulation

2.1 Neutrino Electron Scattering

(Bruenn, 1985) provides an extensive mathematical framework for the transport of neutrinos inside astrophysical core-collapse supernovae. The formulation in FENN will focus on Neutrino Electron Scattering (NES), which we now summarize.

2.1.1 Formulation of Neutrino-Electron Scattering

Let's begin with the basics,

$$\lambda^{(t)}(\omega) \rightarrow \Lambda^{(t)}(\omega) = \frac{3\lambda^{(t)}(\omega)}{3 + \lambda^{(t)}(\omega) |\nabla\psi^{(0)}(\omega)| / \psi^{(0)}(\omega)}, \quad (2.1)$$

Here $\lambda^{(t)}(\omega)$ is the modification of the mean free path, where the focus is on the right-hand side of the equation, which describes neutrino-electron scattering and thermal production terms. This can be simplified by expanding the kernels of these terms into a Legendre series and truncating after the first two terms

$$R_{\text{NES}}^{\text{in/out}}(\omega, \omega', \cos\theta) = \frac{1}{2} \sum_l (2l+1) \Phi_{l,\text{NES}}^{\text{in/out}}(\omega, \omega') P_l(\cos\theta), \quad (2.2)$$

Using this expansion, the quantities $A_{\text{NES}}^{(\alpha)}(\omega)$, $B_{\text{NES}}^{(\alpha)}(\omega)$, and $C_{\text{NES}}^{(\alpha)}(\omega)$ are expressed as:

$$A_{\text{NES}}^{(0)}(\omega) = -\frac{2\pi}{c(2\pi\hbar c)^3} \int_0^\infty \omega'^2 d\omega' \left\{ \Phi_{0,\text{NES}}^{\text{in}}(\omega, \omega') \psi^{(0)}(\omega') + \Phi_{0,\text{NES}}^{\text{out}}(\omega, \omega') [1 - \psi^{(0)}(\omega')] \right\}, \quad (2.3)$$

$$B_{\text{NES}}^{(0)}(\omega) = -\frac{2\pi}{3c(2\pi\hbar c)^3} \int_0^\infty \omega'^2 d\omega' [\Phi_{1,\text{NES}}^{\text{in}}(\omega, \omega') - \Phi_{1,\text{NES}}^{\text{out}}(\omega, \omega')] \psi^{(1)}(\omega'), \quad (2.4)$$

$$C_{\text{NES}}^{(0)}(\omega) = \frac{2\pi}{c(2\pi\hbar c)^3} \int_0^\infty \omega'^2 d\omega' \Phi_{0,\text{NES}}^{\text{in}}(\omega, \omega') \psi^{(0)}(\omega'). \quad (2.5)$$

For the isoenergetic scattering kernel, a similar expansion yields

$$R_{\text{IS}}^0(\omega, \omega, \cos \theta) \approx \frac{1}{2} \Phi_{0,\text{IS}}(\omega) + \frac{3}{2} \Phi_{1,\text{IS}}(\omega) \cos \theta. \quad (2.6)$$

Finally, the $B_{\text{IS}}^{(1)}(\omega)$ is given by:

$$B_{\text{IS}}^{(1)}(\omega) = \frac{2\pi}{c(2\pi\hbar c)^3} \omega^2 [\Phi_{1,\text{IS}}(\omega) - \Phi_{0,\text{IS}}(\omega)]. \quad (2.7)$$

NES involves the exchange of charged (M_w) and neutral (M_z) bosons, leading to distinct matrix elements for electron-type neutrinos formulated later in this chapter.

2.1.2 Weak Interaction

The scattering process involving the exchange of charged (M_w) and neutral (M_z) bosons is described by

$$M_w = \frac{G}{\sqrt{2}} [\bar{u}_\nu(q') \gamma^\mu (1 - \gamma_5) u_e(p_e)] [\bar{u}_e(p'_e) \gamma_\mu (1 - \gamma_5) u_\nu(q)], \quad (2.8)$$

$$M_z = \frac{G}{\sqrt{2}} [\bar{u}_\nu(q') \gamma^\mu (1 - \gamma_5) u_\nu(q)] [\bar{u}_e(p'_e) \gamma_\mu (a - b\gamma_5) u_e(p_e)], \quad (2.9)$$

where $a = -\frac{1}{2} + 2\sin^2 \theta_w$, $b = -\frac{1}{2}$, and G is the weak interaction coupling constant. Combining these interactions, we obtain the total matrix element M as:

$$M = \frac{G}{\sqrt{2}} [\bar{u}_\nu(q') \gamma^\mu (1 - \gamma_5) u_\nu(q)] [\bar{u}_e(p'_e) \gamma_\mu (C_V - C_A \gamma_5) u_e(p_e)], \quad (2.10)$$

with $C_V = a + 1$ and $C_A = b + 1$. The transition rate for this process is given by

$$r = \frac{G^2}{\omega\omega'E_eE'_e} (2\pi)^4 \delta^4(q + p_e - q' - p'_e) \times \\ [(C_V + C_A)^2 p_e \cdot qp'_e \cdot q' + (C_V - C_A)^2 p'_e \cdot qp_e \cdot q' - M_e^2 (C_V^2 - C_A^2) q' \cdot q], \quad (2.11)$$

assuming the last term is negligible for relativistic electrons. The in and out scattering rates, $\Phi_{l,\text{NES}}^{\{\text{in},\text{out}\}}$, are derived from phase-space integration, yielding:

$$\Phi_{l,\text{NES}}^{\begin{cases} \text{in} \\ \text{out} \end{cases}} = \frac{G^2}{\pi\omega^2\omega'^2} \int dE_e F_e(E_e) [1 - F_e(E_e + \omega - \omega')] \left\{ \begin{array}{c} \exp[-\beta(\omega - \omega')] \\ 1 \end{array} \right\} \quad (2.12)$$

$$\times [(C_V + C_A)^2 H_l^{\text{I}}(\omega, \omega', E_e) + (C_V - C_A)^2 H_l^{\text{II}}(\omega, \omega', E_e)], \quad (2.13)$$

where H_l^{I} and H_l^{II} are functions detailed in (Yueh and Buchler, 1976).

The expression for $B_{\text{NES}}^{(1)}(\omega)$ is then given by:

$$B_{\text{NES}}^{(1)}(\omega) = -\frac{2\pi}{c(2\pi\hbar c)^3} \int_0^\infty \omega^2 d\omega' \left\{ \Phi_{0,\text{NES}}^{\text{in}}(\omega, \omega') \psi^{(0)}(\omega') + \Phi_{0,\text{NES}}^{\text{out}}(\omega, \omega') [1 - \psi^{(0)}(\omega')] \right\},$$

where $\omega', \omega, l, T, \eta$ are parameters, with $\eta = \mu_e/k_B T$. To interpolate the NES opacity on a consistent energy grid for ω and ω' within a given state (ρ_i, T_i, Y_{ei}) , it is necessary to interpolate for η first.

The NES tables are five-dimensional tables with $(\omega', \omega, l, T, \eta)$, where $\eta = \mu_e/k_B T$. We then interpolate the NES opacities at some ρ, T, Y_e detailed in Table A.

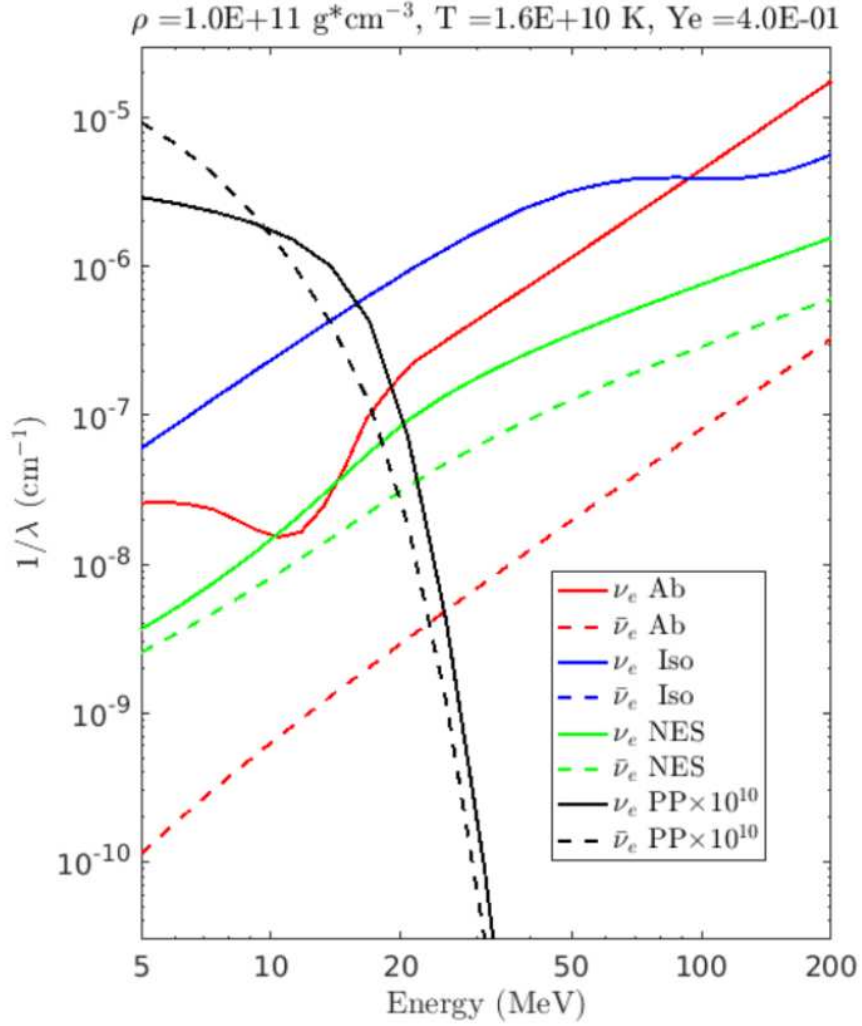


Figure 2.1: WeakLib opacities adopted from (Bruenn, 1985).

2.1.3 Constructing Energy Bins

In FENN, the model describes the evolution of the spectral neutrino number distribution within discretized energy bins, each characterized by a specific volume of phase space V . (Mezzacappa and Bruenn, 1993) demonstrated how realistic treatment of the NES influences the result. The underlying physics is governed by the spatially homogeneous Boltzmann equation, in this case modified to account for the inelastic neutrino-electron scattering, assuming constant background matter during

the processes of interaction. This formulation can be given by,

$$\frac{d\mathcal{F}}{dt} = (1 - \mathcal{F}) \int_{V_P} \mathcal{R}^{\text{in}}(\boldsymbol{\varepsilon}, \boldsymbol{\varepsilon}', \mathbf{n} \cdot \mathbf{n}'; \mathbf{u}) \mathcal{F}' dV_{P'} - \mathcal{F} \int_{V_P} \mathcal{R}^{\text{out}}(\boldsymbol{\varepsilon}, \boldsymbol{\varepsilon}', \mathbf{n} \cdot \mathbf{n}'; \mathbf{u}) (1 - \mathcal{F}') dV_{P'}, \quad (2.14)$$

where \mathcal{F} , the phase-space density, is normalized between $[0, 1]$, and $\mathcal{R}^{\text{in/out}}$ denote the transition rates into or out of an energy bin, influenced by the energy before and after collision, $\boldsymbol{\varepsilon}$ and $\boldsymbol{\varepsilon}'$, and the orientation of neutrino momenta through \mathbf{n} and \mathbf{n}' .

The scattering kernel approximation is given by (Smit and Cernohorsky, 1996)

$$\mathcal{R}^{\text{in/out}}(\boldsymbol{\varepsilon}, \boldsymbol{\varepsilon}', \cos \alpha, \mathbf{u}) \approx \sum_{\ell=0}^L \Phi_{\ell}^{\text{in/out}}(\boldsymbol{\varepsilon}, \boldsymbol{\varepsilon}', \mathbf{u}) P_{\ell}(\cos \alpha), \quad (2.15)$$

with the orthogonality relationship

$$\Phi_{\ell}^{\text{in/out}}(\boldsymbol{\varepsilon}, \boldsymbol{\varepsilon}', \mathbf{u}) = \frac{2\ell + 1}{2} \int_{-1}^1 \mathcal{R}^{\text{in/out}}(\boldsymbol{\varepsilon}, \boldsymbol{\varepsilon}', \cos \alpha, \mathbf{u}) P_{\ell}(\cos \alpha) d \cos \alpha. \quad (2.16)$$

Integrating the phase space density over all directions yields the neutrino number density

$$\mathcal{N}(\boldsymbol{\varepsilon}, \mathbf{x}, t) = \frac{1}{4\pi} \int_0^{2\pi} \int_0^{\pi} \mathcal{F} \sin \vartheta d\vartheta d\phi. \quad (2.17)$$

The isotropic scattering approximation leads to the following equation for the evolution of neutrino number density

$$\begin{aligned} \frac{d\mathcal{N}}{dt} = & (1 - \mathcal{N}) \int_{\mathbb{R}^+} \mathcal{R}^{\text{in}}(\boldsymbol{\varepsilon}, \boldsymbol{\varepsilon}') \mathcal{N}(\boldsymbol{\varepsilon}') dV_{\boldsymbol{\varepsilon}'} \\ & - \mathcal{N} \int_{\mathbb{R}^+} \mathcal{R}^{\text{out}}(\boldsymbol{\varepsilon}, \boldsymbol{\varepsilon}') (1 - \mathcal{N}(\boldsymbol{\varepsilon}')) dV_{\boldsymbol{\varepsilon}'}. \end{aligned} \quad (2.18)$$

Ensuring conservation and equilibrium, we have

$$\mathcal{R}^{\text{in}}(\boldsymbol{\varepsilon}, \boldsymbol{\varepsilon}') = \mathcal{R}^{\text{out}}(\boldsymbol{\varepsilon}', \boldsymbol{\varepsilon}), \quad (2.19)$$

$$\mathcal{R}^{\text{in}}(\boldsymbol{\varepsilon}, \boldsymbol{\varepsilon}') = \mathcal{R}^{\text{out}}(\boldsymbol{\varepsilon}', \boldsymbol{\varepsilon}) e^{\theta(\boldsymbol{\varepsilon}' - \boldsymbol{\varepsilon})}. \quad (2.20)$$

And the equilibrium phase space density is

$$\mathcal{N}_{Eq}(\boldsymbol{\varepsilon}, \mathbf{u}) = \frac{1}{1 + e^{\beta(\boldsymbol{\varepsilon} - \boldsymbol{\mu}_{\nu})}}. \quad (2.21)$$

The discretization of the problem is formulated in (Lackey-Stewart, 2020). In summary, we can discretize the energy domain into N_b energy bins for computational purposes. Each bin is centered at

$$\epsilon_i = \frac{\epsilon_{i-1/2} + \epsilon_{i+1/2}}{2} \quad (2.22)$$

and the volume of each energy bin is given by:

$$\Delta V_i^\epsilon = \int_{\epsilon_{i-1/2}}^{\epsilon_{i+1/2}} dV_\epsilon = \frac{4\pi}{3}(\epsilon_{i+1/2}^3 - \epsilon_{i-1/2}^3). \quad (2.23)$$

Using the finite-volume approach to discretize the governing equation, we approximate

$$\frac{d\mathcal{N}}{dt} \approx (1 - \mathcal{N}) \int_{D^\epsilon} \mathcal{R}^{in}(\epsilon, \epsilon') \mathcal{N}(\epsilon') dV_{\epsilon'} - \mathcal{N} \int_{D^\epsilon} \mathcal{R}^{out}(\epsilon, \epsilon') (1 - \mathcal{N}(\epsilon')) dV_{\epsilon'}. \quad (2.24)$$

For the i^{th} bin with a corresponding \mathcal{N}_i number density, the discretized form becomes

$$\begin{aligned} \frac{d\mathcal{N}_i}{dt} = & \sum_{k=1}^{N_b} (1 - \mathcal{N}_i) \int_{\epsilon_{k-1/2}}^{\epsilon_{k+1/2}} \mathcal{R}_{ik}^{in}(\epsilon, \epsilon') \mathcal{N}_k(\epsilon') dV_{\epsilon'} \\ & - \sum_{k=1}^{N_b} \mathcal{N}_i \int_{\epsilon_{k-1/2}}^{\epsilon_{k+1/2}} \mathcal{R}_{ik}^{out}(\epsilon, \epsilon') (1 - \mathcal{N}_k(\epsilon')) dV_{\epsilon'}. \end{aligned} \quad (2.25)$$

Assuming constant scattering rates within each bin allows us to simplify further

$$\mathcal{N}_i(t) = \frac{1}{\Delta V_i^\epsilon} \int_{\epsilon_{i-1/2}}^{\epsilon_{i+1/2}} \mathcal{N}(\epsilon, t) dV_\epsilon, \quad (2.26)$$

which represents the volume-averaged particle density in each energy bin. This leads us to the expression for the rate of change of neutrinos in the i^{th} energy bin

$$\frac{d\mathcal{N}_i}{dt} = (1 - \mathcal{N}_i) \sum_{k=1}^{N_b} \hat{\mathcal{R}}_{ik}^{in} \mathcal{N}_k - \mathcal{N}_i \sum_{k=1}^{N_b} \hat{\mathcal{R}}_{ik}^{out} (1 - \mathcal{N}_k), \quad (2.27)$$

with $\hat{\mathcal{R}}^{in/out} = \mathcal{R}^{in/out} \Delta V_k^\epsilon$.

Here we describe the rate of change of neutrino populations. In (Lackey-Stewart et al., 2024) the i^{th} energy bin had 40 equations so i ranged from 1 to 40, but here they are determined by the network size, so for the results presented in this thesis, they take on a value between 1 and 180.

Further simplification gives

$$\frac{d\mathcal{N}_i}{dt} = \sum_{k=1}^{N_b} \hat{\mathcal{R}}_{ik}^{in} \mathcal{N}_k - \mathcal{N}_i \sum_{k=1}^{N_b} \left[\hat{\mathcal{R}}_{ik}^{out} + (\hat{\mathcal{R}}_{ik}^{in} - \hat{\mathcal{R}}_{ik}^{out}) \mathcal{N}_k \right]. \quad (2.28)$$

Letting $F_i^+ = \sum_{k=1}^{N_b} \hat{\mathcal{R}}_{ik}^{in} \mathcal{N}_k$ and $\kappa_i = \sum_{k=1}^{N_b} \hat{\mathcal{R}}_{ik}^{out}$, and defining

$$\tilde{\kappa}_i = \sum_{k=1}^{N_b} \left[\delta_{ik} \kappa_k + (\hat{\mathcal{R}}_{ik}^{in} - \hat{\mathcal{R}}_{ik}^{out}) \mathcal{N}_k \right], \quad (2.29)$$

we obtain

$$\frac{d\mathcal{N}_i}{dt} = F_i^+ - \tilde{\kappa}_i \mathcal{N}_i = C_i, \quad (2.30)$$

where δ_{ik} is the Kronecker delta. This encapsulates the flux of neutrinos associated with the i^{th} bin and the rate parameter for neutrino-electron collisions. An exact solution for the differential equation is provided by

$$\mathcal{N}_i(t) = \mathcal{N}_0 e^{-\tilde{\kappa}_i t} + \frac{F_i^+}{\tilde{\kappa}_i} (1 - e^{-\tilde{\kappa}_i t}), \quad (2.31)$$

where \mathcal{N}_0 is the initial number density. The mean free path of neutrinos, assumed to travel at light speed, is

$$\ell = \frac{c}{\tilde{\kappa}_i}. \quad (2.32)$$

2.1.4 Matrix Formulation of the NES Model

The discretized NES model culminates in a matrix formulation. This formulation is structured around the spectral number density of neutrinos, \mathcal{N} , within the discretized energy bins, which transforms the Boltzmann equation into a system of linear differential equations represented in Eq. 2.27 where \mathcal{N}_i and \mathcal{N}_k represent the neutrino number densities in bins i and k , respectively, and N_b is the total number of bins. The transition rates $\mathcal{R}_{ik}^{in/out}$ encapsulate the physics of neutrino scattering between these bins.

Converting this equation into matrix form, we introduce a vector \mathcal{N} representing the neutrino number densities across all energy bins and a matrix \mathbf{M} encoding the transition rates between bins, such that

$$\frac{d\mathcal{N}}{dt} = \mathbf{M}(\mathcal{N}) \cdot \mathcal{N}, \quad (2.33)$$

where \mathbf{M} is an $N_b \times N_b$ collision matrix, embodying the interaction rates between different energy bins.

The elements of the collision matrix, M_{ik} , are defined as

$$M_{ik} = \hat{\mathcal{R}}_{ik}^{in} - \delta_{ik} \tilde{\kappa}_k, \quad (2.34)$$

indicating the rate at which neutrinos scatter into ($\hat{\mathcal{R}}^{\text{in}}$) and out of ($\hat{\kappa}$) the energy bins. This formulation captures both the influx and efflux of neutrinos in each bin, modulated by the in-scattering and out-scattering rates, respectively.

Defining $\dot{\mathcal{N}}_i \equiv d\mathcal{N}_i/dt$, we have explicitly for the ‘‘Collision Matrix’’

$$\begin{pmatrix} \dot{\mathcal{N}}_1 \\ \dot{\mathcal{N}}_2 \\ \dot{\mathcal{N}}_3 \\ \vdots \\ \dot{\mathcal{N}}_{N_b} \end{pmatrix} = \begin{pmatrix} M_{11} & M_{12} & M_{13} & \dots & M_{1N_b} \\ M_{21} & M_{22} & M_{23} & \dots & M_{2N_b} \\ M_{31} & M_{32} & M_{33} & \dots & M_{3N_b} \\ \vdots & \vdots & \vdots & \dots & \vdots \\ M_{N_b1} & M_{N_b2} & M_{N_b3} & \dots & M_{N_bN_b} \end{pmatrix} \begin{pmatrix} \mathcal{N}_1 \\ \mathcal{N}_2 \\ \mathcal{N}_3 \\ \vdots \\ \mathcal{N}_{N_b} \end{pmatrix} \quad (2.35)$$

The results presented in [Lackey-Stewart et al. \(2024\)](#) used a 40×40 matrix, but here we can incorporate matrices up to 180×180 . Standard explicit methods for solving the matrix differential equations in stiff systems often require non-competitive, extremely small time steps to maintain stability. However, it will be shown that algebraically stabilized explicit methods can achieve competitive time steps. Explicit integration methods are used at each time step to simulate the dynamical neutrino distributions from well-defined initial conditions.

On the other hand, implicit schemes require much more costly matrix inversions at every step. While it is true that implicit methods can demand multiple matrix inversions within one time step, especially during strong interaction phases, the primary concern is the non-linear impact of matrix inversions on computing time. Typically, the dependence of computing time on the size of the matrix is quadratic or worse. By using less costly matrix-vector multiplications, we can reduce the computational load and take more cost-effective time steps.

Chapter 3

Numerical Integration

3.1 Numerical Integration Methods for Neutrino Distribution

The two dominant algorithms used in numerical simulations for the distributions of neutrinos over astrophysical events in this thesis consist of the explicit asymptotic method and the forward Euler algorithm. In this regard, such methods play an active role in stabilizing the evolution of the neutrino distribution, hence keeping at bay most of the computational difficulties sometimes induced by stiff differential equations.

3.1.1 Explicit Asymptotic Method

As described in more depth for neutrinos in (Lackey-Stewart, 2020), as well as in thermonuclear networks in (Guidry, 2012; Guidry et al., 2013b), the explicit asymptotic method approximates the future state of neutrino number densities. More specifically, the explicit asymptotic method approximates the future state of the number density of neutrinos by iterating solutions for \mathcal{N}_i^{n+1} . This calculates the number density at the next time step $n + 1$, based on the current time step n . The derivative of this expansion is given by

$$\mathcal{N}_i = \frac{1}{\tilde{\kappa}_i} \left(F_i^+ - \frac{d_i \mathcal{N}_i}{dt} \right), \quad (3.1)$$

and in the asymptotic limit where $\frac{d\mathcal{N}_i}{dt} \rightarrow 0$ implying $F_i^+ \approx \tilde{\kappa}_i$, the finite-difference approximation yields:

$$\frac{d\mathcal{N}_i^n}{dt} = \frac{\mathcal{N}_i^{n+1} - \mathcal{N}_i^n}{\Delta t} - \frac{\Delta t}{2} \frac{d^2 \mathcal{N}_i^n}{dt^2} + \dots, \quad (3.2)$$

truncating at the first term for small derivatives. This leads to an approximate expression for \mathcal{N}_i^{n+1} :

$$\mathcal{N}_i^{n+1} = \mathcal{N}_i^n + \frac{\Delta t C_i^n}{1 + \tilde{\kappa}_i \Delta t}. \quad (3.3)$$

Particle number conservation check for the explicit asymptotic (EA) method involves,

$$N_{\text{tot}}^{n+1} = N_{\text{tot}}^n + \Delta t \sum_{i=1}^{N_b} \frac{C_i^n}{1 + \tilde{\kappa}_i \Delta t} \Delta V_i^\epsilon, \quad (3.4)$$

with the Taylor Series expansion of the denominator

$$\frac{1}{1 + \tilde{\kappa}_i \Delta t} = \sum_{m=0}^{\infty} (-1)^m (\tilde{\kappa}_i \Delta t)^m, \quad (3.5)$$

resulting in

$$N_{\text{tot}}^{n+1} = N_{\text{tot}}^n + \Delta t \sum_{i=1}^{N_b} C_i^n \Delta V_i^\epsilon + \sum_{i=1}^{N_b} \sum_{m=1}^{\infty} C_i^n \Delta V_i^\epsilon (-1)^m (\tilde{\kappa}_i)^m (\Delta t)^{m+1}, \quad (3.6)$$

where C_i^n is directly derived from the rate of change of \mathcal{N}_i^n . This approach, based on the first term of Taylor series expansion, has the significant advantage of providing a clear formula that allows one to avoid the explicit inversion of matrices and is thus particularly efficient for large-scale simulation.

The tolerance condition for conservation of particle number is defined as:

$$\left| \frac{N_{\text{tot}}^{n+1} - N_{\text{tot}}^n}{N_{\text{tot}}^n} \right| \leq \text{tolC}, \quad (3.7)$$

and an additional tolerance condition for the accuracy in density between time steps is introduced

$$\max \left[\frac{|\mathcal{N}^{n+1} - \mathcal{N}^n|}{\max(\mathcal{N}^n, 10^{-8})} \right] \leq \text{tolN}. \quad (3.8)$$

3.1.2 Explicit Forward Euler Algorithm

The Forward Euler Algorithm is a simplistic explicit numerical integration requiring small time steps for stability in stiff systems. We can apply it directly to the neutrino distribution evolution as

$$\mathcal{N}_i^{n+1} = \mathcal{N}_i^n + \Delta t C_i^n, \quad (3.9)$$

with the change rate C_i^n defined as

$$C_i^n \equiv \frac{d\mathcal{N}_i^n}{dt} = \eta_i - \tilde{\kappa}_i \mathcal{N}_i^n. \quad (3.10)$$

The total particle number at a specific time t is approximated by the sum over all energy bins

$$N_{\text{tot}}(t) \approx \sum_{i=1}^{N_b} \mathcal{N}_i(t) \Delta V_i^\epsilon. \quad (3.11)$$

By multiplying Eq. 3.9 by ΔV_i^ϵ and summing over all bins, we derive the expression for the total particle number at the next time step

$$N_{\text{tot}}^{n+1} = N_{\text{tot}}^n + \Delta t \sum_{i=1}^{N_b} C_i^n \Delta V_i^\epsilon. \quad (3.12)$$

Evaluating the summation of $C_i^n \Delta V_i^\epsilon$ leads to the conclusion that the total particle number remains conserved

$$\sum_{i=1}^{N_b} C_i^n \Delta V_i^\epsilon = \sum_{i=1}^{N_b} \sum_{k=1}^{N_b} (\mathcal{R}_{ik}^{\text{in}} - \mathcal{R}_{ki}^{\text{out}}) (1 - \mathcal{N}_i) \mathcal{N}_k \Delta V_i^\epsilon \Delta V_k^\epsilon = 0, \quad (3.13)$$

which holds due to the symmetry of the scattering kernels, ensuring $N_{\text{tot}}^{n+1} = N_{\text{tot}}^n$, thus confirming that the forward Euler method conserves particle number at each step to machine precision.

This scheme ensures stability for time steps Δt smaller than a critical threshold τ_c , prescribed by the inverse of the fastest rate in the system. It has an advantage in being a simple and computationally effective way for small time steps, which could fully integrate the system dynamics.

Therefore the decision to use either the forward Euler or the explicit asymptotic method relies on the comparative size of the integration time step Δt and the critical time step τ_c . For $\Delta t < \tau_c$, the forward Euler method is stable and preferred due to its simplicity. On the other hand, for $\Delta t \geq \tau_c$, when the forward Euler scheme can become unstable, the use of the explicit asymptotic method is far more stable and shows us better results without instability for larger values of the time step.

This approach ensures that the integration done in FENN remains stable and efficient, allowing for accurate simulations of neutrino dynamics across varying timescales and interaction intensities.

3.1.3 Backward Euler Method

The backward Euler (BE) method, an implicit method used for comparison with the explicit asymptotic (EA) method, is applied as follows:

$$\mathcal{N}_i^{n+1} = \mathcal{N}_i^n + \Delta t C_i^{n+1}, \quad (3.14)$$

where it is noted that BE conserves particle number within a specified tolerance and requires solving an algebraic equation for future density values \mathcal{N}_i^{n+1} . This is approached using the Newton-Raphson method with a defined tolerance parameter, tolBE. The algebraic equation to solve is

$$\mathcal{N}_i^{n+1}(1 + \tilde{\kappa}_i(\mathcal{N}^{n+1})\Delta t) - \Delta t F_i^+(\mathcal{N}^{n+1}) - \mathcal{N}_i^n = 0, \quad (3.15)$$

or concisely, $f(\mathcal{N}_i^{n+1}) = 0$. The iterative formula for the Newton-Raphson method is:

$$\mathcal{N}_{i,k+1}^{n+1} = \mathcal{N}_{i,k}^{n+1} - \frac{f(\mathcal{N}_{i,k}^{n+1})}{f'(\mathcal{N}_{i,k}^{n+1})}, \quad (3.16)$$

with the termination condition

$$\left| \frac{f(\mathcal{N}_{i,k}^{n+1})/f'(\mathcal{N}_{i,k}^{n+1})}{\mathcal{N}_{i,k+1}^{n+1}} \right| < \text{tolBE}. \quad (3.17)$$

The Newton-Raphson method's vector form, requiring matrix inversions, is

$$\mathcal{N}_{k+1}^{n+1} = \mathcal{N}_k^{n+1} - \frac{f(\mathcal{N}_k^{n+1})}{f'(\mathcal{N}_k^{n+1})}. \quad (3.18)$$

Chapter 4

Integration of WeakLib and FENN

4.1 Pipeline Algorithms

WeakLib is a Fortran based computational library developed at Oak Ridge Labs, that allows the computation of 5 dimensional tables as referenced in section 2. To incorporate the neutrino scattering opacities (Φ_{In}), tabulated within WeakLib, as demonstrated in the above formalism, into FENN, a dedicated pipeline algorithm was developed. This algorithm reads the tabulated data, applies necessary physical constants such as the speed of light, and seamlessly integrates this data into the FENN simulation environment. A greatly simplified pipeline was used in (Lackey-Stewart et al., 2024), however, a modified pipeline is required for integration with the WeakLib library that can read an arbitrary ρ , T , Y_e grid. The new pipeline first introduced in (Chari et al., 2024) is outlined in the following sections.

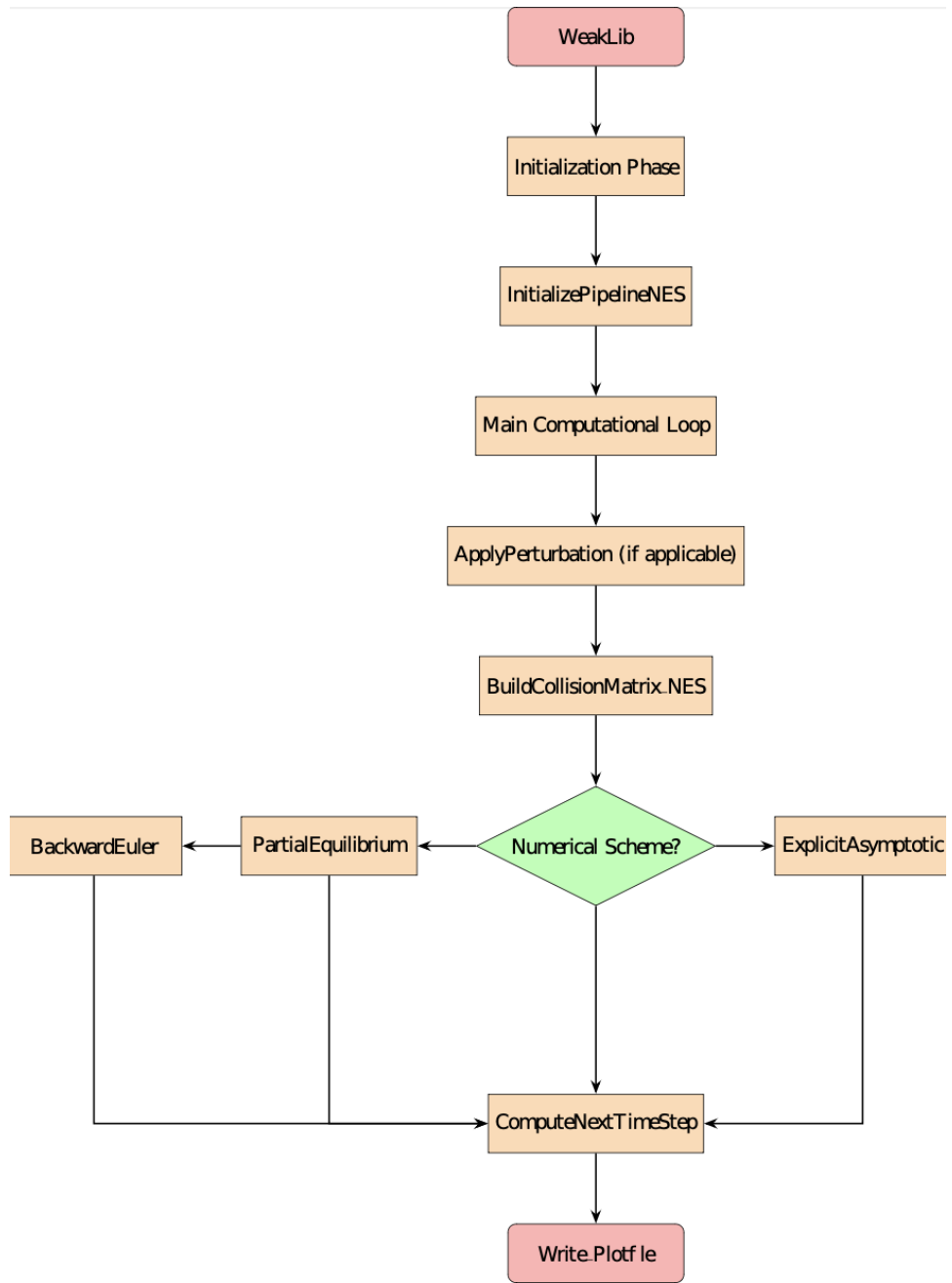


Figure 4.1: WeakLib to FENN Integration.

4.1.1 Data Reading and Transformation

Given a file path `filePath` and dataset name `datasetName`, the algorithm reads multidimensional data for neutrino scattering opacities Φ_{In} .

Procedure 1: Initialization of the NES Pipeline	
Data:	$N_g, eC, dV, R_{\text{In}}, R_{\text{Out}}, N_{\text{Eq}}, \text{ScatteringKernel}, filePath, mu, kT, Rho, Ye$
Result:	Initialize variables and compute values for R_{Out} and N_{Eq}
1	$eC \leftarrow \text{ReadData1DFromHDF5}(filePath, \text{"ProfileInfo/Energy"});$
2	$de \leftarrow$ $\text{ReadData1DFromHDF5}(filePath, \text{"ProfileInfo/EnergyWidths"});$
3	for $i \leftarrow 0$ to $N_g - 1$ do
4	$dV[i] \leftarrow ((eC[i] + 0.5 \times de[i])^3 - (eC[i] - 0.5 \times de[i])^3)/3;$
5	end
6	$mu \leftarrow$ $\text{ReadDataFromHDF5}(filePath, \text{"ProfileInfo/Chemical_Potential"});$
7	$kT \leftarrow \text{ReadDataFromHDF5}(filePath, \text{"ProfileInfo/Temperature"});$
8	$Rho \leftarrow \text{ReadDataFromHDF5}(filePath, \text{"ProfileInfo/Density"});$
9	$Ye \leftarrow$ $\text{ReadDataFromHDF5}(filePath, \text{"ProfileInfo/Electron_Fraction"});$
10	Select dataset based on ScatteringKernel ;
11	$R_{\text{In}} \leftarrow \text{ReadData2DFromHDF5}(filePath, datasetName);$
12	$c \leftarrow 3 \times 10^{10};$
13	for $i \leftarrow 0$ to $R_{\text{In}}.size() - 1$ do
14	for $j \leftarrow 0$ to $R_{\text{In}}[i].size() - 1$ do
15	$R_{\text{In}}[i][j] \leftarrow R_{\text{In}}[i][j] \times c;$
16	$R_{\text{Out}}[i][j] \leftarrow R_{\text{In}}[j][i];$ // Switch matrix
17	end
18	end
19	$N_{\text{Eq}} \leftarrow$ Initialize based on mu and kT ;
20	for $i \leftarrow 0$ to $N_g - 1$ do
21	for $j \leftarrow 0$ to $N_g - 1$ do
22	if $j < i$ then
23	$R_{\text{In}}[i][j] \leftarrow R_{\text{In}}[j][i] \times \exp((eC[j] - eC[i])/kT);$
24	end
25	$R_{\text{Out}}[i][j] \leftarrow R_{\text{In}}[j][i];$
26	end
27	end

Figure 4.2: InitializePipelineNES algorithm

4.1.2 Treatment of Φ_{In}

The speed of light c is used to scale the Φ_{In} scattering rates read from the datasets:

$$\mathbf{R}_{\text{In}} = \mathbf{R}_{\text{In}} \cdot c \quad (4.1)$$

Given energy bin centers \mathbf{eC} and widths \mathbf{de} , the volume elements \mathbf{dV} are calculated from Eq. 2.23 for $i = 1, \dots, N_g$. For a selected scattering kernel, the input and output rates \mathbf{R}_{In} and \mathbf{R}_{Out} are adjusted to reflect physical constraints and detailed balance:

$$R_{\text{Out},ij} = R_{\text{In},ji} \exp\left(\frac{eC_j - eC_i}{kT}\right), \quad \forall i, j \quad (4.2)$$

4.1.3 Equilibrium Distribution Initialization

The equilibrium distribution \mathbf{N}_{Eq} is initialized based on the chemical potential μ and temperature kT :

$$N_{\text{Eq},i} = \frac{1}{\exp\left(\frac{eC_i - \mu}{kT}\right) + 1}, \quad i = 1, \dots, N_g \quad (4.3)$$

4.2 Newton-Raphson Method Implementation for Neutrino Scattering Simulations

Newton-Raphson is the primary solver for our backward Euler calculations. This results in costly matrix inversions at each time step, while explicit asymptotic has less costly matrix-vector multiplication, requiring more steps that are more cost effective. The backward Euler mathematical formulation is described more in depth in (Lackey-Stewart, 2020).

4.2.1 Jacobian Matrix Computation

The Jacobian matrix, \mathbf{J} , crucial for the Newton-Raphson iteration, is computed based on finite differences, incorporating the input and output scattering rates, \mathbf{R}_{In} and \mathbf{R}_{Out} , across discrete energy groups.

$$\mathbf{J}(\mathbf{N}) = -(\mathbf{R}_{\text{In}} \odot (\mathbf{1} - \mathbf{N}) + \mathbf{R}_{\text{Out}} \odot \mathbf{N}) + \text{Diag}(-(\mathbf{R}_{\text{In}}\mathbf{N} + \mathbf{R}_{\text{Out}}(\mathbf{1} - \mathbf{N}))), \quad (4.4)$$

where \odot denotes the element-wise multiplication, and $\text{Diag}(\cdot)$ creates a diagonal matrix from the vector argument. The diagonal components are adjusted separately to account for the conservation laws and the specific dynamics of neutrino scattering.

4.2.2 Right-Hand Side Computation

The right-hand side (RHS) of the Newton-Raphson method encapsulates the balance between the scattering into and out of each energy state:

$$\mathbf{F}(\mathbf{N}) = (\mathbf{1} - \mathbf{N}) \odot (\mathbf{R}_{\text{In}}\mathbf{N}) - \mathbf{N} \odot (\mathbf{R}_{\text{Out}}(\mathbf{1} - \mathbf{N})). \quad (4.5)$$

4.2.3 Newton-Raphson Iteration

The Newton-Raphson iterative process for updating the neutrino occupation numbers is detailed as follows:

1. Compute the Jacobian $\mathbf{J}(\mathbf{N})$ and RHS $\mathbf{F}(\mathbf{N})$ at the current estimate \mathbf{N} .
2. Solve the linear system $(\mathbf{I} - \Delta t \mathbf{J}(\mathbf{N})) \Delta \mathbf{N} = (\mathbf{N}_{\text{old}} - \mathbf{N}) + \Delta t \mathbf{F}(\mathbf{N})$ for $\Delta \mathbf{N}$.
3. Update the solution $\mathbf{N} \leftarrow \mathbf{N} + \Delta \mathbf{N}$.
4. Check for convergence using the norm of $\Delta \mathbf{N}$ relative to \mathbf{N} ; if not converged, return to step 1.

The algorithm proceeds until the solution converges to within a specified defined tolerance.

4.2.4 Timestep Functions

Additionally, we can adjust our timestep settings by varying the Tolerance Conditions from Eq. 3.7. Each timestep has a fixed dt_{grow} value for a more robust timestepping algorithm.

Algorithm 1: ComputeNextTimeStep: Adjusting simulation time step based on energy ratios.

Result: Calculate the new time step size based on the energy ratios.

Data: E_O , E_D vectors of energy outputs and demands, and the old time step dt_{old} .

```
1 if Size of  $E_O$   $\neq$  Size of  $E_D$  then
2   | Throw an invalid argument exception;
3 end
4  $E_R \leftarrow 0$ ;
5 for each index  $i$  from 0 to size of  $E_O$  do
6   |  $E_R \leftarrow$  maximum of  $E_R$  and  $\frac{E_O[i]}{E_D[i]}$ ;
7 end
8 if  $E_R > 0.1$  then
9   |  $dt_{new} \leftarrow dt_{old} \times 0.9 \times E_R^{-1.0}$ ;
10 else
11   | if  $E_R < 0.5$  then
12     |  $dt_{new} \leftarrow dt_{old} \times 0.9 \times E_R^{-0.5}$ ;
13   | else
14     |  $dt_{new} \leftarrow dt_{old}$ ;
15   | end
16 end
17  $dt_{new} \leftarrow$  maximum of minimum of  $dt_{new}$  and  $2 \times dt_{old}$ ,  $0.5 \times dt_{old}$ ;
```

Figure 4.3: The ComputeNextTimeStep function modifies the time step dynamically, responding to the ratio of energy output to energy demand ($E_O \rightarrow E_D$). It reduces the time step when this ratio is too high to preserve the accuracy of the simulation, and it expands the time step when the ratio is low to enhance efficiency.

Algorithm 2: computeTimeStep EA: Calculating new time step size using environmental assessment.

Result: Determine the new time step size using an environmental assessment (EA) approach.

Data: C matrix of concentrations, k vector of reaction coefficients, N vector of quantities, dV vector of volumes, tolerance $tolC$, fixed time step dt_{FE} , and initial time step dt_0 .

```

1 Initialize  $CN$  vector of size  $n$  with zeros;
2 for each  $i$  from 0 to  $n - 1$  do
3   | for each  $j$  from 0 to  $n - 1$  do
4   | |  $CN[j] \leftarrow CN[j] + C[j][i] \times N[i]$ ;
5   | end
6 end
7  $Ntot \leftarrow 0$ ;
8 for each  $i$  from 0 to  $n - 1$  do
9   |  $Ntot \leftarrow Ntot + dV[i] \times N[i]$ ;
10 end
11  $dt_{EA} \leftarrow dt_0$ ;
12  $|sumVal| > tolC \times Ntot$   $sumVal \leftarrow 0$ ;
13 for each  $i$  from 0 to  $n - 1$  do
14   |  $sumVal \leftarrow sumVal + dV[i] \times \left( \frac{dt_{EA} \times CN[i]}{1.0 + dt_{EA} \times k[i]} \right)$ ;
15 end
16 if  $|sumVal| > tolC \times Ntot$  then
17   |  $dt_{EA} \leftarrow 0.9 \times dt_{EA}$ ;
18 end
19  $dt_{EA} \leftarrow \max(dt_{EA}, dt_{FE})$ ;

```

Figure 4.4: The computeTimeStep EA function employs an environmental assessment approach, adjusting the time step according to the total changes observed over a time step compared to a predefined tolerance. This method allows the function to modify the time step to maintain simulation precision within set limits.

Chapter 5

Tradeoff of Speed and Accuracy

5.1 Single Models

We can begin by presenting a representative of one set of conditions using explicit asymptotic methods. Figure 5.1 shows the variation of number density N_i across 40 energy bins as a function of time, as well as the progression of computational time steps in relation to the temporal axis. All corresponding model conditions are tabulated in the appendix A. We are using a wide range of thermodynamic conditions expected to occur in core-collapse supernovae.

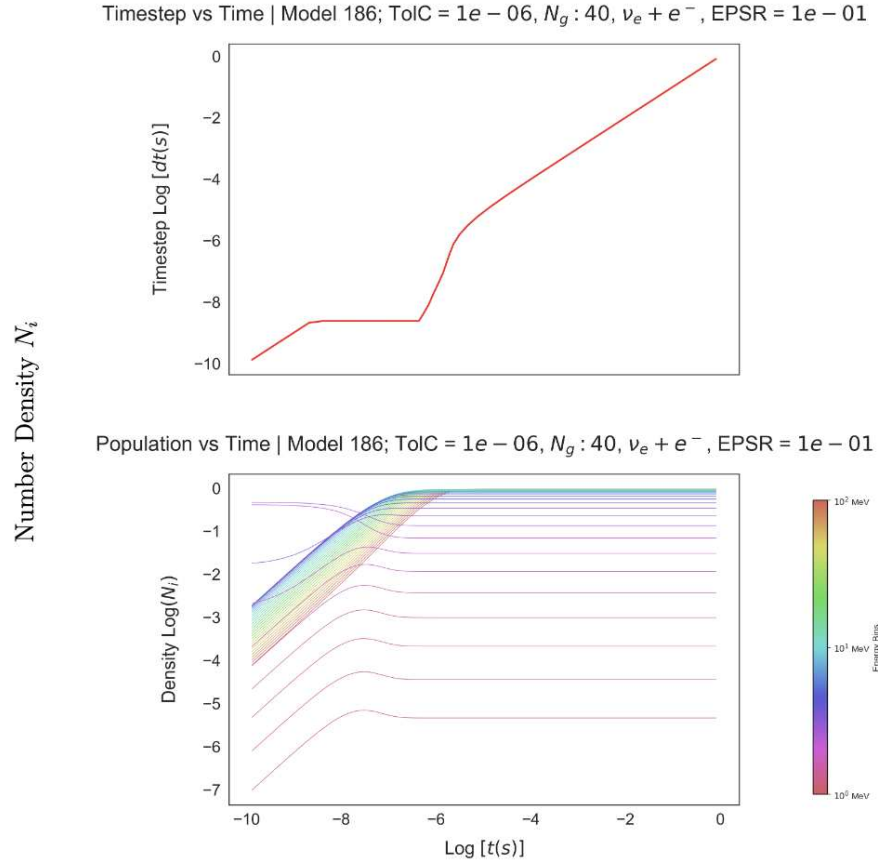


Figure 5.1: Dynamics of Model 186 showing Number Density N_i across 40 energy bins vs time and time step vs time. The calculation referenced took 323 explicit steps.

5.1.1 Heatmaps

We can also introduce heatmaps for the scattering rates for Neutrino Electron Scattering. The following heatmaps are for a network size of 50 and reflect the rates used in the proceeding sections.

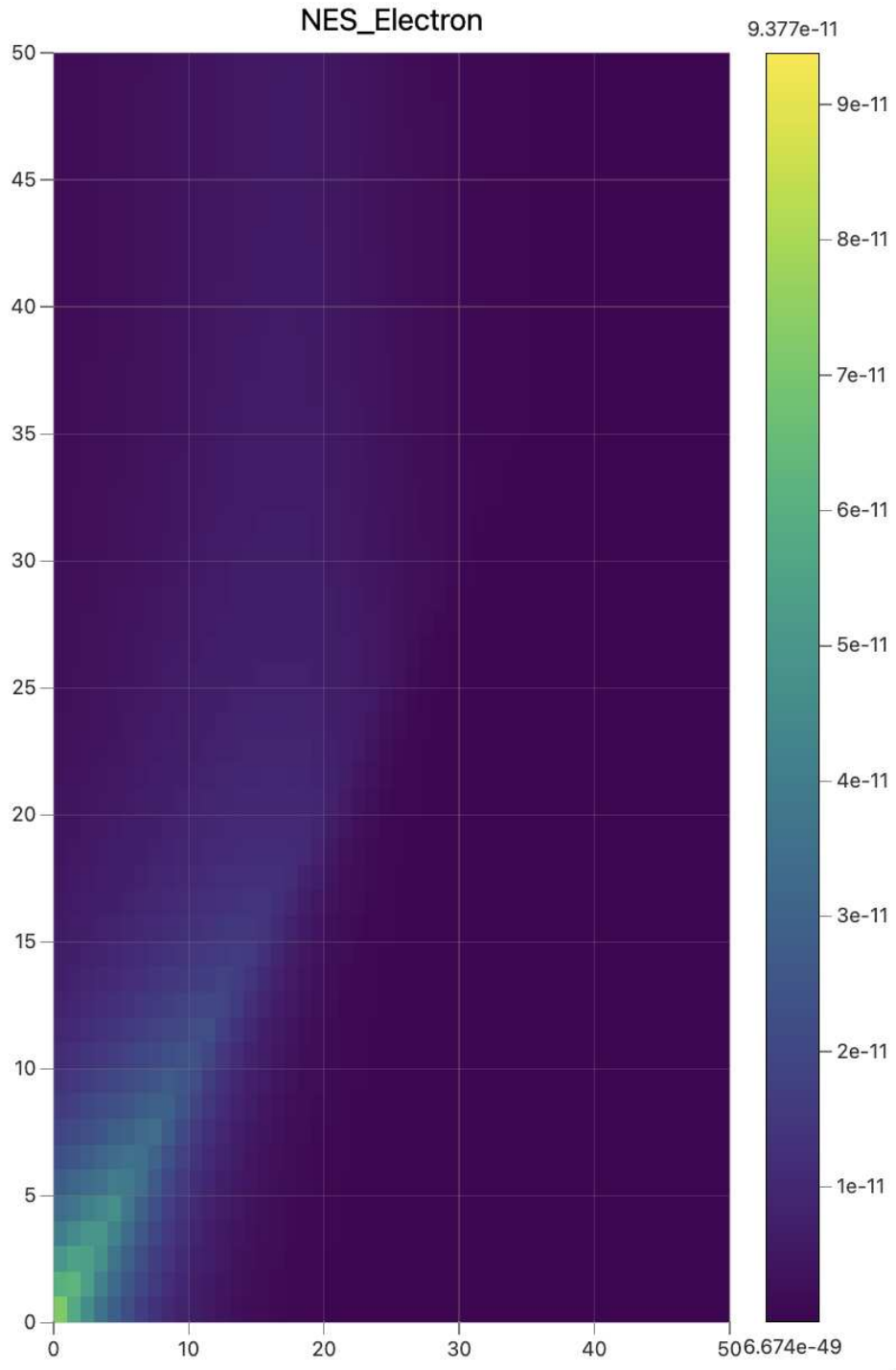


Figure 5.2: Model 81 Heatmap

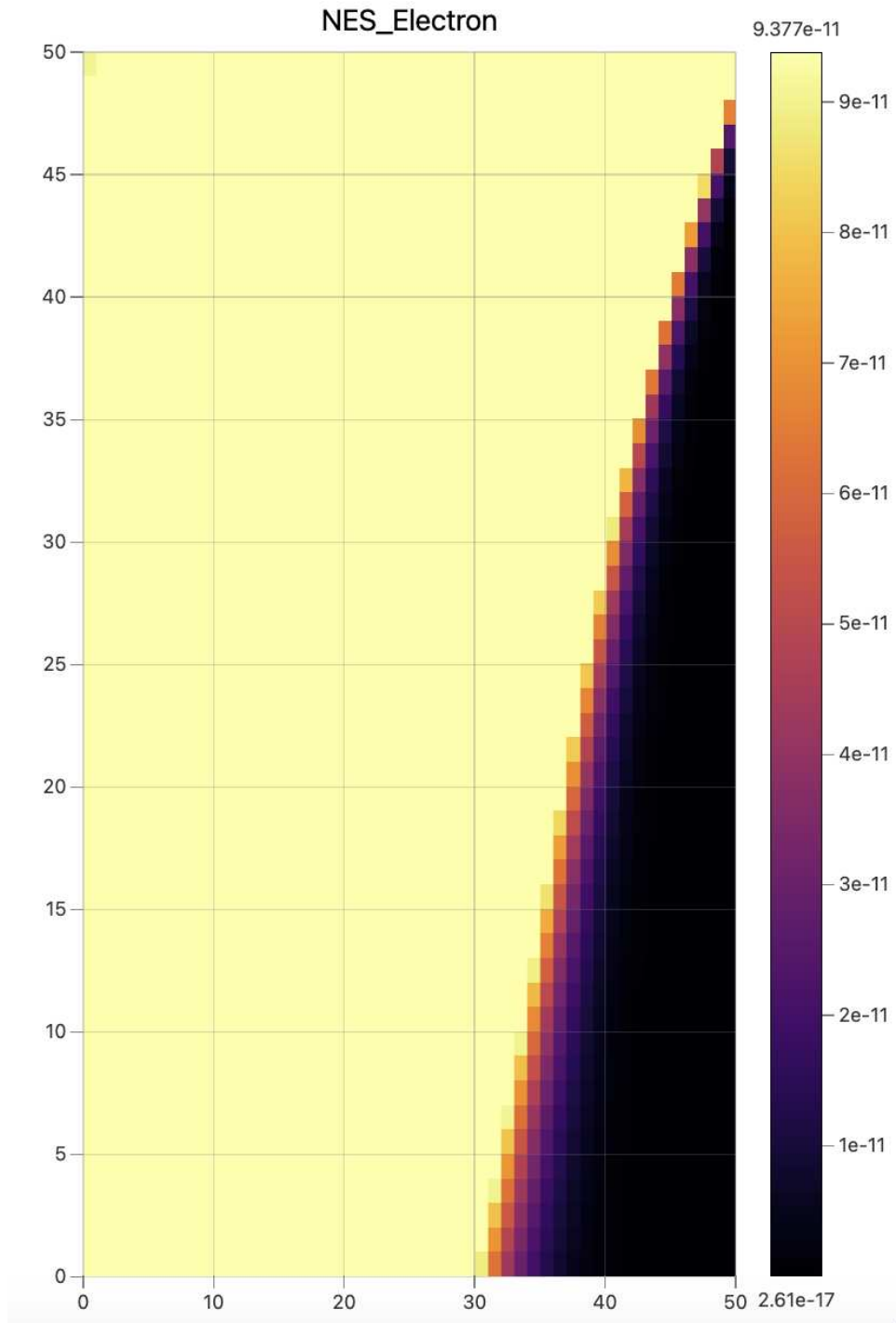


Figure 5.3: Model 186 Heatmap

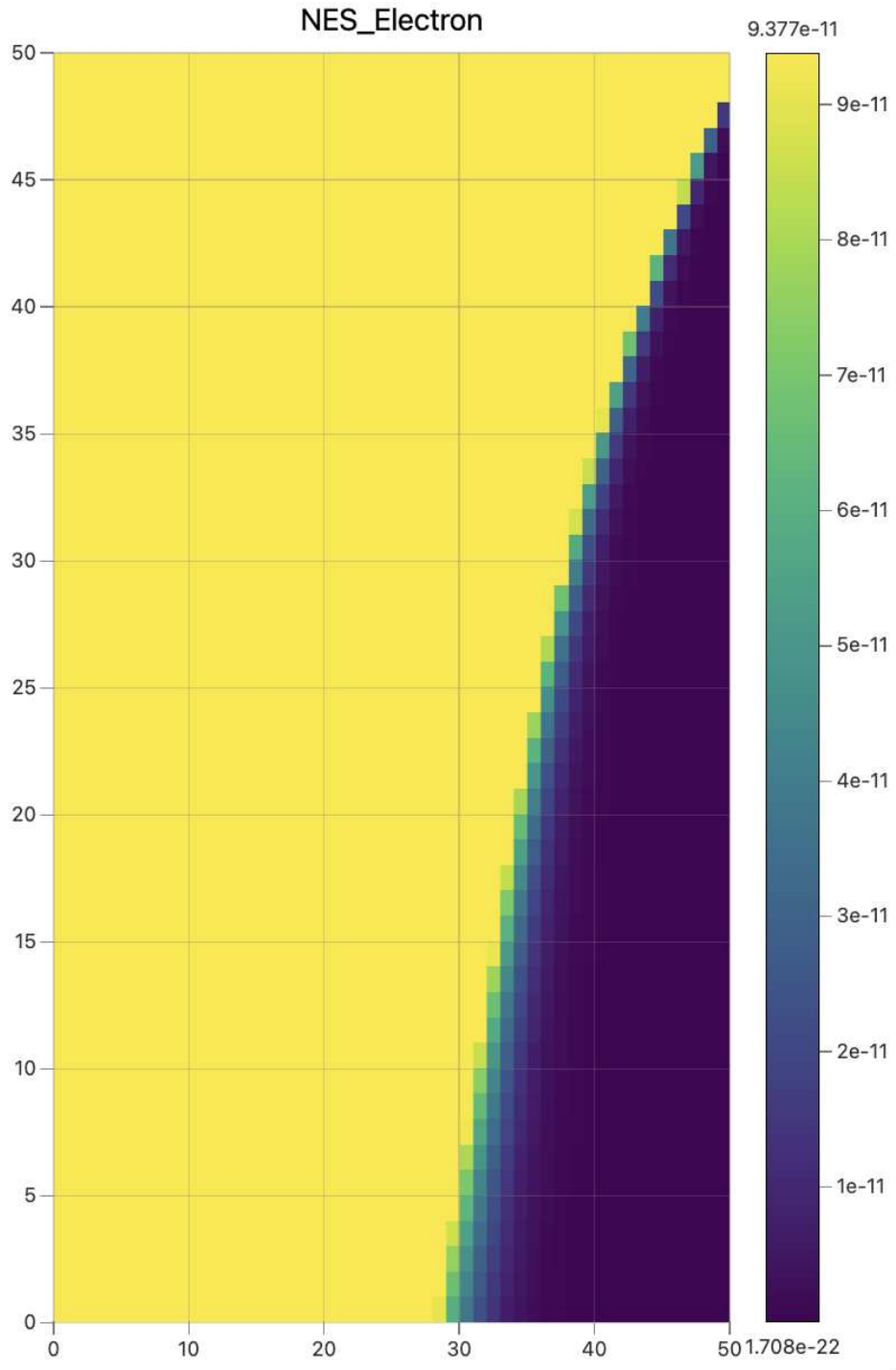


Figure 5.4: Model 213 Heatmap

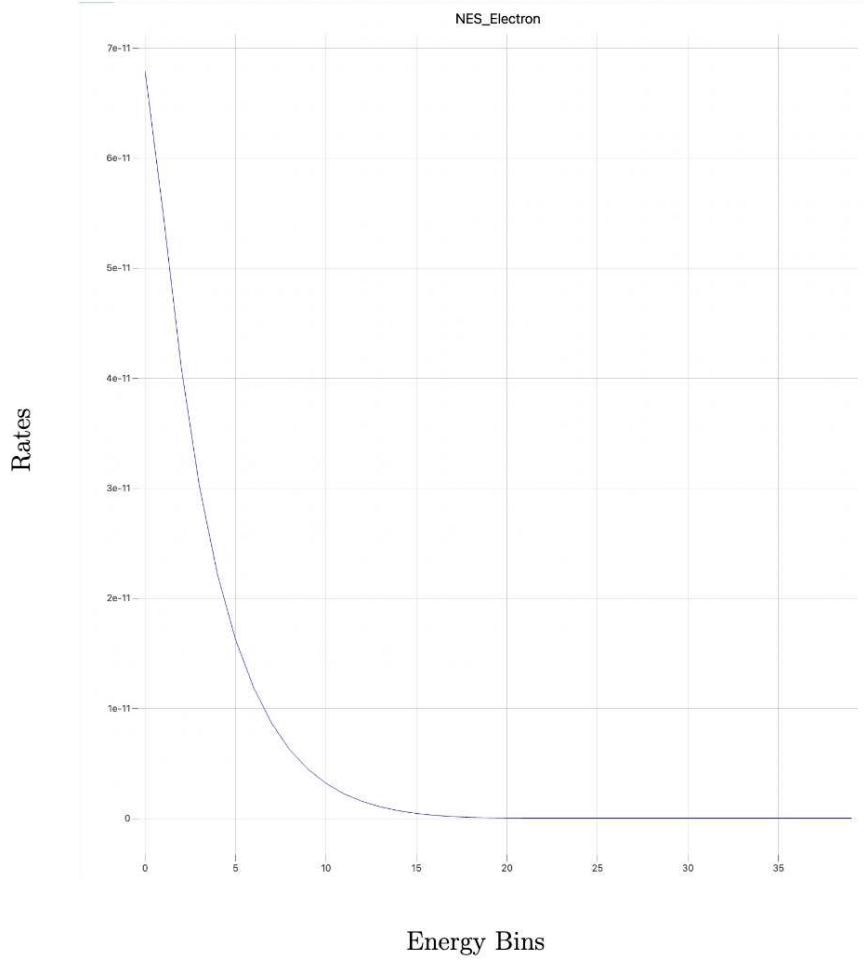


Figure 5.5: Φ_{In} for one Energy Level

Before comparing backward Euler versus explicit results we have to define a quantitative measure of accuracy, since approximations of the realistic problem introduces some level of error. More in-depth explanations are formulated in (Lackey-Stewart et al., 2024)

We can characterize the accuracy of an explicit algebraic evaluation of the neutrino evolution by integrating the deviation of the neutrino number densities n_i from backward Euler results, which is our basis of comparison. We employ a root mean square calculation in number densities integrated (approximated by a sum) over all energy bins. $R_i(t)$ is defined for each species i in the network at every time t ,

$$R_i(t) \equiv |n_i(t) - n_i^0(t)|, \quad (5.1)$$

where $n_i(t)$ is the explicit asymptotic approximation for the number density in bin i at time t . We can define the root mean square (RMS) error $R(t)$ summed over all bins at time t ,

$$R(t) \equiv \sqrt{\sum_i R_i(t)^2} = \sqrt{\sum_i |n_i(t) - n_i^0(t)|^2}, \quad (5.2)$$

where the sum is over all energy bins and $\sum_i n_i^0 = 1$.

We can then approximate the total error per unit time ϵ as

$$\epsilon = \frac{1}{\delta t} \sum_{j=j_0}^{j(t_{\text{eq}})} R(t_j) \delta t_j, \quad (5.3)$$

where t_j is the time at the j th plot output step, j_0 is the first plot output step with finite $R(t)$, $j(t_{\text{eq}})$ is the plot output step corresponding to the equilibration time, $\delta t_j = t_j - t_{j-1}$ is the time difference between the j th and $(j-1)$ th plot output steps, and $\delta t \equiv t_{\text{eq}} - t(j_0)$ is the total time between the onset of finite $R(t)$ and equilibration at t_{eq} . These are represented in the ϵ vs Time plots in the comparisons.

5.1.2 A Quantitative Measure of Speed

The explicit algebraic methods are parameterized in terms of the total number of integration steps required to complete a given simulation. This is what is known as an ‘‘intrinsic’’ measure. The total integration time is a function of the steps and the time required for each step, however, the backward Euler is doing complex matrix inversions at each step, while explicit is doing matrix-vector multiplication .

We can define a speedup factor as $F \equiv 1/(1-f)$, where f is the fraction of overall computing time spent by the implicit code (backward Euler) in its linear algebra solver during for each timestep. We then expect the explicit asymptotic to be approximately F times faster than backward Euler in the same computational environment.

The factor F has been computed in (Guidry et al., 2013b) using an implicit backward Euler code *Xnet* (Hix and Thielemann, 1999). Note that these use a dense matrix solver, so our results in a dense 40-species neutrino network are approximately valid.

For a 40 bin calculation we can define it as:

$$\frac{\Delta t_{\text{EA}}}{\Delta t_{\text{BE}}} \simeq \frac{S_{\text{EA}}}{F \cdot S_{\text{BE}}} \simeq 0.25 \left(\frac{S_{\text{EA}}}{S_{\text{BE}}} \right), \quad (5.4)$$

where Δt denotes elapsed wall clock time and S is the steps. The 40-species network was employed in (Lackey-Stewart et al., 2024), however here we investigate larger networks also.

5.2 Energy Grid Definitions

All of the following calculations were done in the energy grid shown in fig. 5.6.

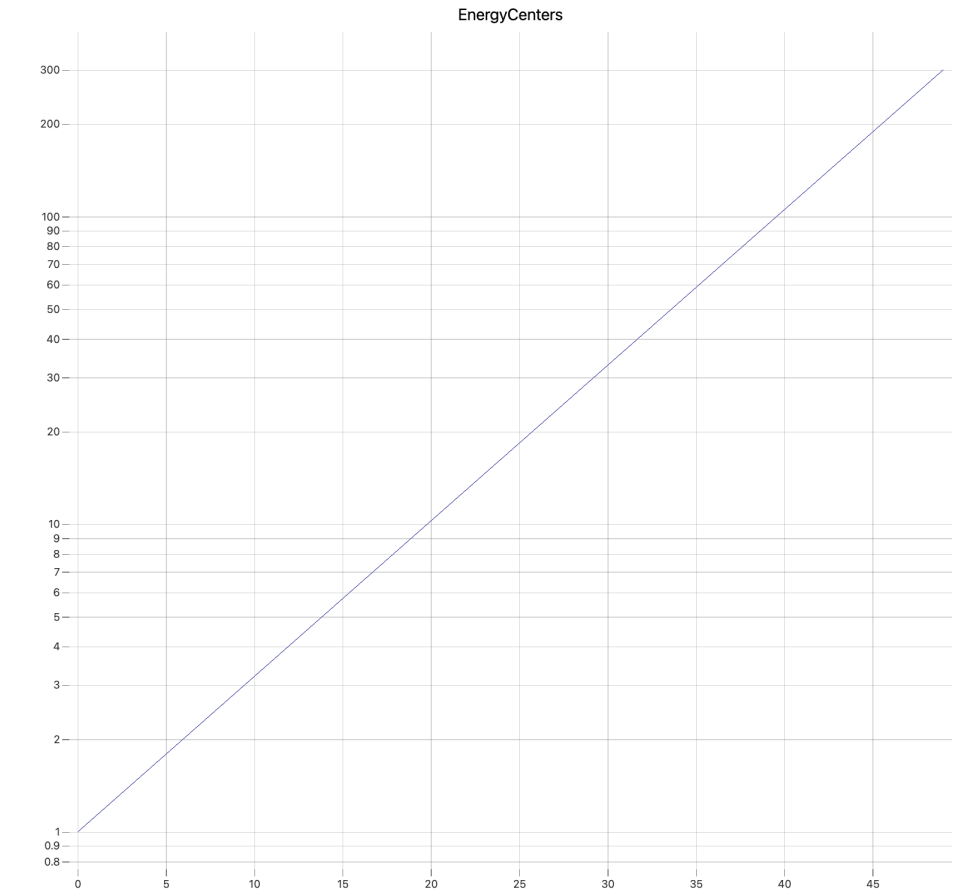


Figure 5.6: Energy Grid for a 50-species network. Energies are logarithmically spaced from 1 – 300 MeV.

Similarly for fig. 5.7.

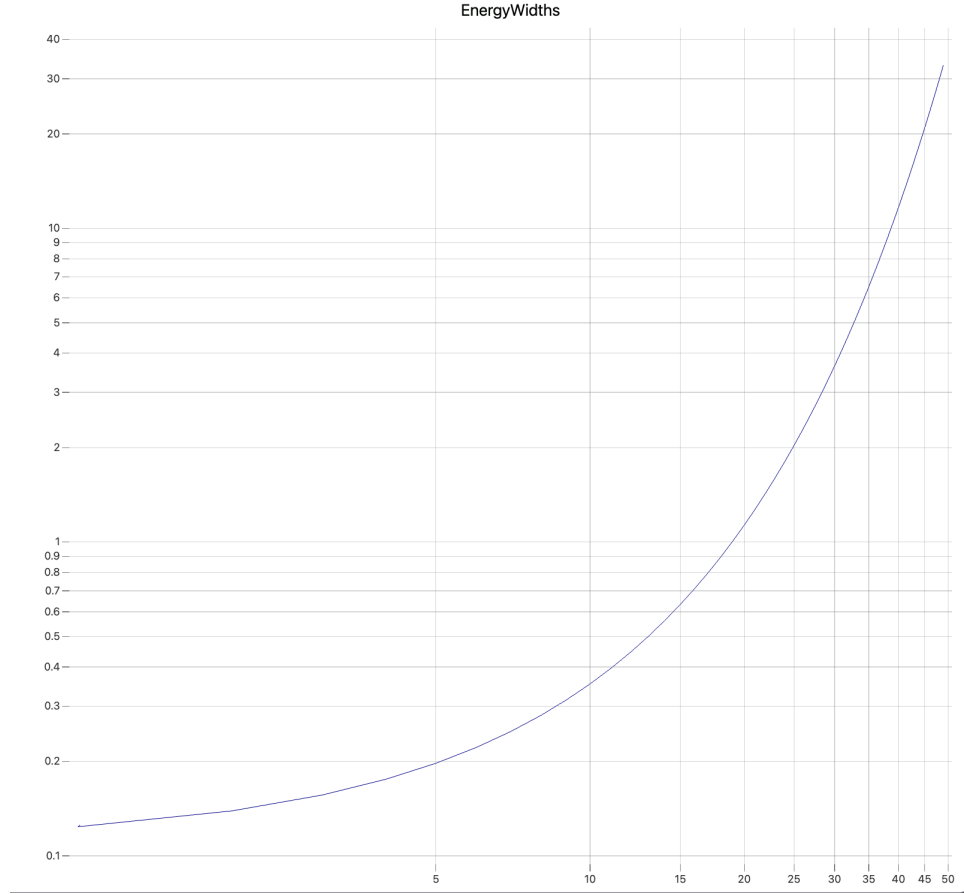


Figure 5.7: Energy Widths

Data values are tabulated in the appendix [A](#)

5.3 Model Analysis

We can take a few of the models from appendix [A](#), and do a comparative analysis of speed versus accuracy.

5.3.1 Model 81 Analysis

We can begin our comparison with Model 81. We group the results by the Accurate, Intermediate, and Fast cases. These are controlled by the tolerance and are representative conditions. The following calculations were done with respect to the energy grid in fig. [5.6](#):

Here the time steps are represented in the Population vs Time plots as *Explicit(Implicit)* ϵ is taken as a function of time calculated up until equilibrium as referenced in Eq. [5.3](#).

Accurate Case

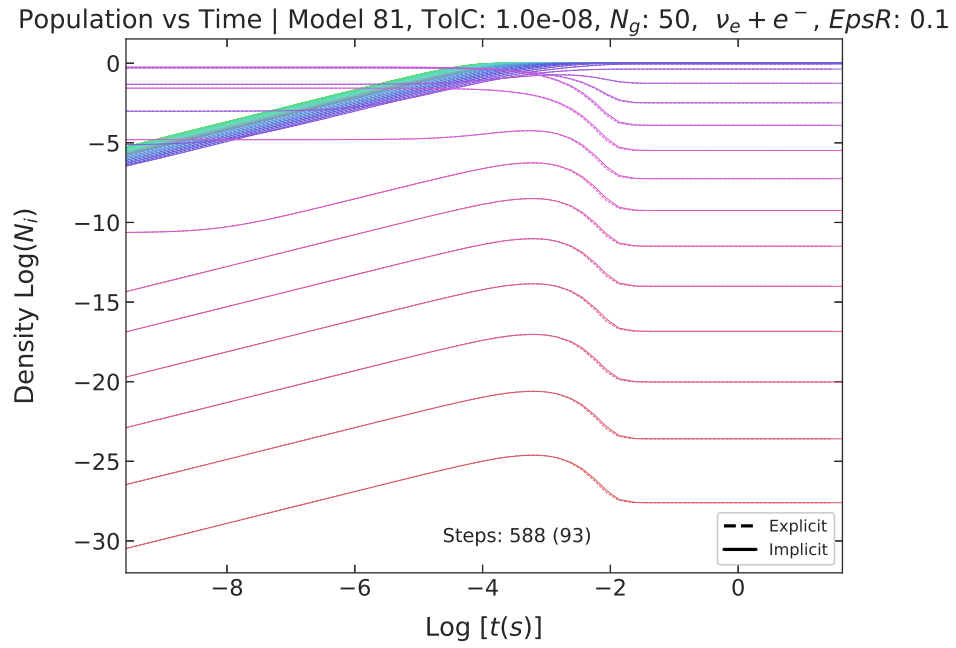


Figure 5.8: Population vs time for Model 81 - Accurate Case.

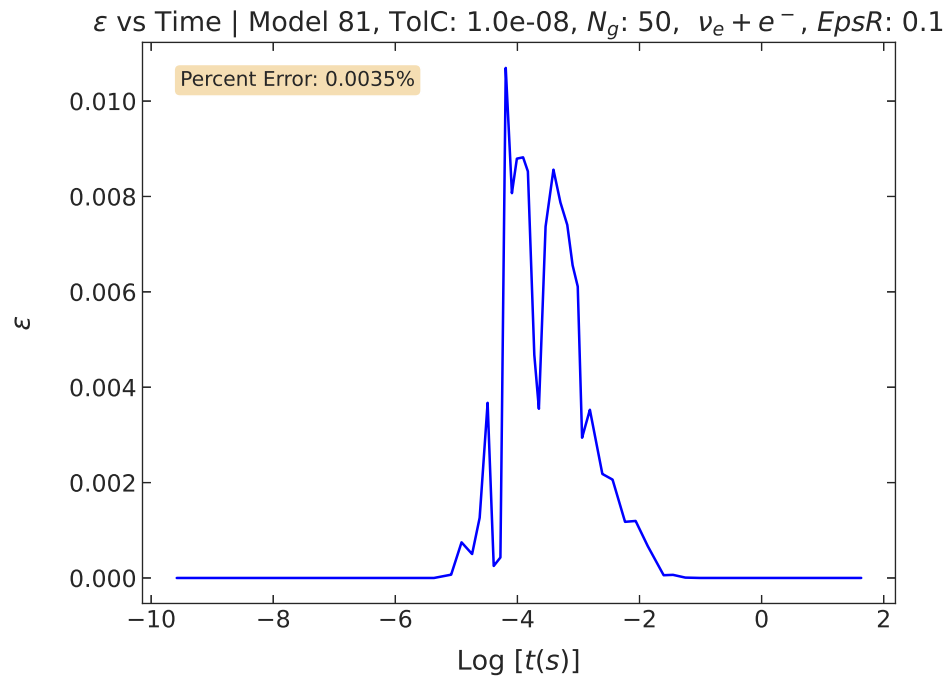


Figure 5.9: RMS vs time for Model 81 - Accurate Case.

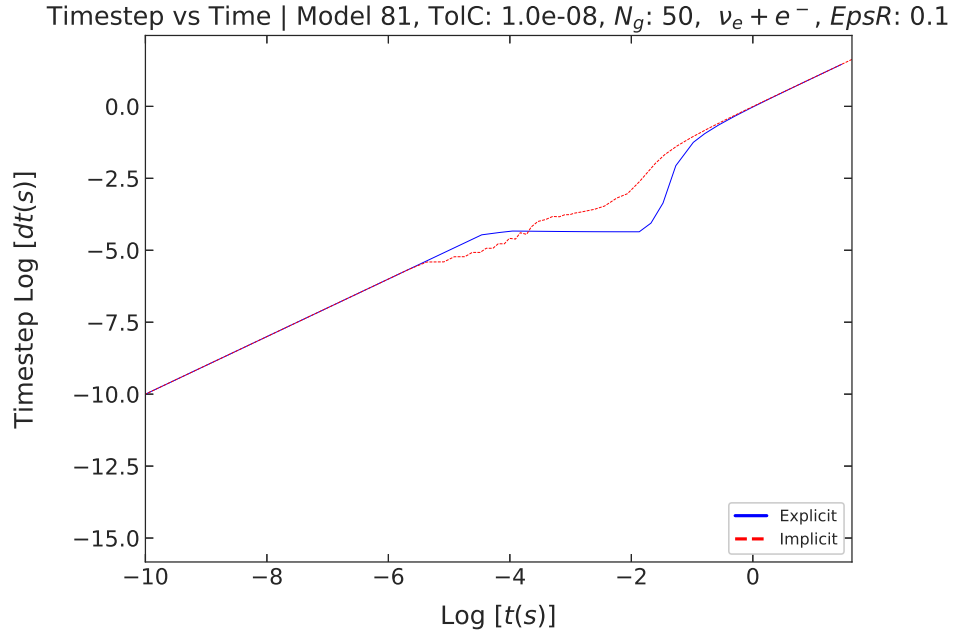


Figure 5.10: Time step vs time for Model 81 - Accurate Case.

Here, TolC is 10^{-8} which takes small time steps. The error is as a result very small.

Intermediate Case

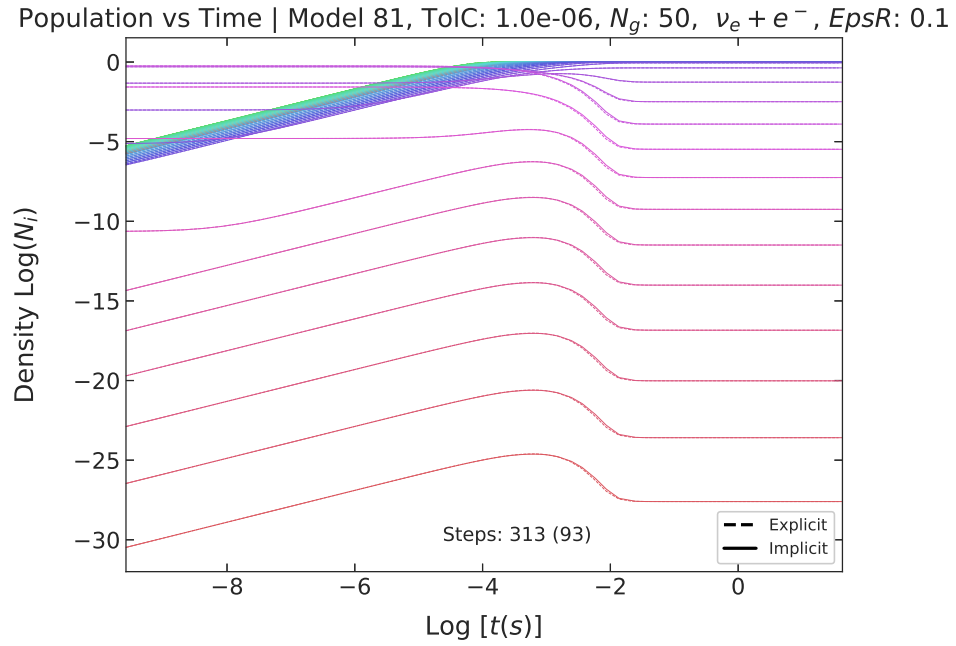


Figure 5.11: Population vs time for Model 81 - Intermediate Case.

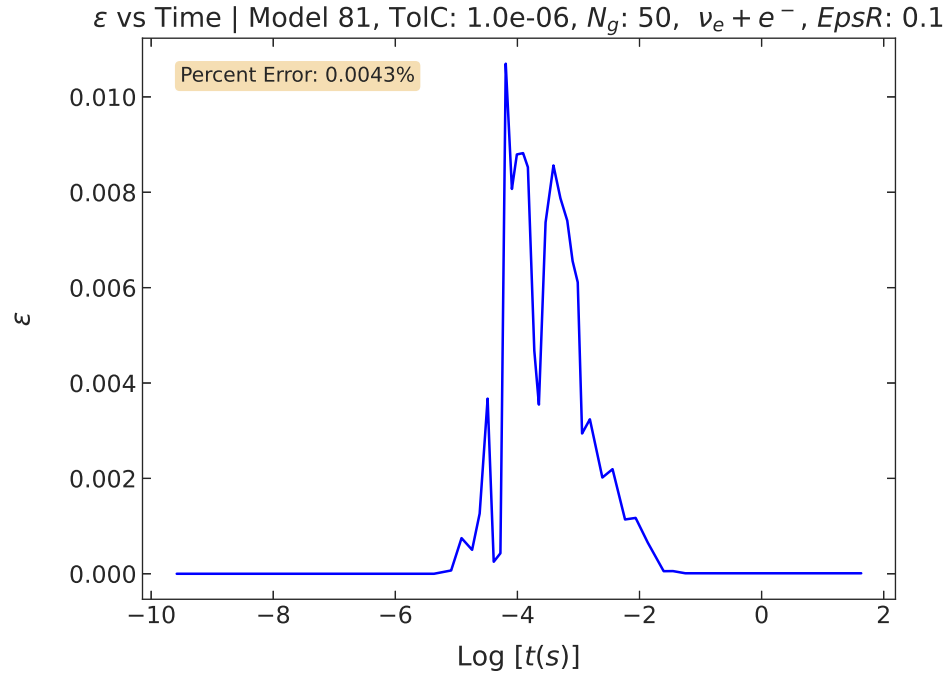


Figure 5.12: RMS vs time for Model 81 - Intermediate Case.

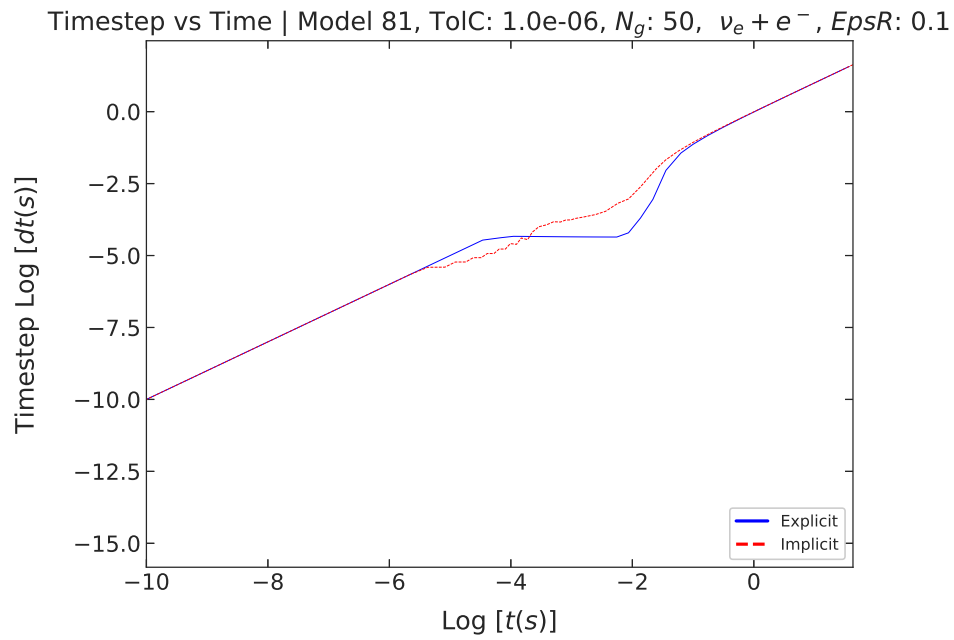


Figure 5.13: Time step vs time for Model 81 - Intermediate Case.

For our intermediate case we can adjust TolC to 10^{-6} which loosens the particle conservation, taking faster time steps against the same backward Euler comparison.

Fast Case

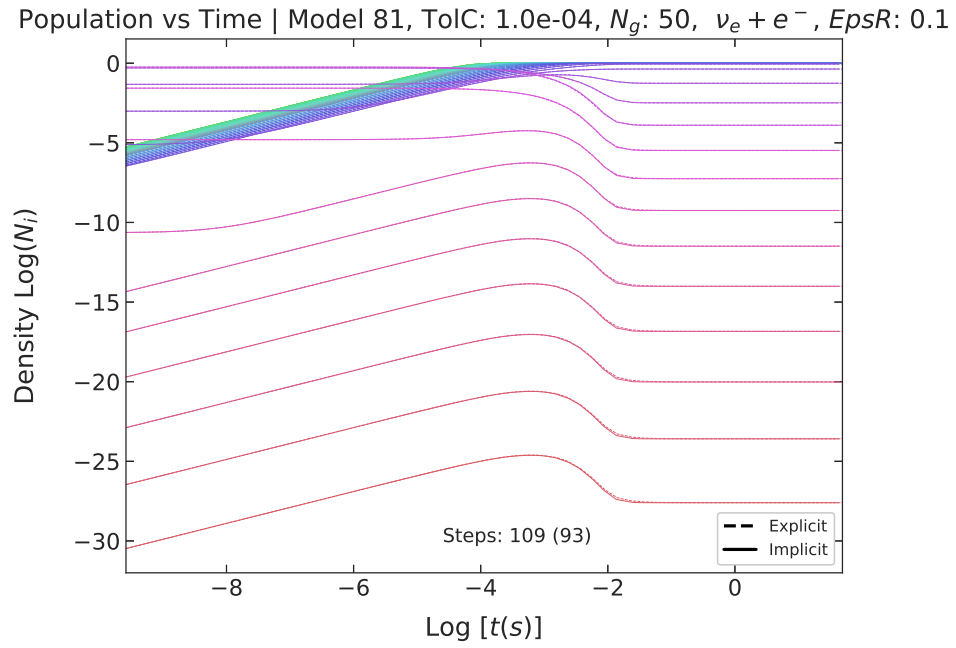


Figure 5.14: Population vs time for Model 81 - Fast Case.

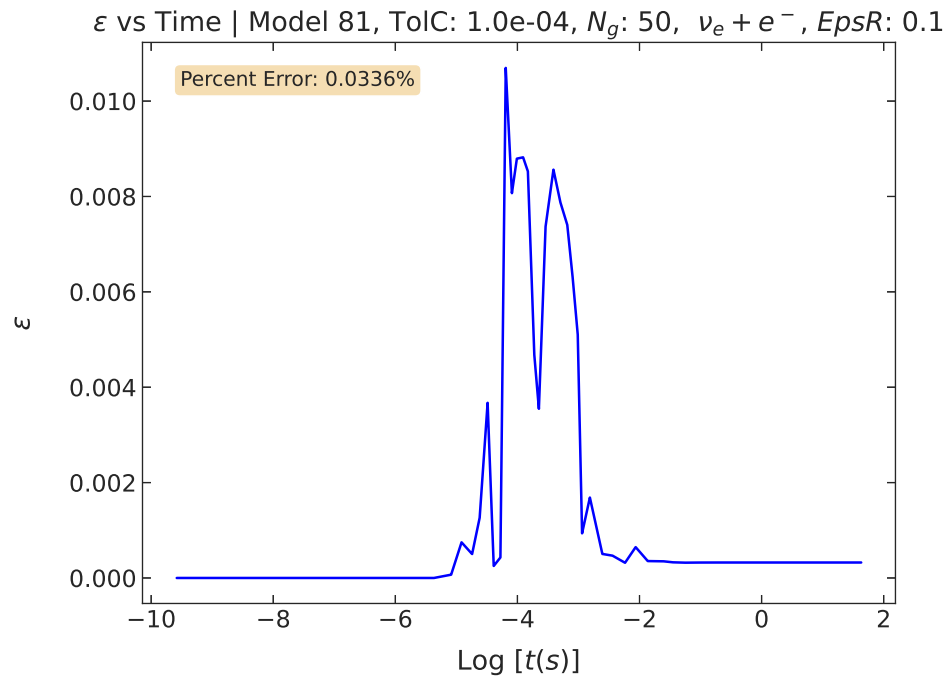


Figure 5.15: RMS vs time for Model 81 - Fast Case.

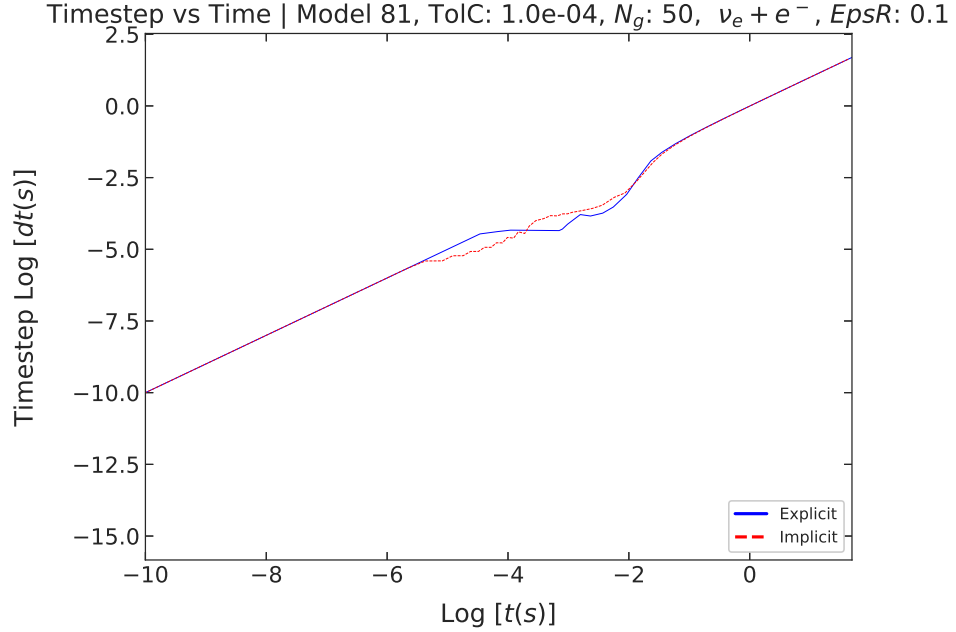


Figure 5.16: Time step vs time for Model 81 - Fast Case.

Similarly, we adjust TolC to 10^{-4} which loosens the conservation of particles even more taking only 109 time steps for explicit.

Case	Steps Explicit	Steps Implicit	Error (%)
Accurate	588	93	0.0035
Intermediate	313	93	0.0043
Fast	109	93	0.0336

Table 5.1: Summary of steps and error for Model 81.

Here the error from Eq. 5.3 occurs in restricted areas of integration time. This is shown in fig. 5.9, 5.12, and fig. 5.15 where the error accumulates almost entirely between $t \approx 10^{-6} - \approx 10^{-2}$ seconds.

When using operator-split coupling in hydrodynamics, the continuous integration in fig. 5.9 can be segmented into sequential, piece wise integrations within each fluid zone. Each segment corresponds to integrating the network over one hydrodynamical timestep in the zone. Consequently, significant errors from the neutrino network for that zone are confined to a narrow range of hydrodynamical integration steps, specifically between 10^{-6} and 10^{-2} seconds. This observation

allows for potential optimization of speed versus accuracy on a per-zone basis within the hydro-kinetic system, though such optimizations are left for future exploration.

Furthermore, it's crucial to understand how neutrino network errors, as defined in Eq. 5.3 and illustrated in fig. 5.9 and in table 5.1, translate into overall errors in the coupled kinetic-hydrodynamical system due to specific algebraic approximations. The error calculated from Eq. 5.3 represents the RMS error per unit time across the relevant times where $R(t)$ is non-zero. Importantly, there is no error for hydro integration steps that do not intersect with significant $R(t)$ regions shown in fig. 5.9. For those hydro time steps that do intersect in these significant regions, the error introduced by network approximations per hydro time step Δt_{hydro} will depend on the integrated value of $R(t)$ during that time step, influenced by factors such as hydro integration methods, zone sizes, and fluid characteristics at the time. This makes the error case-specific. However, the relatively low values of E chosen in fig. 5.9 indicate that the maximum overall error can be limited to a few percent or less while still achieving sufficient speed, when applied to specific scenarios.

5.3.2 Model 186 Analysis

Similarly, we can proceed for Model 186

Accurate Case

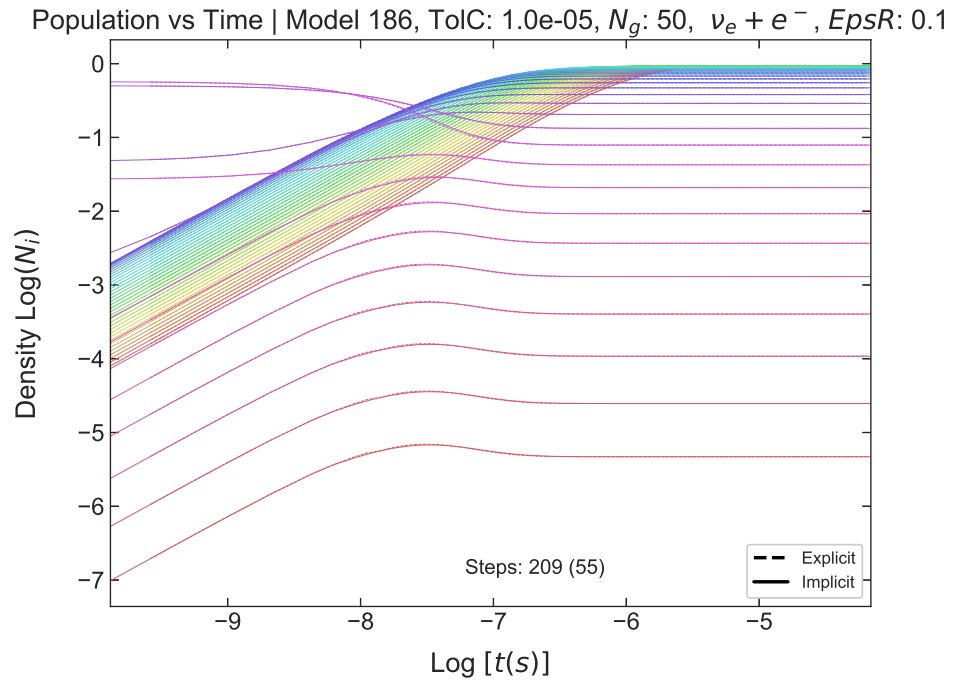


Figure 5.17: Population vs time for Model 186 - Accurate Case.

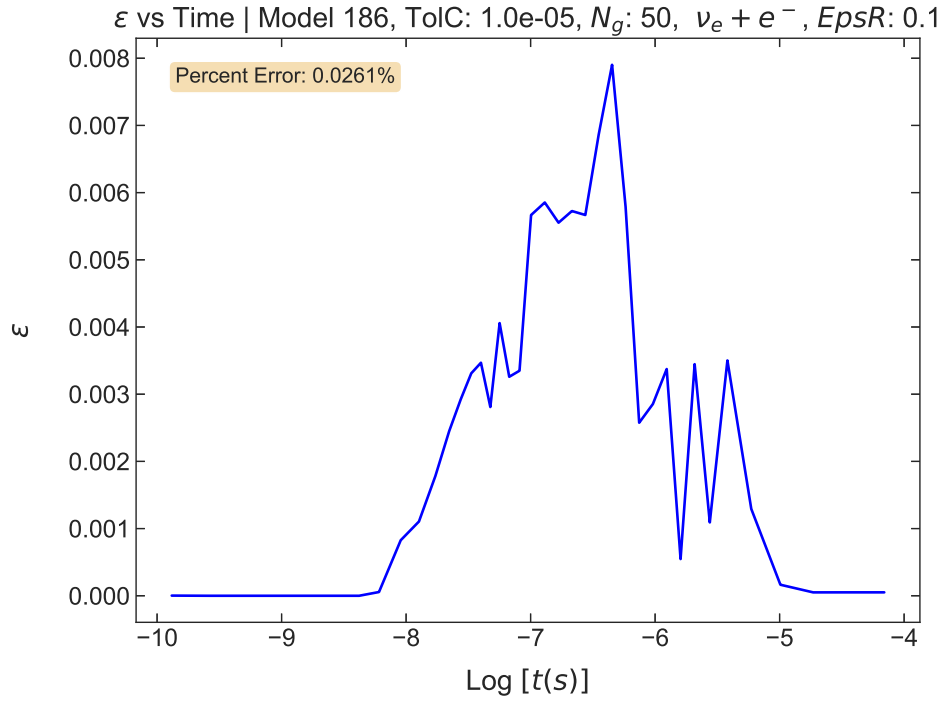


Figure 5.18: RMS vs time for Model 186 - Accurate Case.

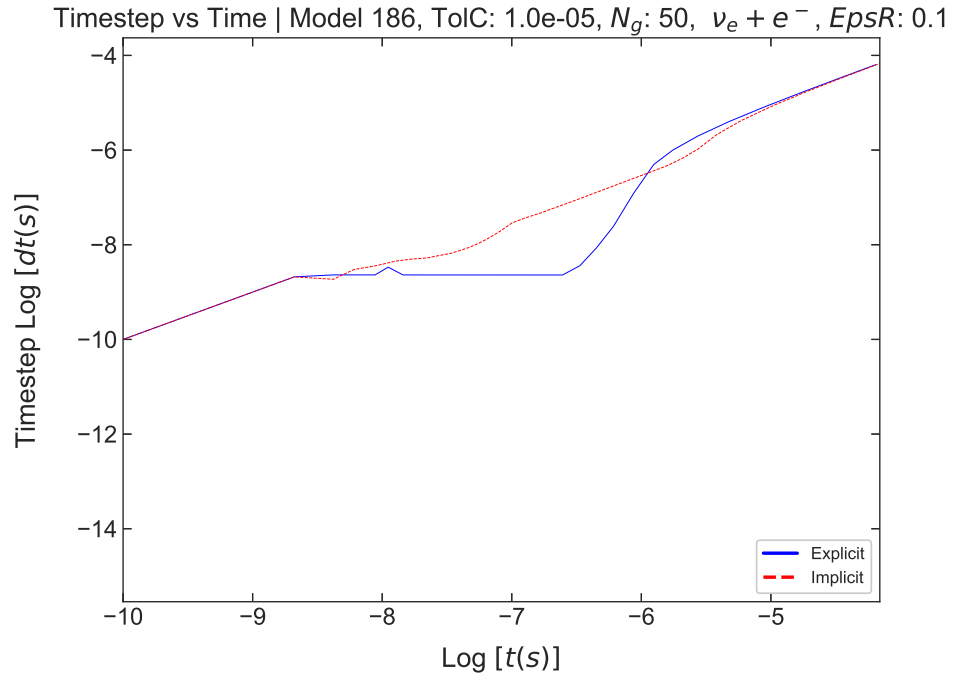


Figure 5.19: Timestep vs time for Model 186 - Accurate Case.

Intermediate Case

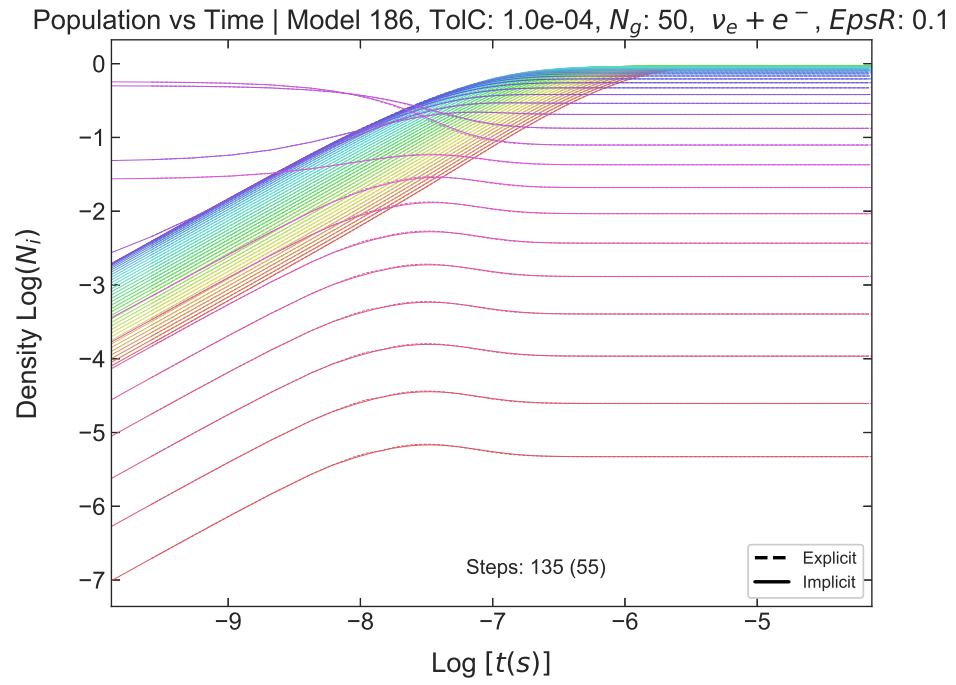


Figure 5.20: Population vs time for Model 186 - Intermediate Case.

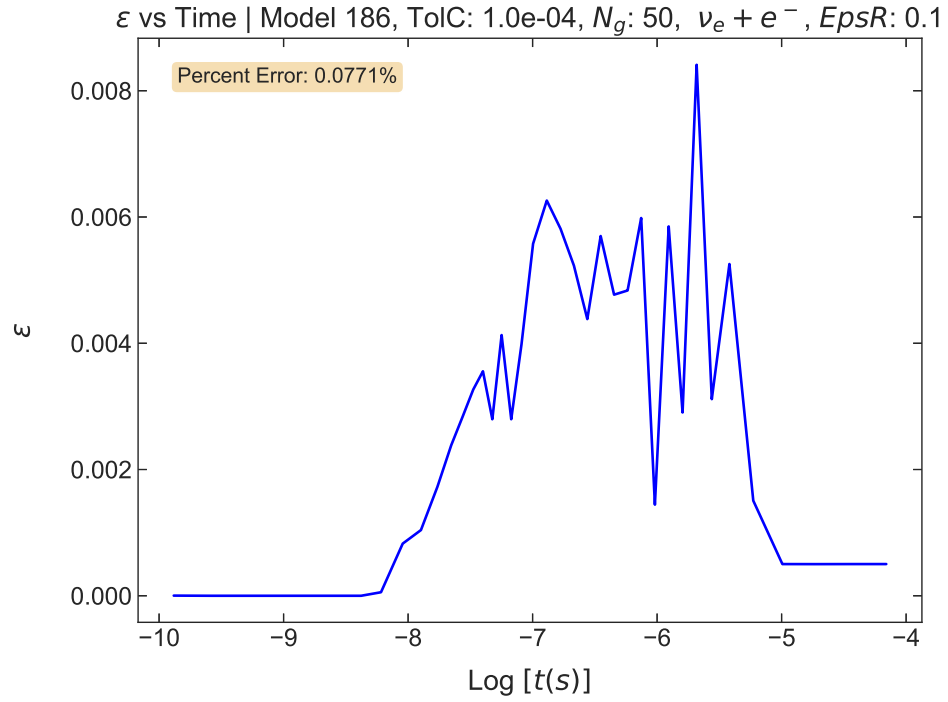


Figure 5.21: RMS vs time for Model 186 - Intermediate Case.

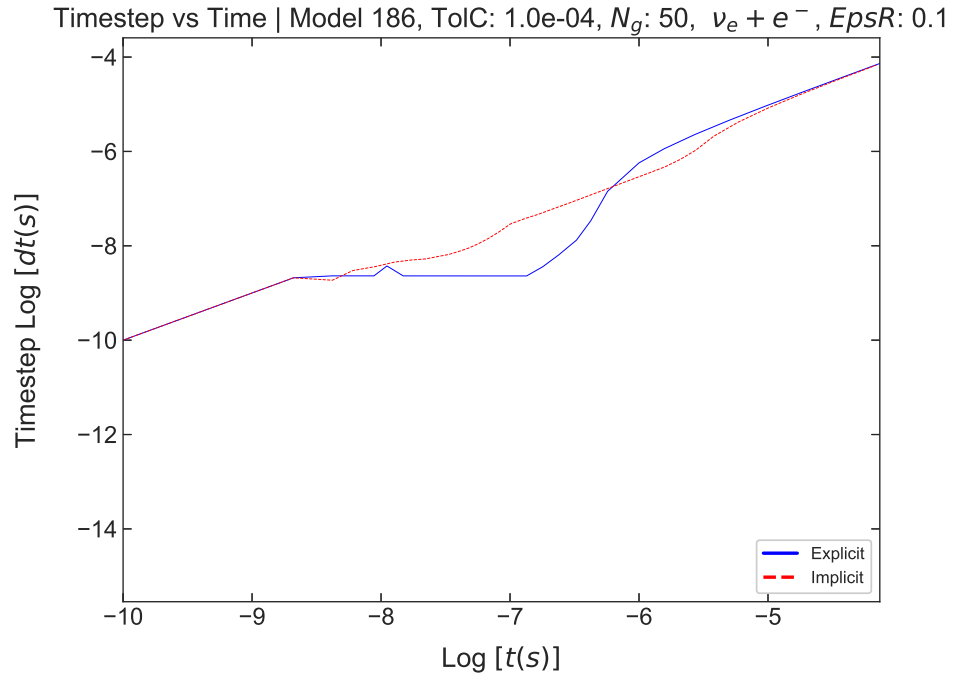


Figure 5.22: Timestep vs time for Model 186 - Intermediate Case.

Fast Case

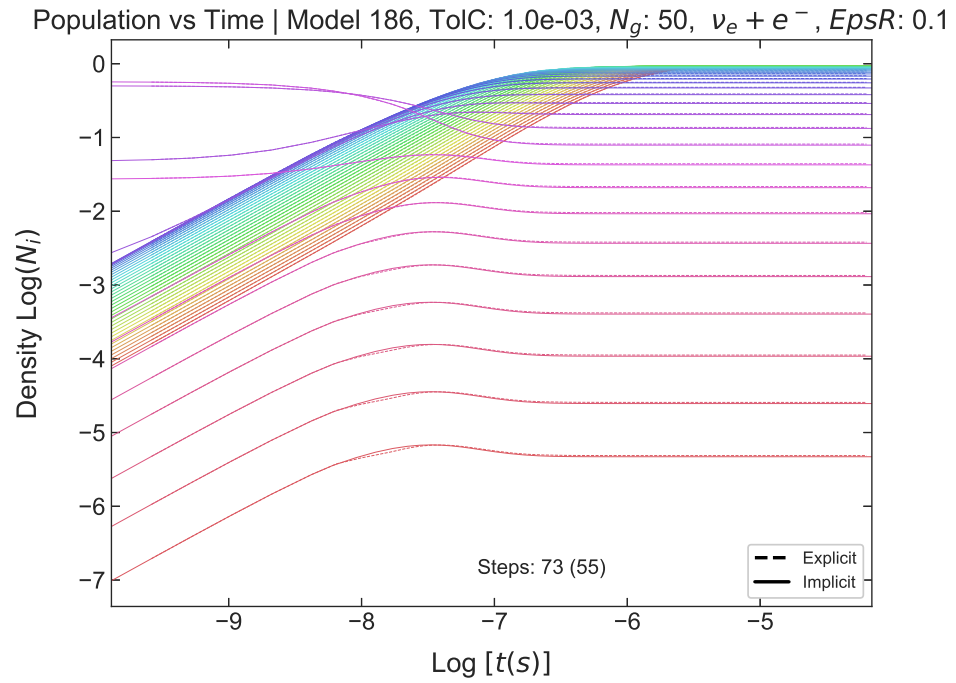


Figure 5.23: Population vs time for Model 186 - Fast Case.

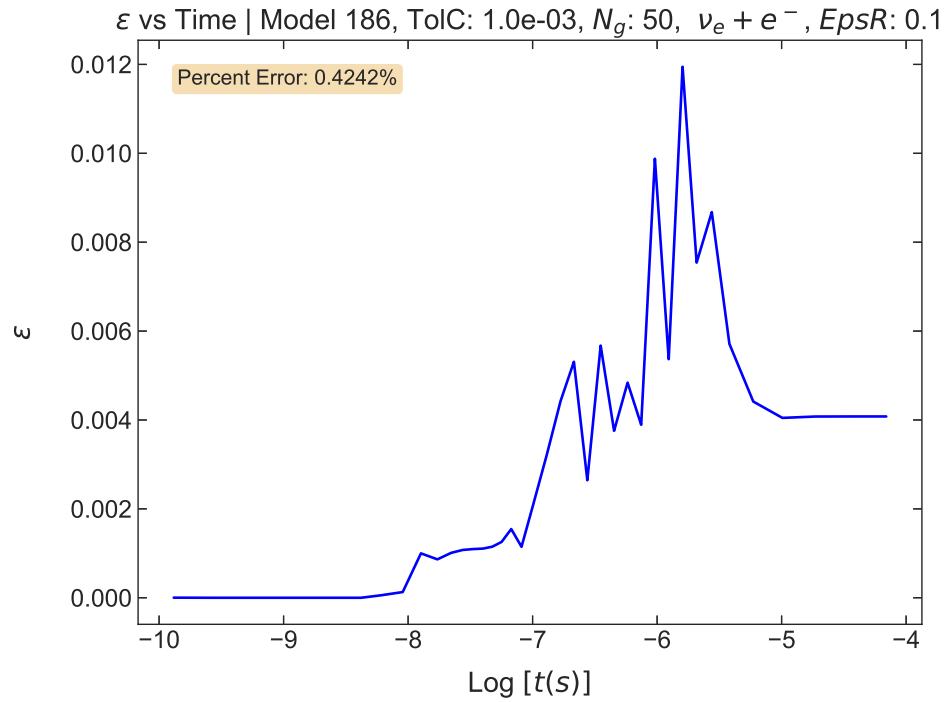


Figure 5.24: RMS vs time for Model 186 - Fast Case.

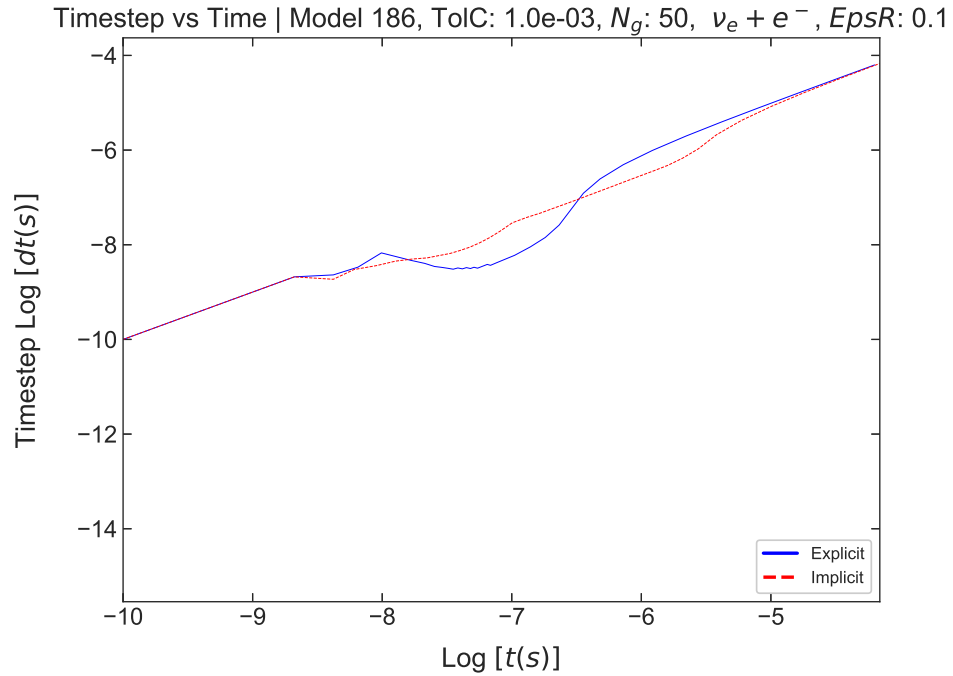


Figure 5.25: Timestep vs time for Model 186 - Fast Case.

Case	Steps Explicit	Steps Implicit	Error (%)
Accurate	209	55	0.0261
Intermediate	175	55	0.0771
Fast	73	55	0.4242

Table 5.2: Summary of steps and error for Model 186.

5.3.3 Model 213 Analysis

Similarly, we can provide an analysis of Model 213, for comparison.

Accurate Case

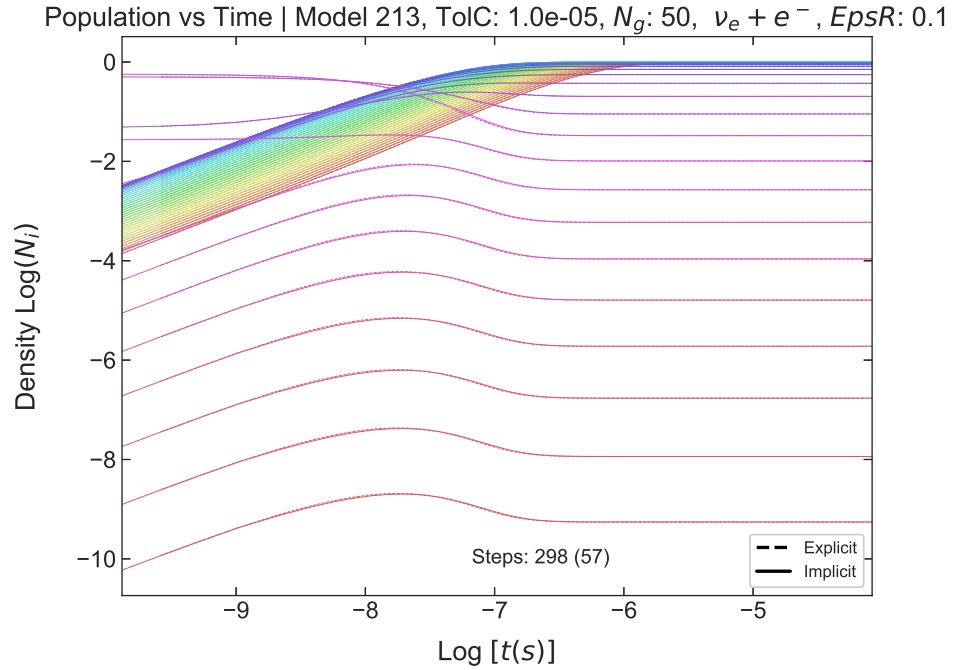


Figure 5.26: Population vs time for Model 213 - Accurate Case.

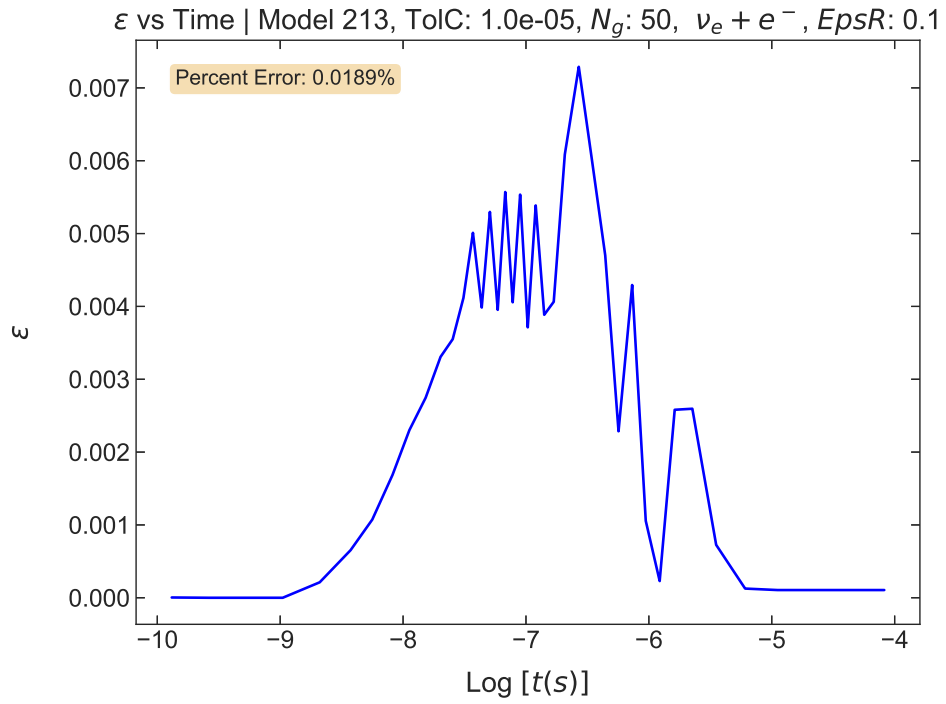


Figure 5.27: RMS vs time for Model 213 - Accurate Case.

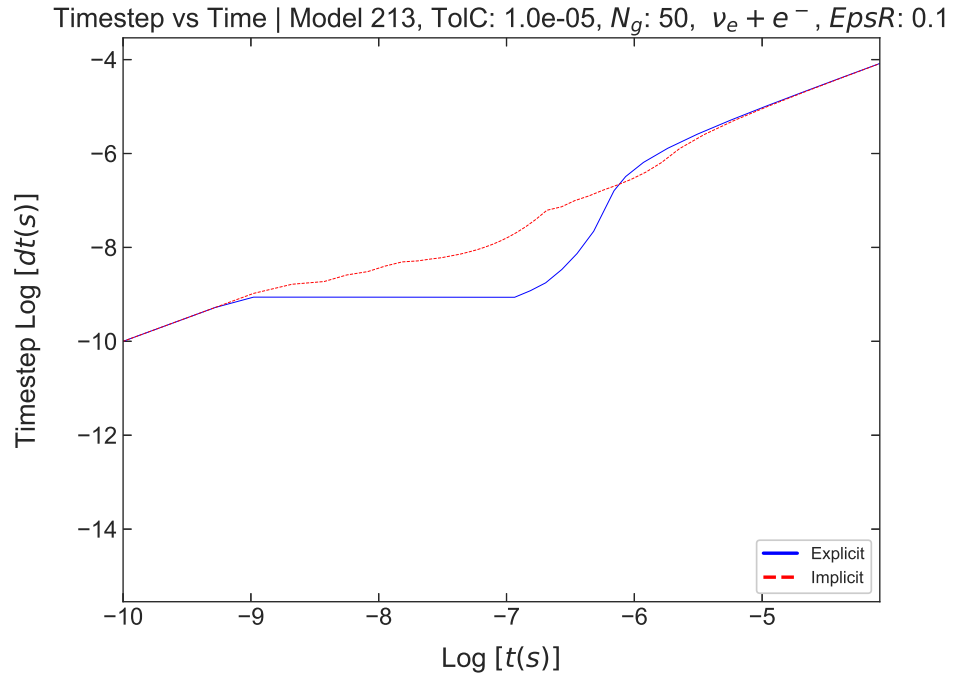


Figure 5.28: Time step vs time for Model 213 - Accurate Case.

Intermediate Case

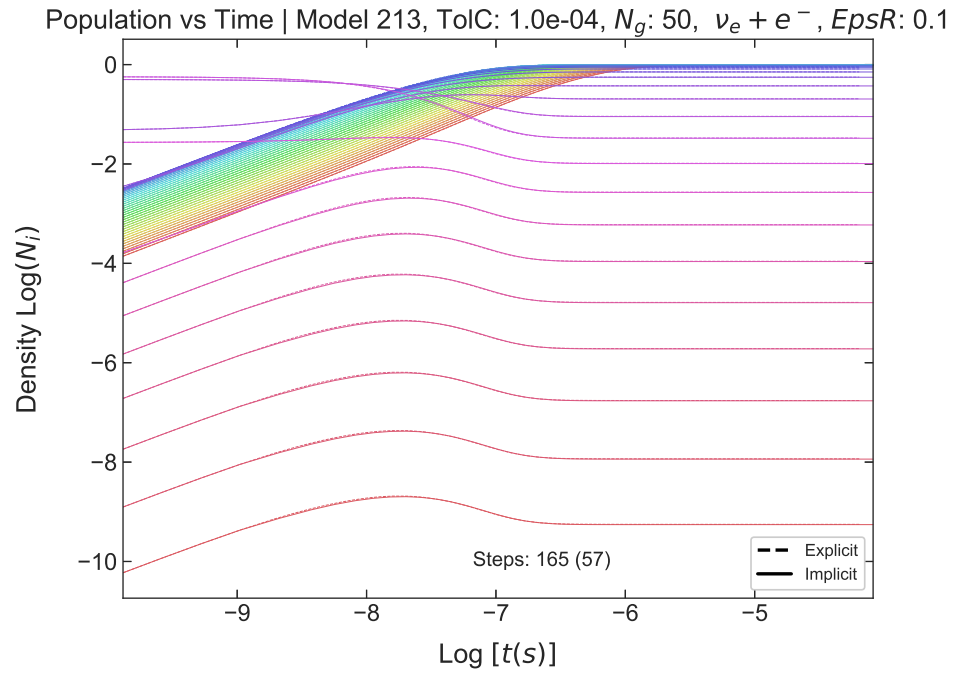


Figure 5.29: Population vs time for Model 213 - Intermediate Case.

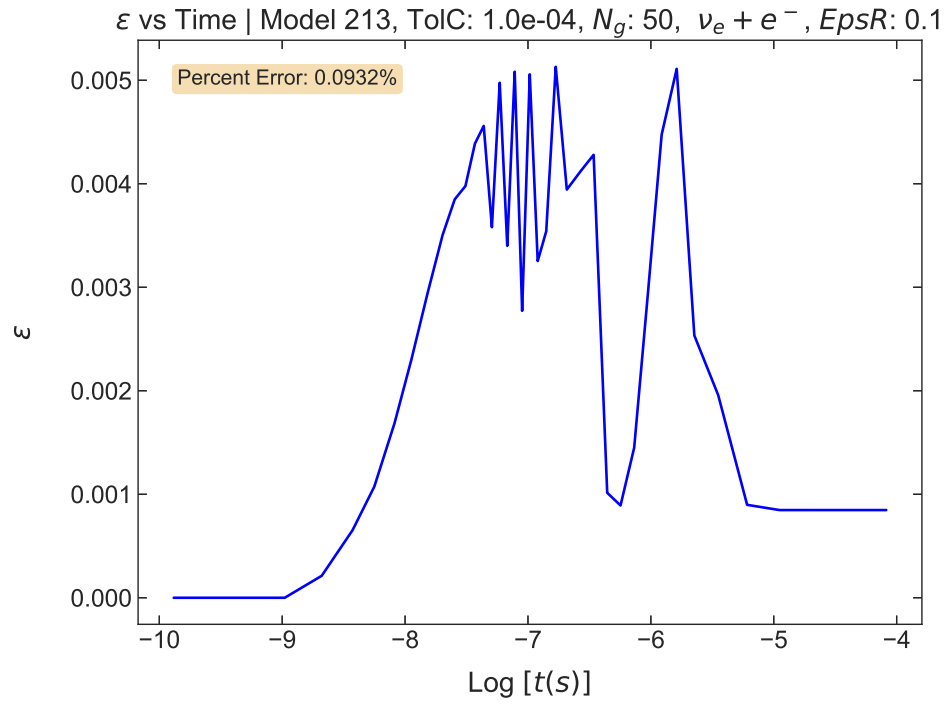


Figure 5.30: RMS vs time for Model 213 - Intermediate Case.

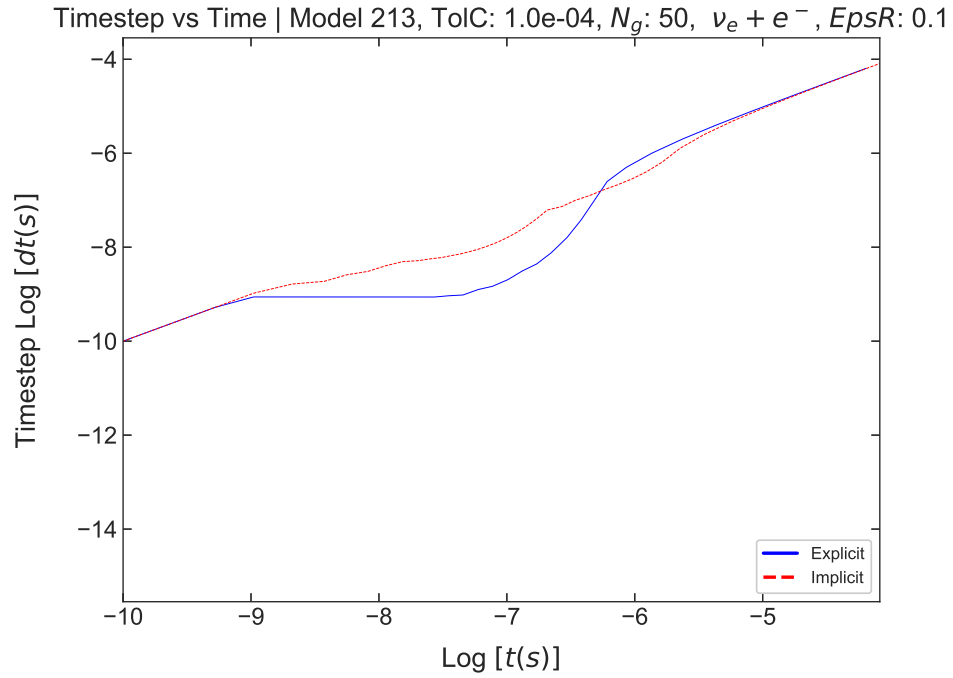


Figure 5.31: Time step vs time for Model 213 - Intermediate Case.

Fast Case

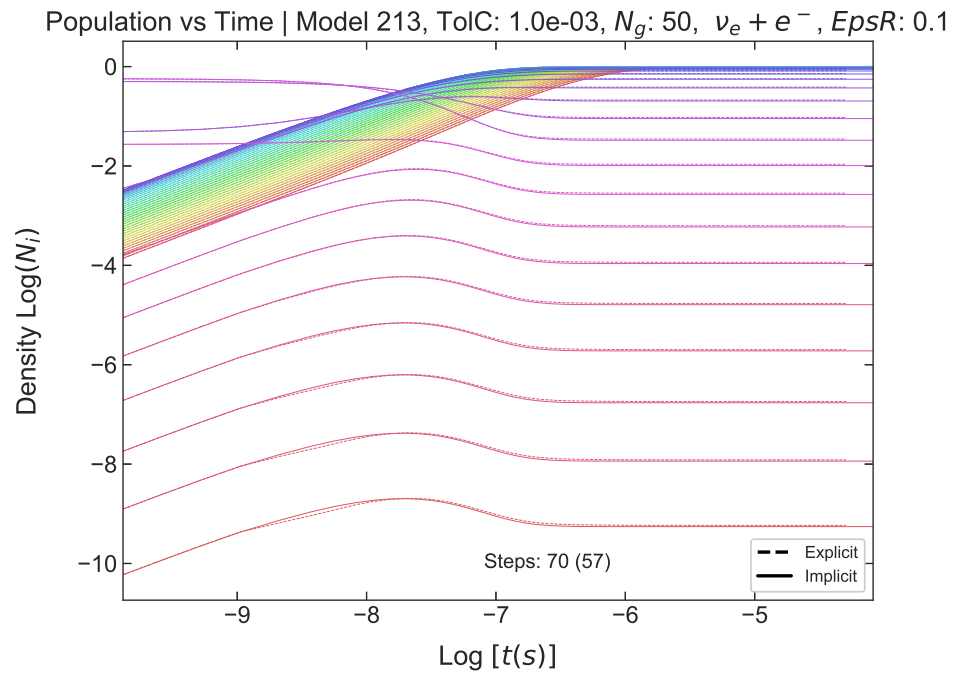


Figure 5.32: Population vs time for Model 213 - Fast Case.

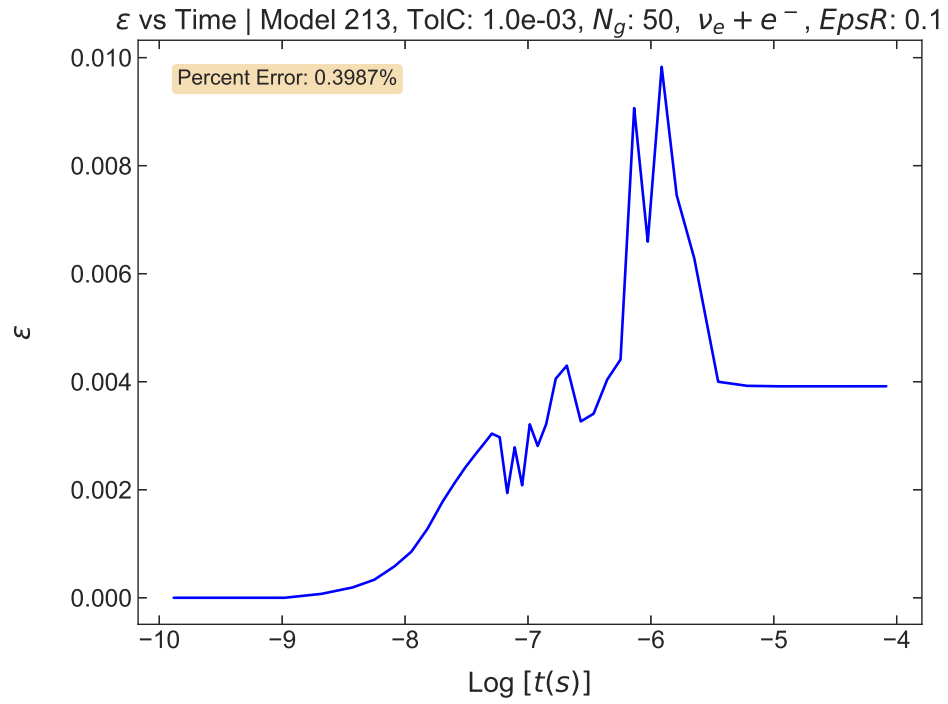


Figure 5.33: RMS vs time for Model 213 - Fast Case.

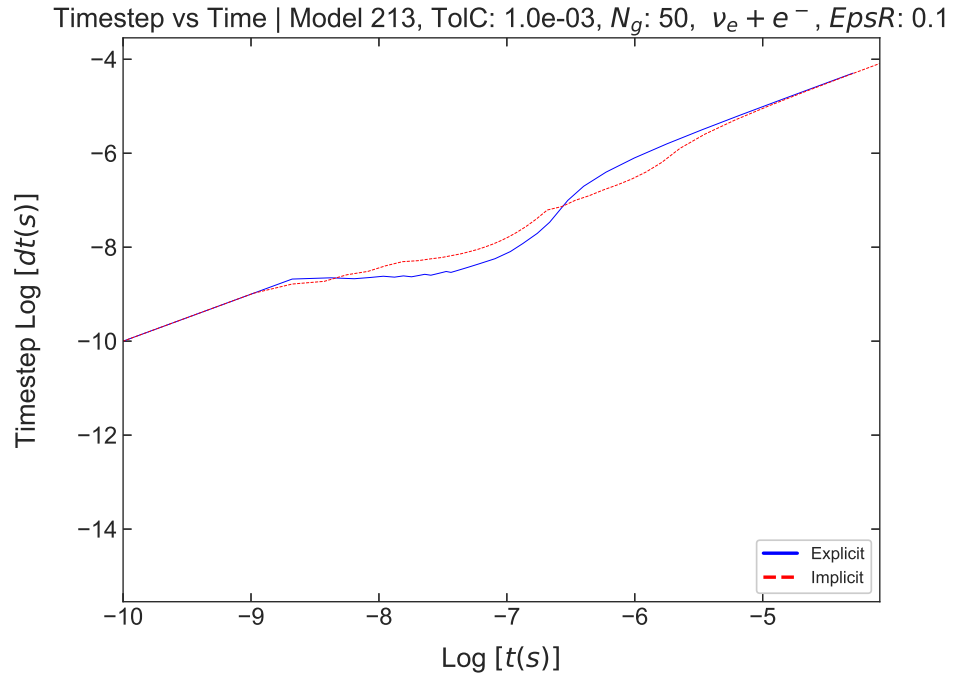


Figure 5.34: Time step vs time for Model 213 - Fast Case.

Case	Steps Explicit	Steps Implicit	Error (%)
Accurate	298	57	0.0189
Intermediate	165	57	0.0932
Fast	70	57	0.3987

Table 5.3: Summary of steps and error for Model 213.

5.3.4 Speed vs Accuracy

We can see in sections 5.3.1, 5.3.2, and 5.3.3 that we demonstrate that as we increase the speed of our explicit algorithms by decreasing our steps through increasing our tolerance conditions (TolC), we obtain a trade off of speed vs accuracy. The TolC conditions are tabulated in table 5.4.

Model / Case	Accurate	Intermediate	Fast
Model 81	10^{-8}	10^{-6}	10^{-4}
Model 186	10^{-5}	10^{-4}	10^{-3}
Model 213	10^{-5}	10^{-4}	10^{-3}

Table 5.4: Tolerance Conditions (TolC) for Each Model and Case.

We can necessitate a trade off of the accuracy by comparing the steps and error in tables 5.1, 5.2, 5.3. For speed, we can adopt Eq. 5.4 for a 50-Bin Network, as we see in 7.3 the speedup factor is approximately equal.

In the case of Model 213, the backward Euler implicit calculation took 57 integration steps. Referring to our earlier calculations in figures 5.26, 5.29, 5.32 the number of explicit asymptotic (Asy) integration steps taken for the Accurate, Intermediate, and Fast cases were 298, 165, and 70, respectively.

For the Accurate case of Model 213, we calculate the ratio of wall clock times for asymptotic integration relative to implicit integration using Eq. 5.4.

$$\frac{\Delta t_{EA}}{\Delta t_{BE}} \simeq 0.25 \times \frac{298}{57} \simeq 1.31.$$

This indicates that the explicit asymptotic integration is approximately $(1.31)^{-1} \simeq 0.77$ times as fast as the backward Euler calculation. This result implies that even though the explicit method requires approximately 5.2 times as many integration steps as the implicit method, it computes each

step about 4 times faster on the same system due to much easier matrix vector multiplication instead of costly matrix inversions.

For the intermediate calculation in Model 213, we proceed similarly:

$$\frac{\Delta t_{EA}}{\Delta t_{BE}} \simeq 0.25 \times \frac{165}{57} \simeq 0.72,$$

resulting in the calculation being about $(0.72)^{-1} \simeq 1.38$ times faster than the implicit BE calculation. Here, the explicit method requires roughly 2.9 times as many steps as the implicit method.

Lastly, for the fast model 213 example, we find:

$$\frac{\Delta t_{EA}}{\Delta t_{BE}} \simeq 0.25 \times \frac{70}{57} \simeq 0.31,$$

indicating that the fast asymptotic calculation is estimated to be about $(0.31)^{-1} \simeq 3.26$ times faster than the implicit BE calculation. In this scenario, the explicit method only requires about 1.2 times more steps than the implicit method.

So, while the explicit asymptotic integration often requires more steps, its faster computation per step on equivalent machines leads to significant reductions in overall computational time compared to the backward Euler method. This analysis shows how leveraging computational efficiency can compensate for an increased number of steps in certain dynamic models.

These calculations lead to the following table 5.5, which summarizes the wall clock times for the three models referenced across different cases:

Case	Model 81	Model 186	Model 213
Accurate	0.63	1.05	0.77
Intermediate	1.19	1.26	1.38
Fast	3.41	3.01	3.26

Table 5.5: Summary of wall clock times for Models 81, 186, 213

The explicit asymptotic calculation is similar in speed to the implicit reference calculation for the accurate case on a single CPU, but by speeding up the integration by choosing specific tolerance conditions from Eq. 3.7, we can take fewer explicit steps to increase an estimate 1-3 times faster for our calculations for the intermediate and fast cases, while maintaining an acceptable error.

Chapter 6

Neutrino Flavors

6.1 Introduction to Neutrino Flavors and Electron Scattering

In the results presented in Chapter 5, (Lackey-Stewart et al., 2024), as well as Lackey-Stewart (2020) only include simple neutrino electron scattering $\nu_e + e^-$. Here we introduce different flavors to the problem.

It is important to consider that neutrinos exist in three flavors: electron neutrinos (ν_e), muon neutrinos (ν_μ), and tau neutrinos (ν_τ), each associated with their respective charged leptons (electron e^- , muon μ^- , and tau τ^-). Additionally, for each neutrino, there exists a corresponding antineutrino defined as the electron antineutrino ($\bar{\nu}_e$), muon antineutrino ($\bar{\nu}_\mu$), and tau antineutrino ($\bar{\nu}_\tau$). We can introduce these various flavors into our problem to visualize how considering neutrino flavors incorporates additional realistic physics into the simulation at a fundamental level.

In this thesis, we use the notation $\nu_{\mu,\tau} + \mu^-, \tau^-$ and $\bar{\nu}_{\mu,\tau} + \mu^-, \tau^-$ to represent the scattering processes involving muon and tau neutrinos (and their antineutrinos) with their corresponding charged leptons. We did not consider muon or tau chemical potentials due to their negligible presence in the scenarios we are modeling. Our primary concern was to examine the impact of electron scattering processes, which are more relevant in core-collapse supernova environments.

6.1.1 $\bar{\nu}_e + e^-$ Scattering

Following $\nu_e + e^-$ in chapter 5, we can introduce AntiNeutrino Electron Scattering:

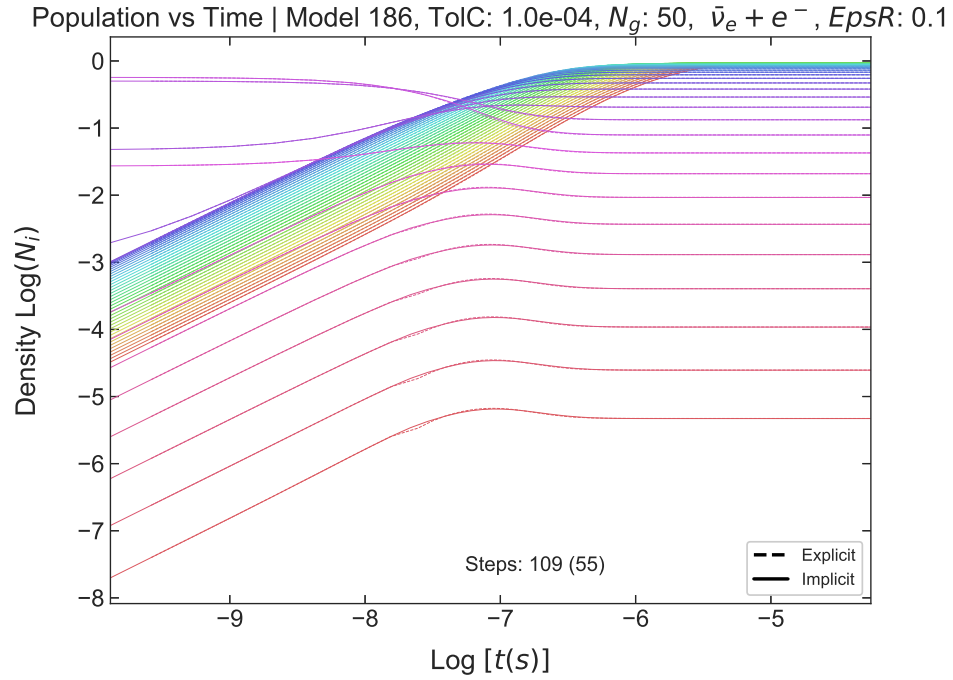


Figure 6.1: Population vs time for Model 186 - TolC = 10^{-4}

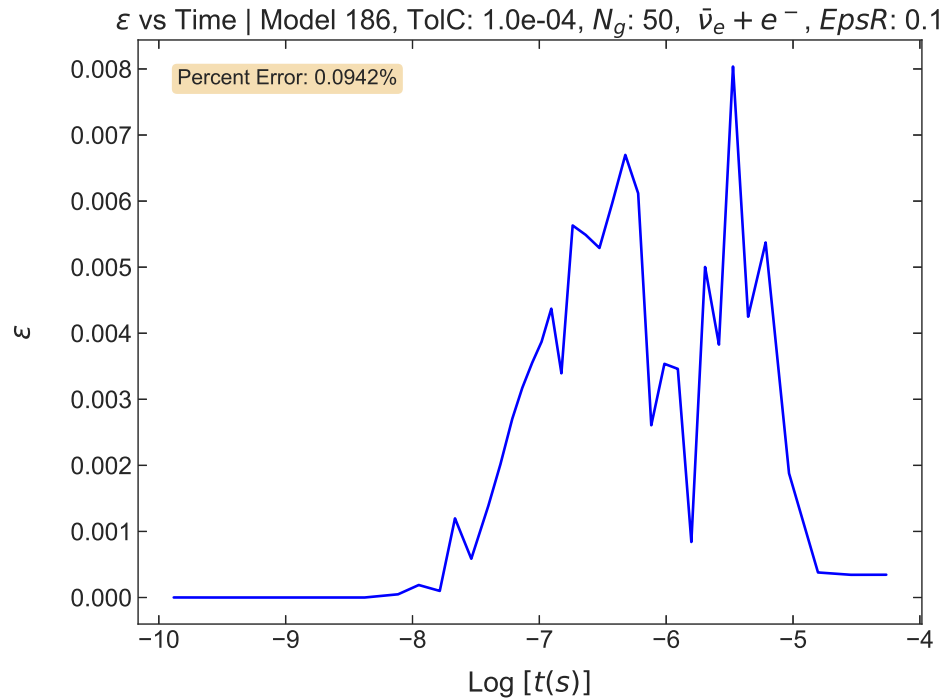


Figure 6.2: RMS vs time for Model 186 - TolC = 10^{-4}

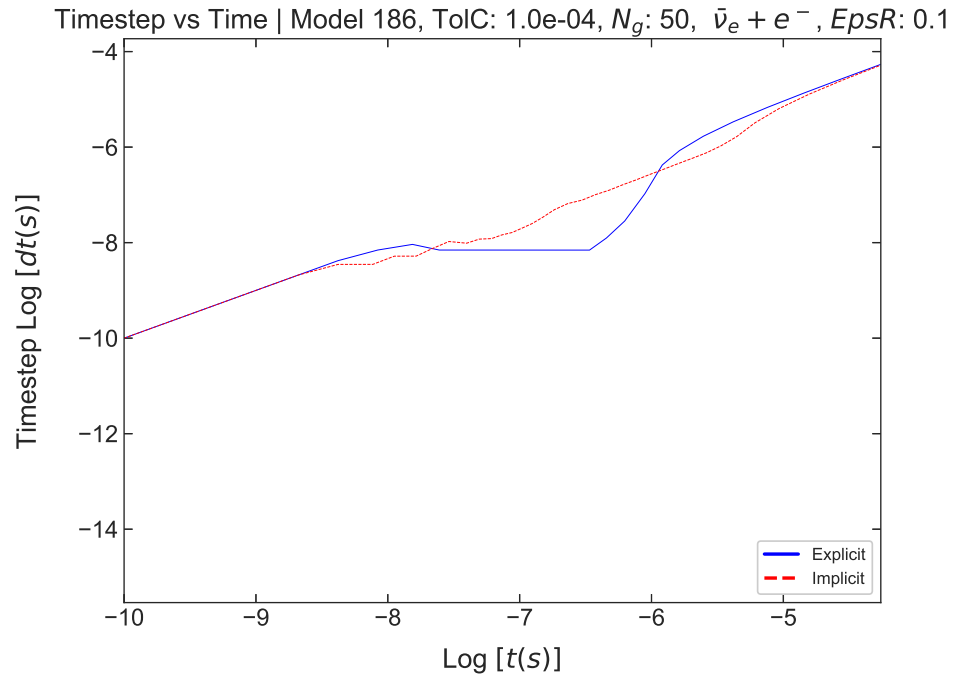


Figure 6.3: Time step vs time for Model 186 - TolC = 10^{-4}

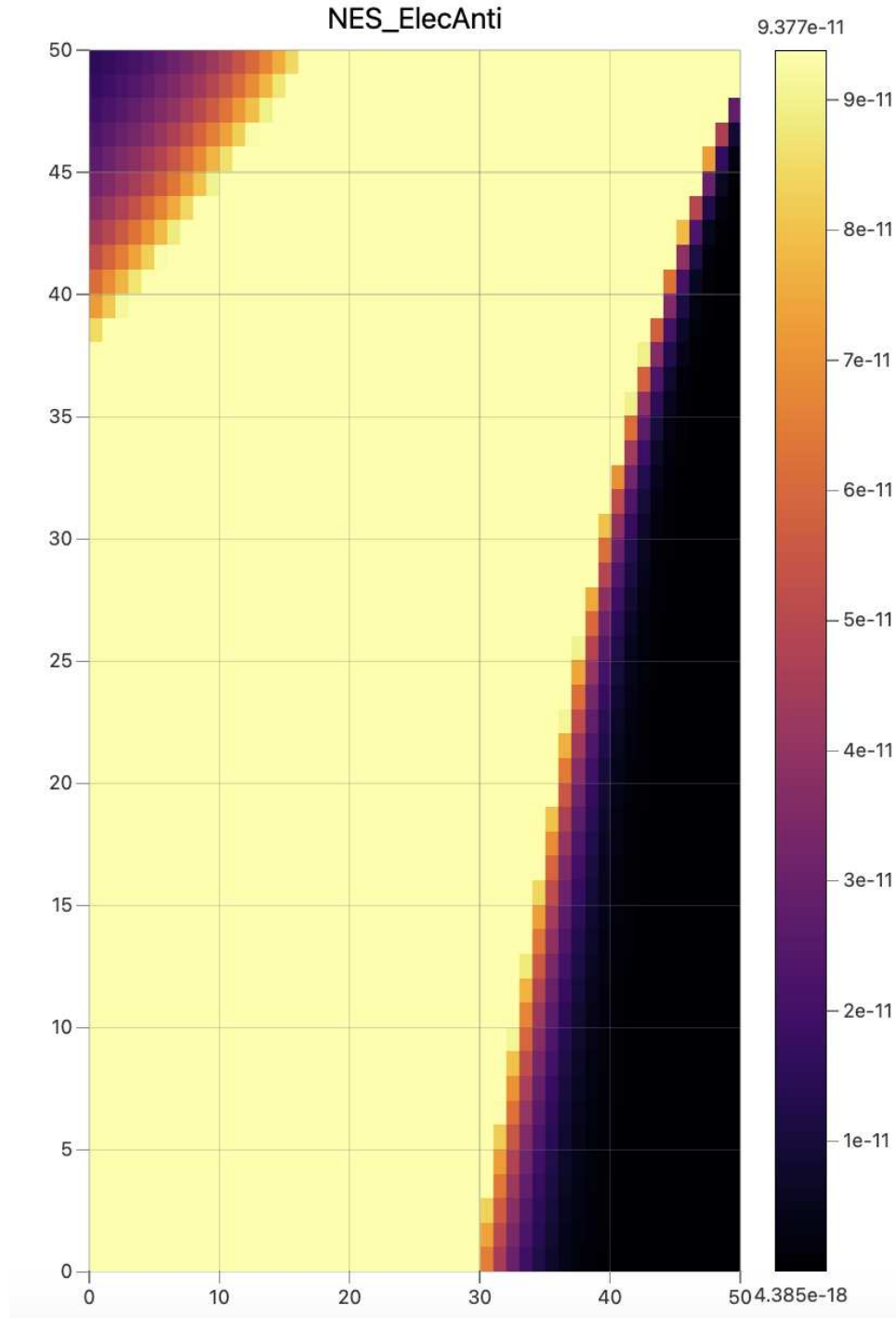


Figure 6.4: Heatmap of Scattering Rates for $\bar{\nu}_e + e^-$

We can see here that the anti-neutrinos have a negligible effect, in comparison with Fig. 5.21.

6.1.2 $\bar{\nu}_{\mu,\tau} + \mu^-, \tau^-$ Scattering

Similarly we can show results for $\bar{\nu}_{\mu,\tau} + \mu^-, \tau^-$ scattering in fig. 6.5.

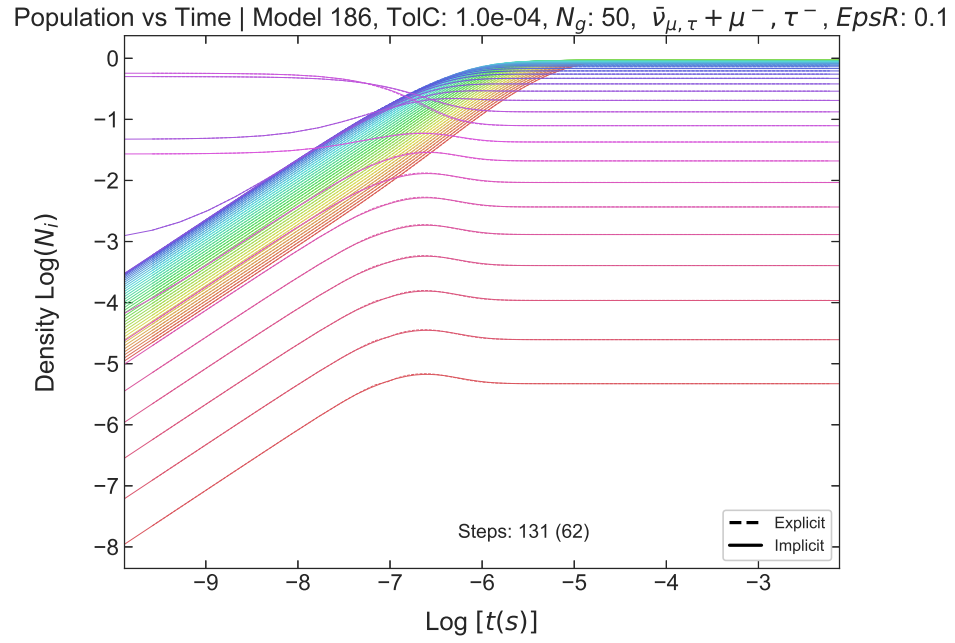


Figure 6.5: Population vs time for Model 186 - TolC = 10^{-4}

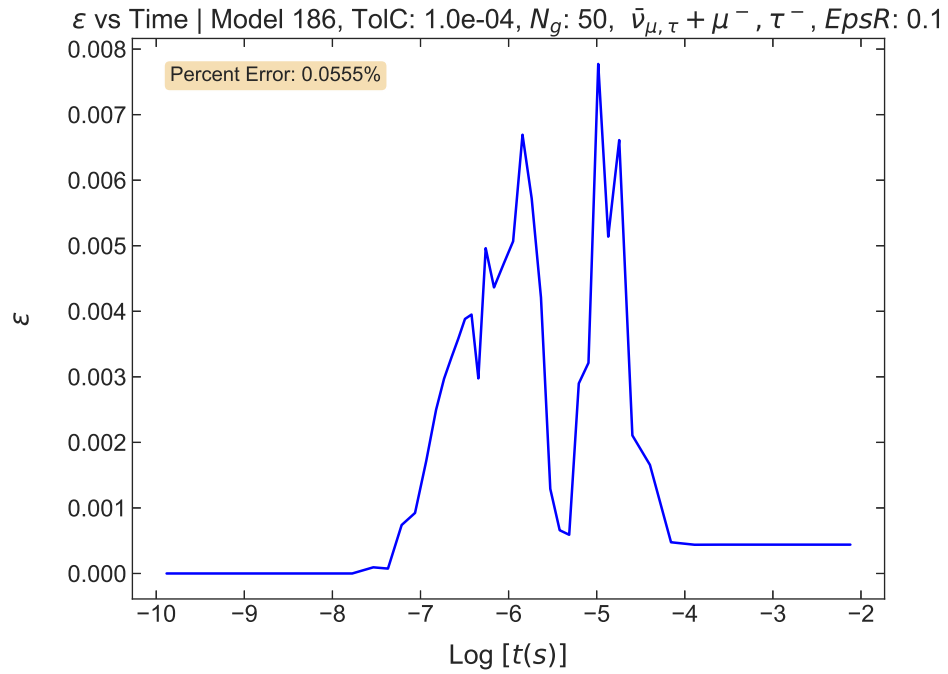


Figure 6.6: RMS vs time for Model 186 - TolC = 10^{-4}

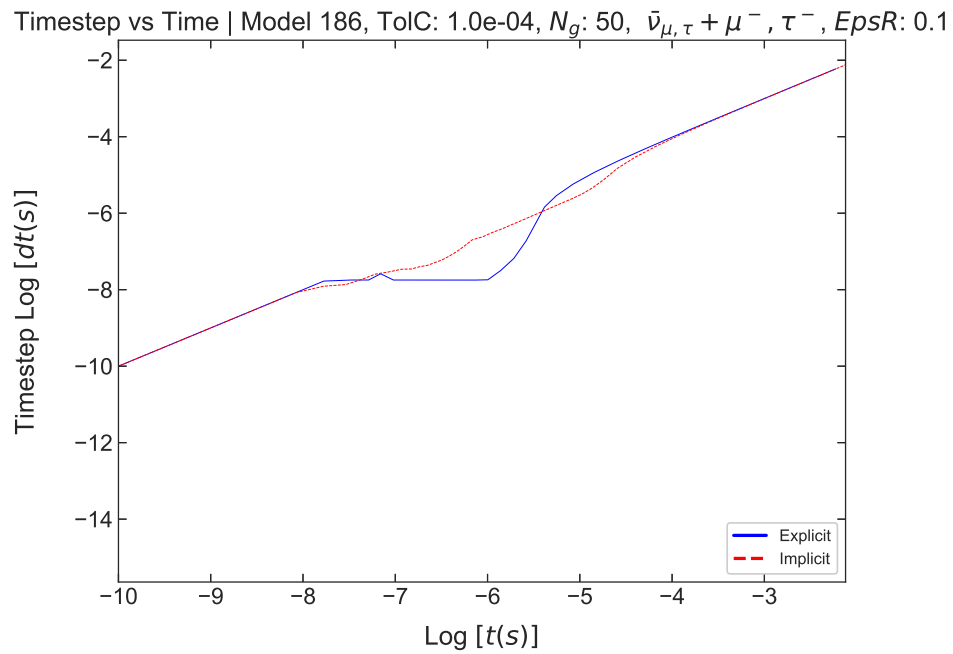


Figure 6.7: Time step vs time for Model 186 - TolC = 10^{-4}

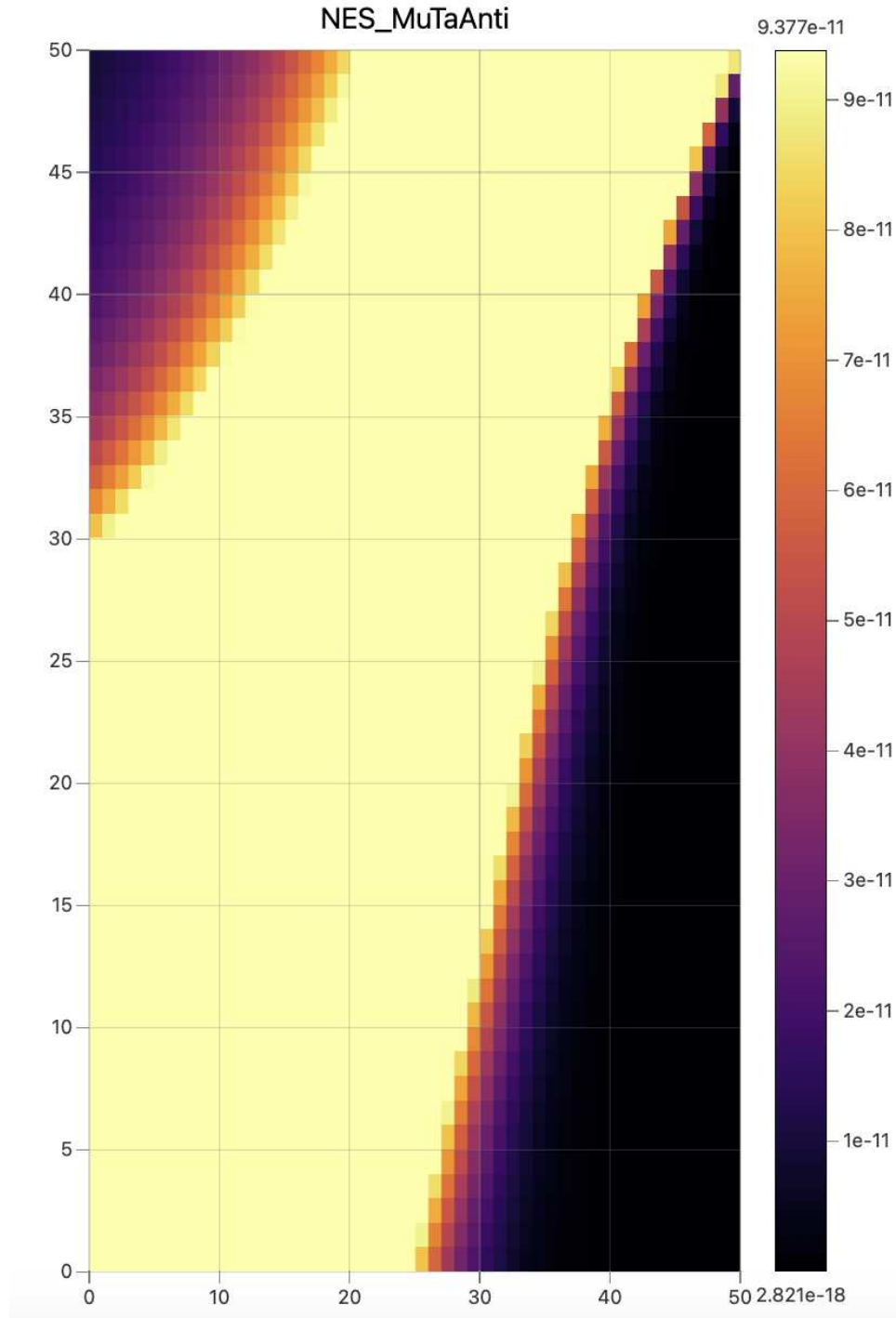


Figure 6.8: Heatmap of Scattering Rates for $\bar{\nu}_{\mu,\tau} + \mu^-, \tau^-$

We can see here the error is comparable with Fig. 5.21, however the solutions take longer to reach each equilibrium in reference to fig. 5.20.

6.1.3 $\nu_{\mu,\tau} + \mu^-, \tau^-$ Scattering

Results for $\nu_{\mu,\tau} + \mu^-, \tau^-$ are as follows:

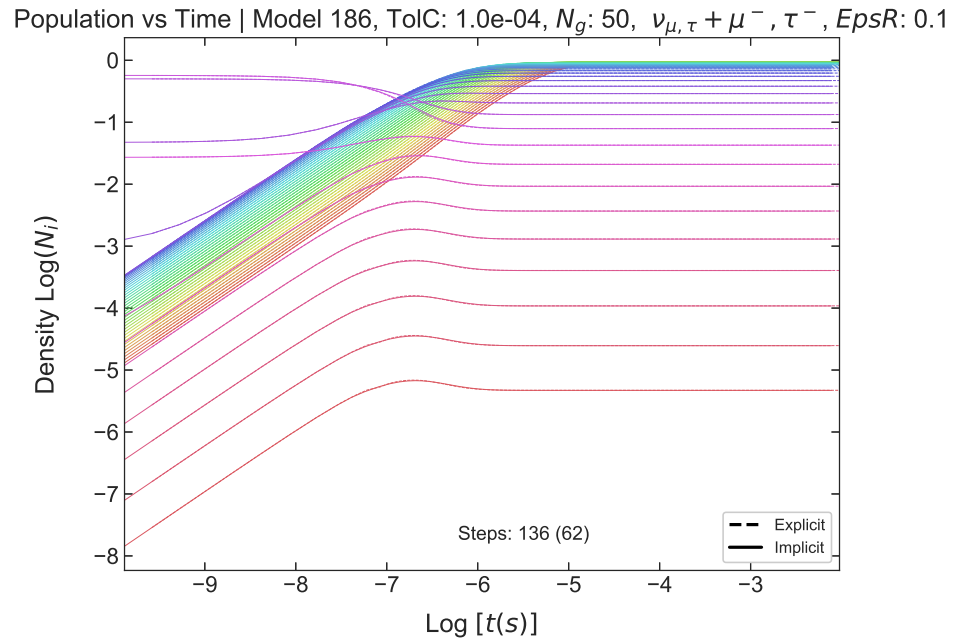


Figure 6.9: Population vs time for Model 186 - TolC = 10^{-4}

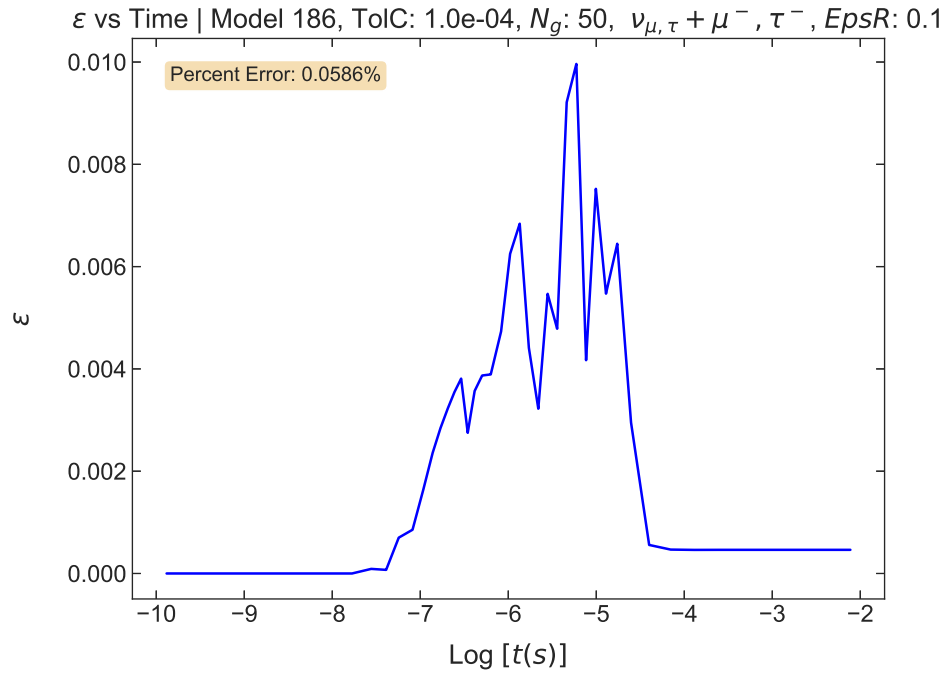


Figure 6.10: RMS vs time for Model 186 - TolC = 10^{-4}

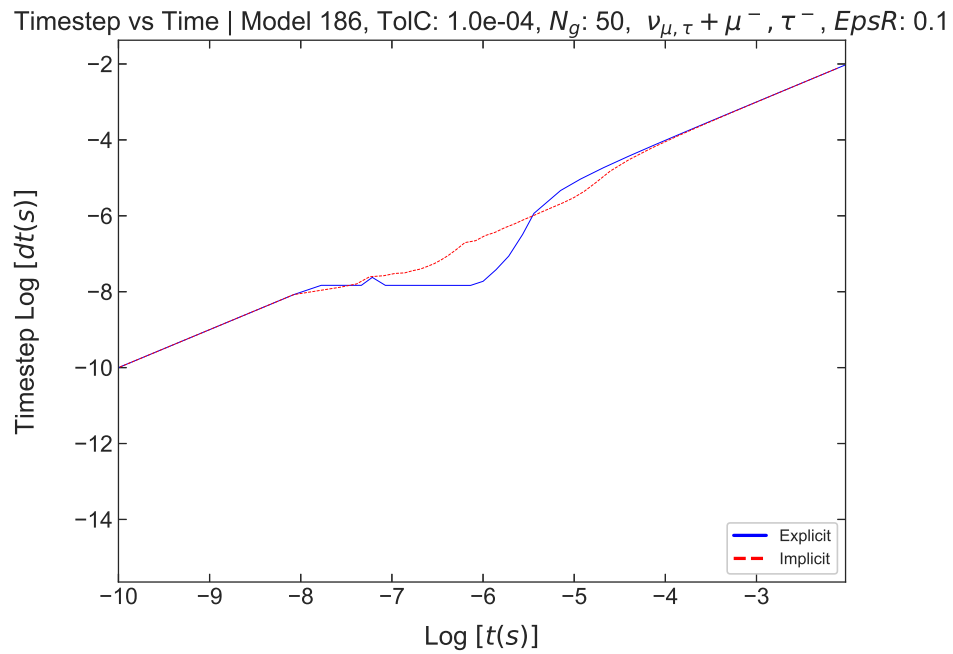


Figure 6.11: Time step vs time for Model 186 - TolC = 10^{-4}

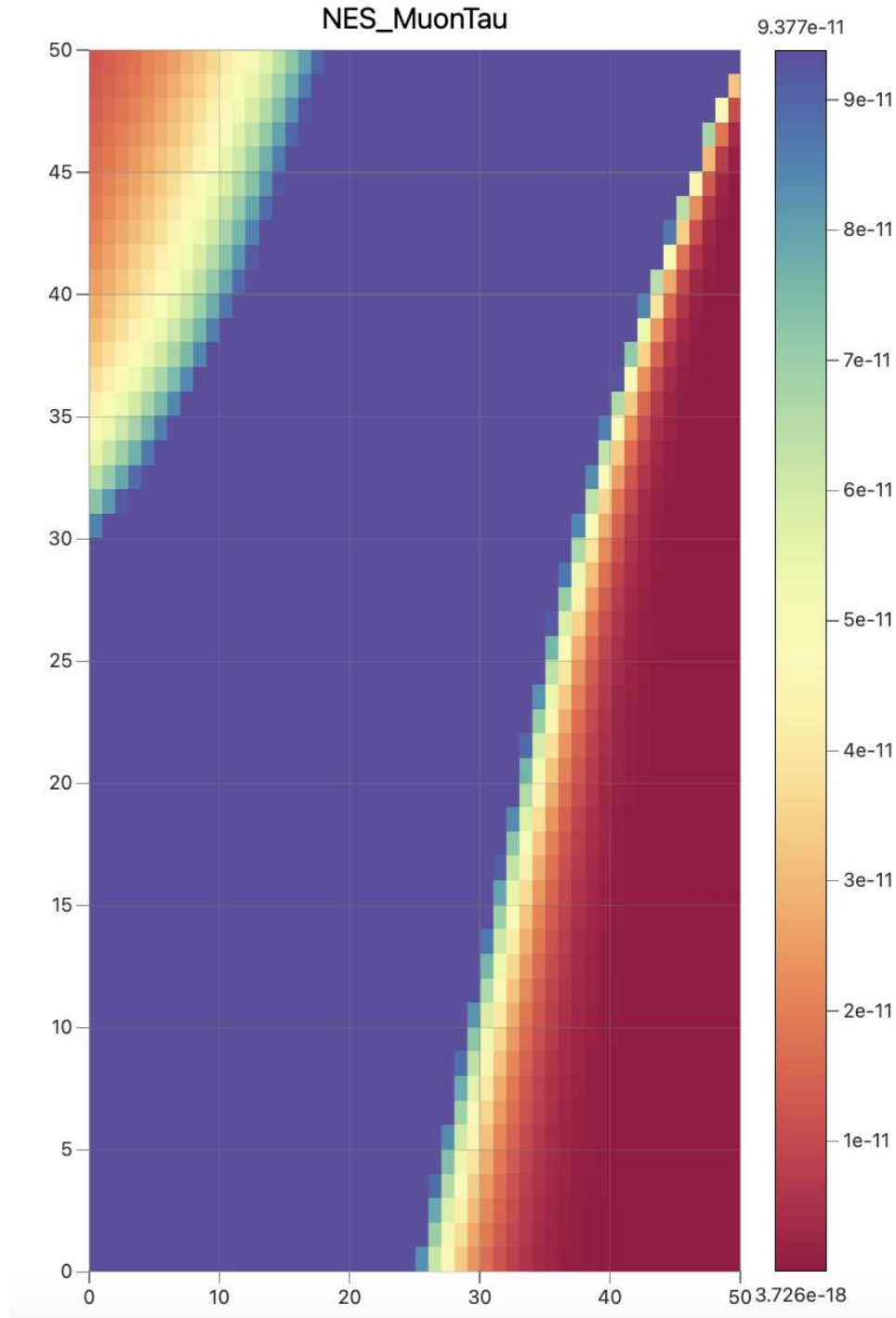


Figure 6.12: Heatmap of Scattering Rates for $\nu_{\mu,\tau} + \mu^-, \tau^-$

Similarly, the integration takes longer and the error is comparable to the results from fig. 6.6.

The results showcase that the neutrino flavors may introduce a small but negligible correction for the present solutions. This introduces a realistic ingredient in our simulations, with the possibility of capturing the rich interplay of muon and tau neutrinos with their associated leptons in more complex cases.

The mixing of different neutrino flavors introduced into our models exerted some influence on the dynamics of a system. Still, the level of error is reasonable which is crucial to maintain the integrity of the model under different conditions. However, if one wants to model the neutrino behavior in astrophysical environment with all necessary and sufficient details, a complete neutrino transport regime is necessary.

Oscillations of flavor make the calculation and transport of neutrinos complex because they take place when neutrinos change their flavor or state while propagating. Present models often make simplifications in these processes, which in turn may omit interactions that are crucial and may be responsible for a range of large-scale phenomena. Such as supernova explosion mechanisms or rates of cooling of neutron stars. While the full neutrino transport coupling is not included here, this introduces foundational work which FENN will build upon for a more realistic model.

Chapter 7

Scaling with Network Size

7.1 Analysis of Scaled Networks

In chapter 5 we presented the accurate, intermediate, and fast results for the standard scenario of 40 energy bins. After integration with WeakLib, we can now make the same analysis for increased network sizes at fixed resolution, giving an opportunity to enhance the complexity of our simulations even more. Note that this implies in the changing the size of our collision matrix in Eq. 2.35, letting us handle more detailed interactions and higher energy resolutions.

This section gives a detailed comparative analysis of the network scaling process with respect to size for Model 186, and elaborates on the effect of increasing network size on the system dynamics. Making our comparative study with larger networks, it is possible to appreciate scaling with system size in terms of both complexity and computational demand. We analyze and compare results using network sizes of 40, 50, 80, 100, 130, 160, and 180, energy bins, comparing Population vs. Time, Epsilon vs. Time, and Timestep vs. Time.

The following are similar figures from chapter 5, with the mentioned energy sizes.

7.1.1 Network Size 40

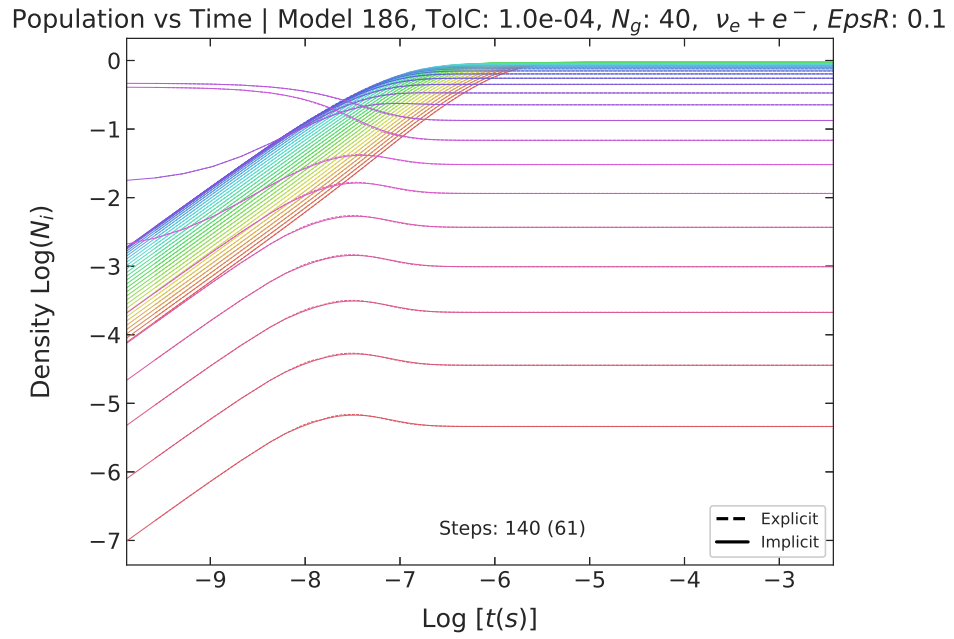


Figure 7.1: Population vs. time for Network Size 40.

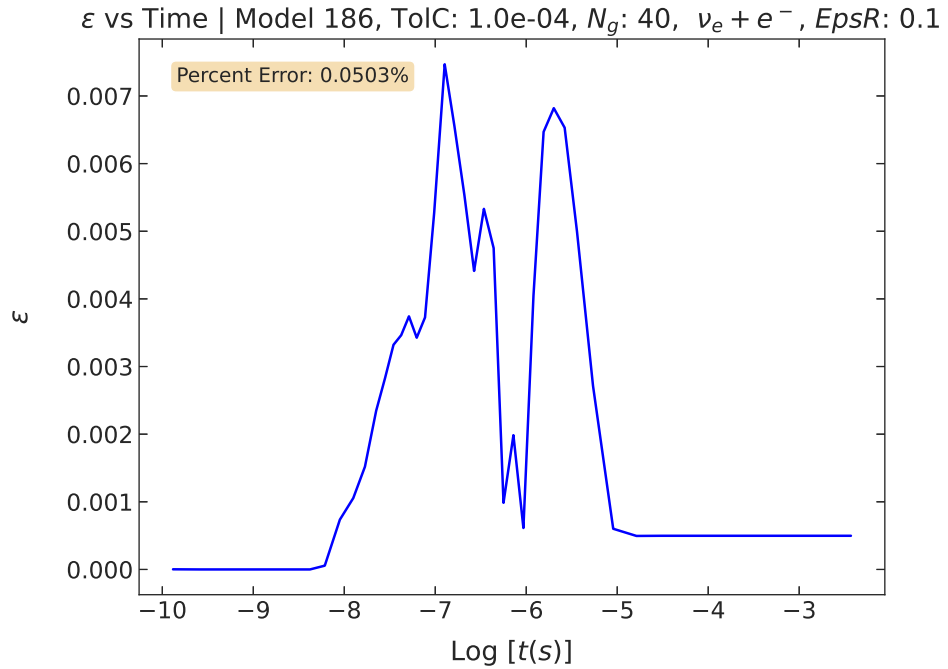


Figure 7.2: Epsilon vs. time for Network Size 40.

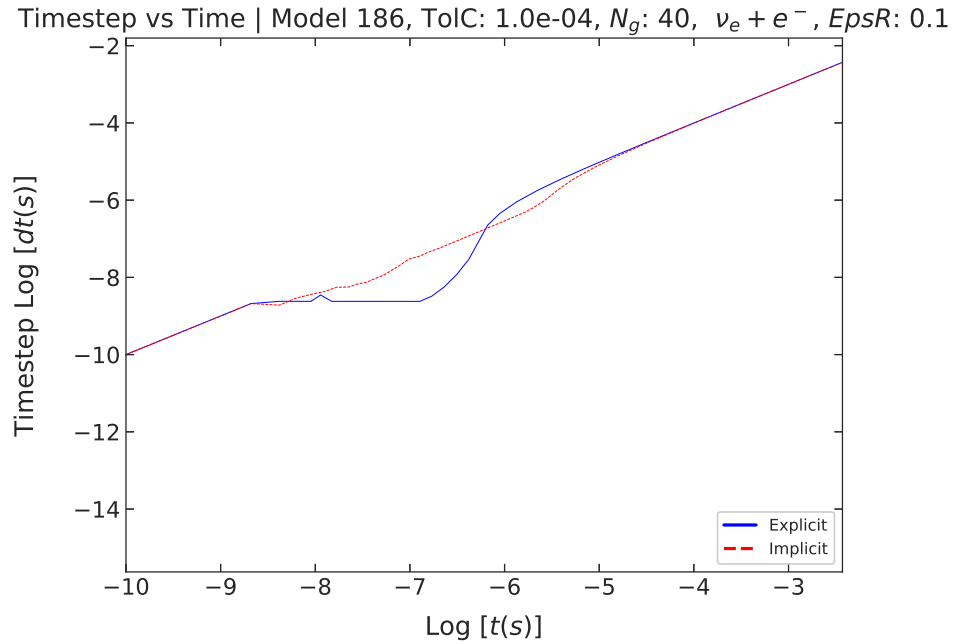


Figure 7.3: Timestep vs. time for Network Size 40.

7.1.2 Network Size 50

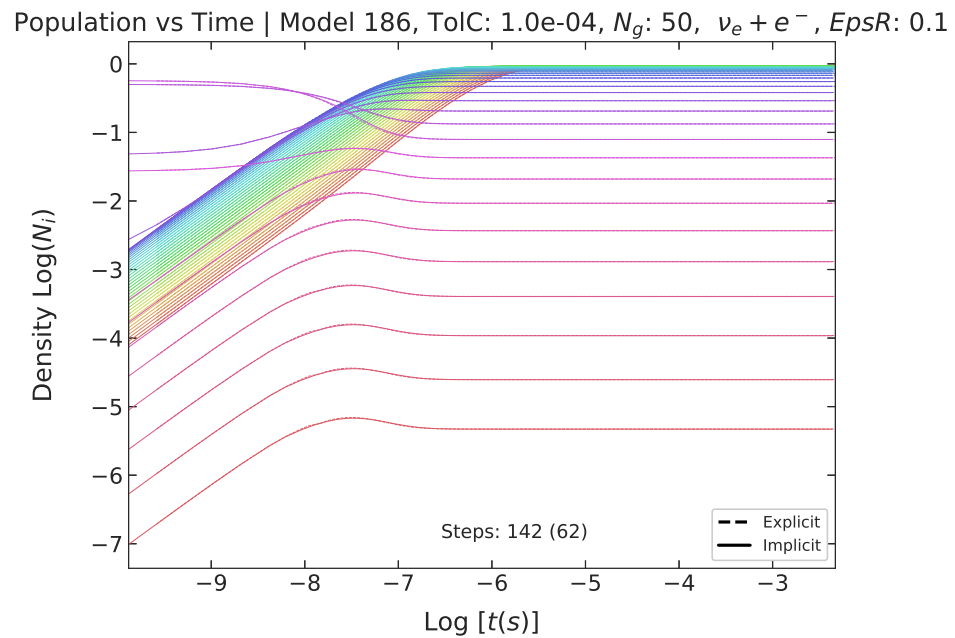


Figure 7.4: Population vs. time for Network Size 50.

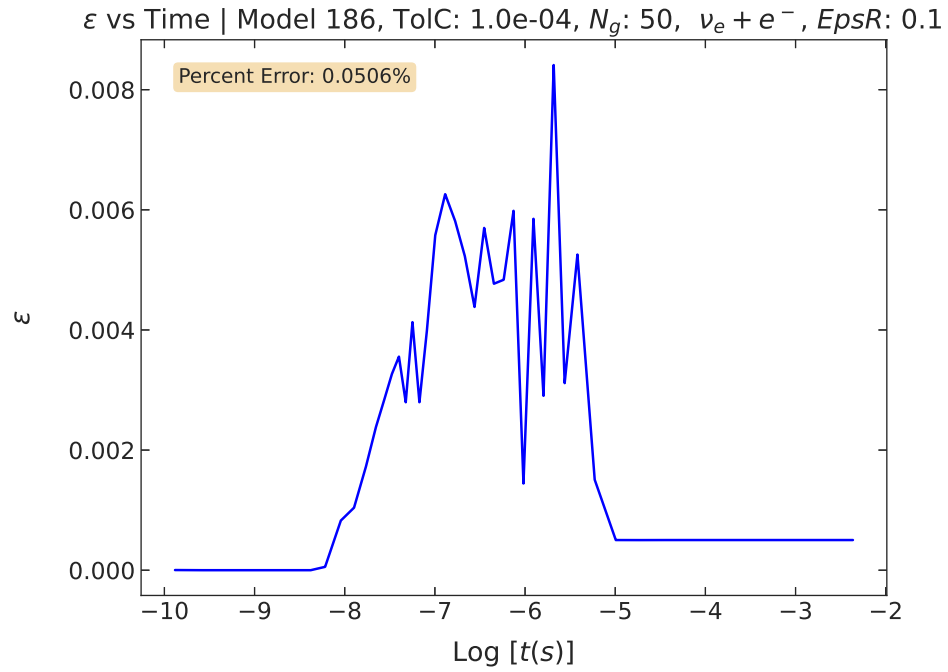


Figure 7.5: Epsilon vs. time for Network Size 50.

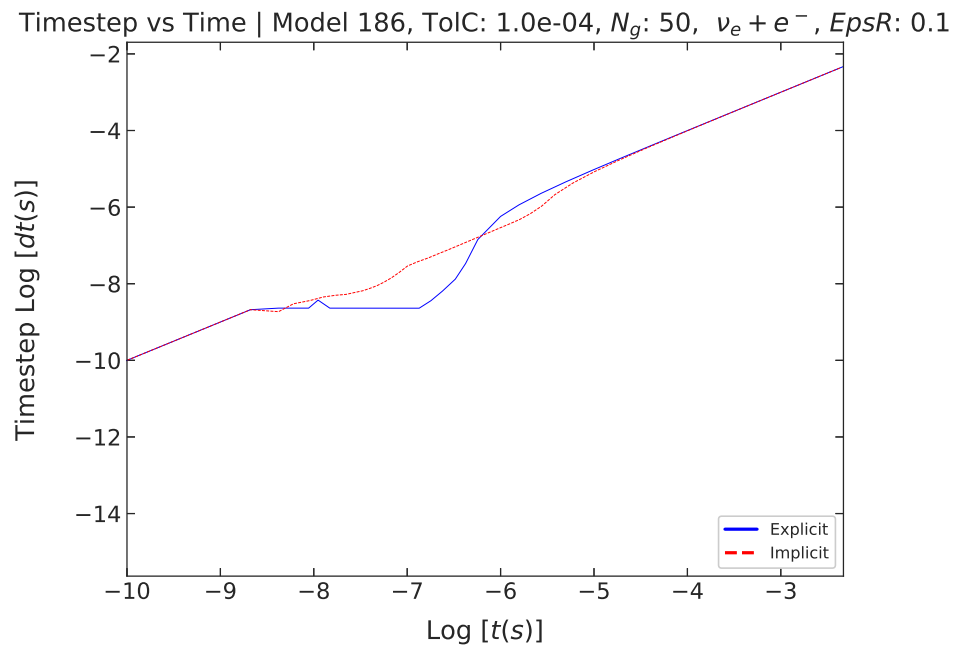


Figure 7.6: Timestep vs. time for Network Size 50.

7.1.3 Network Size 80

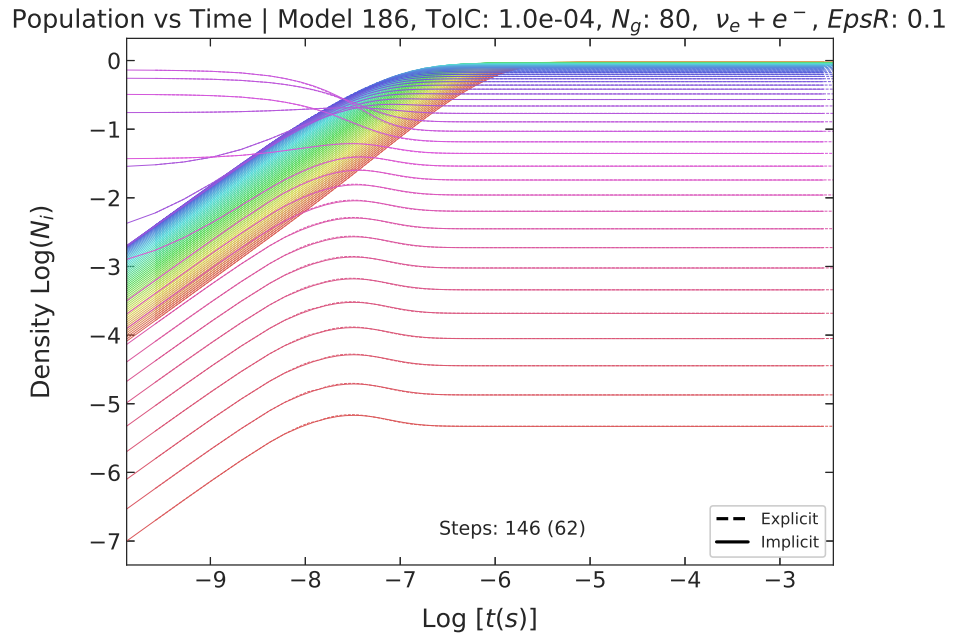


Figure 7.7: Population vs. time for Network Size 80.

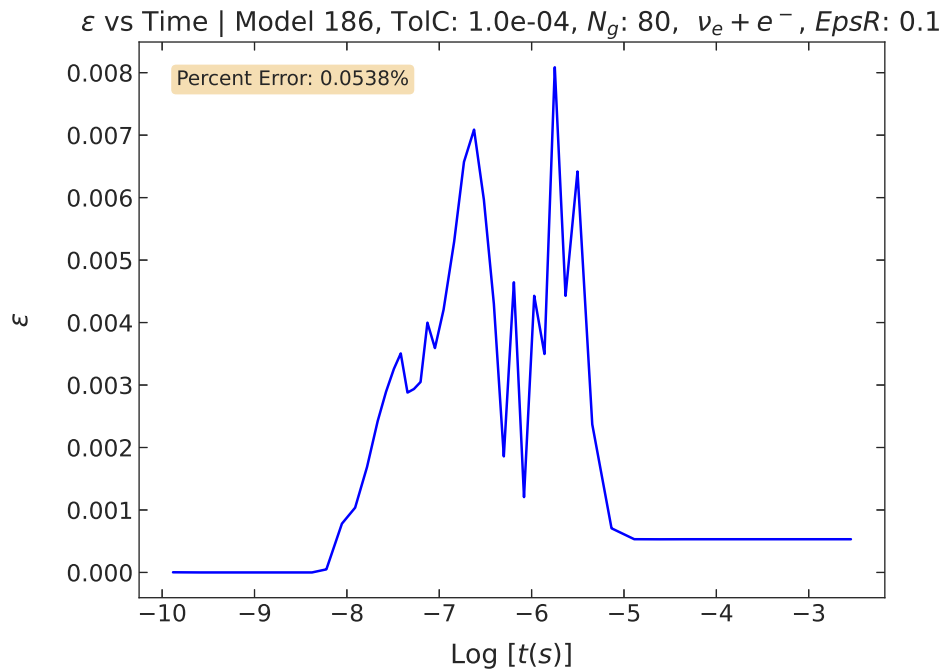


Figure 7.8: Epsilon vs. time for Network Size 80.

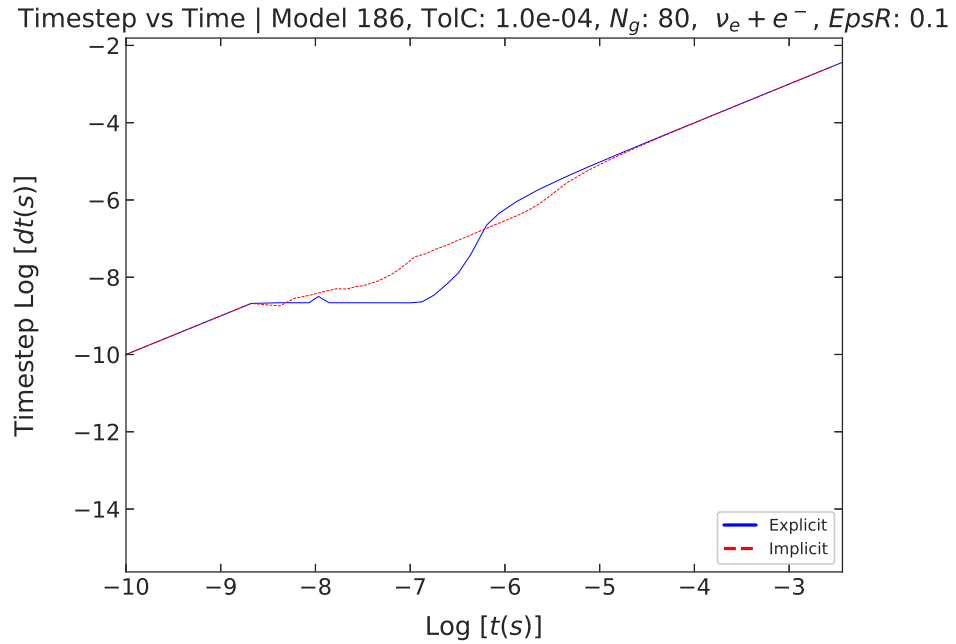


Figure 7.9: Timestep vs. time for Network Size 80.

7.1.4 Network Size 100

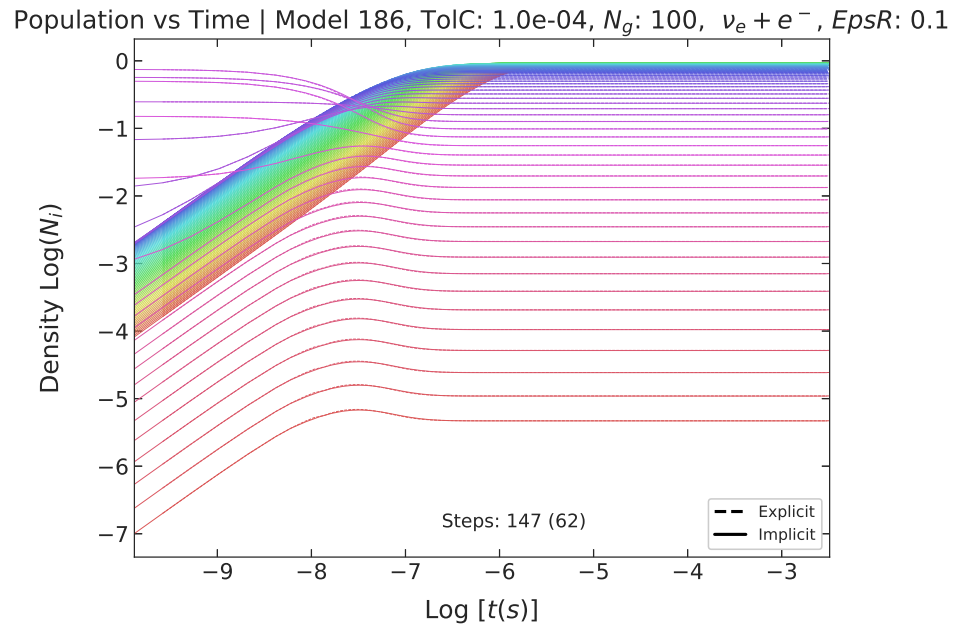


Figure 7.10: Population vs. time for Network Size 100.

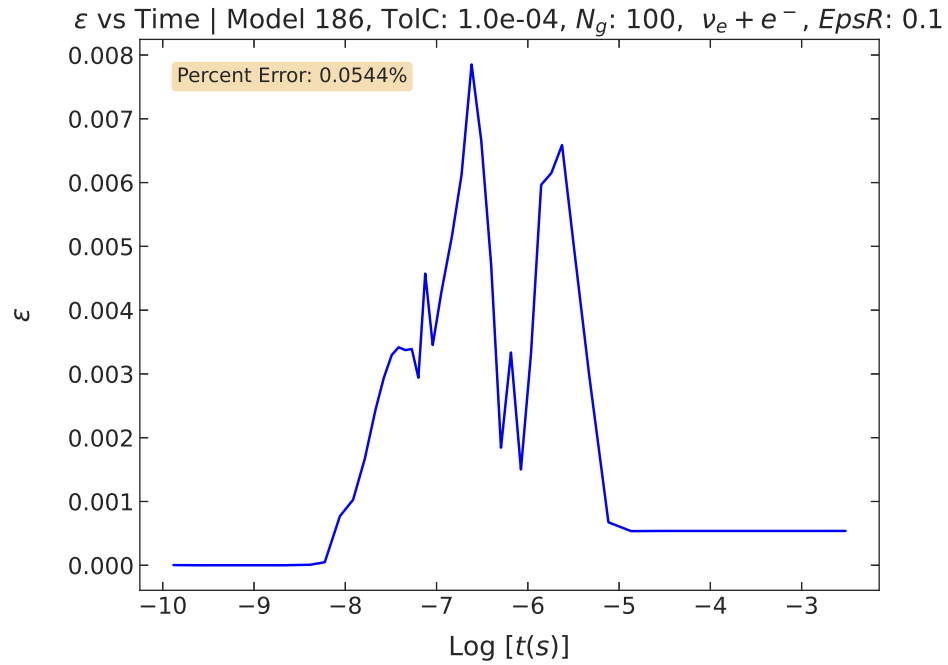


Figure 7.11: Epsilon vs. time for Network Size 100.

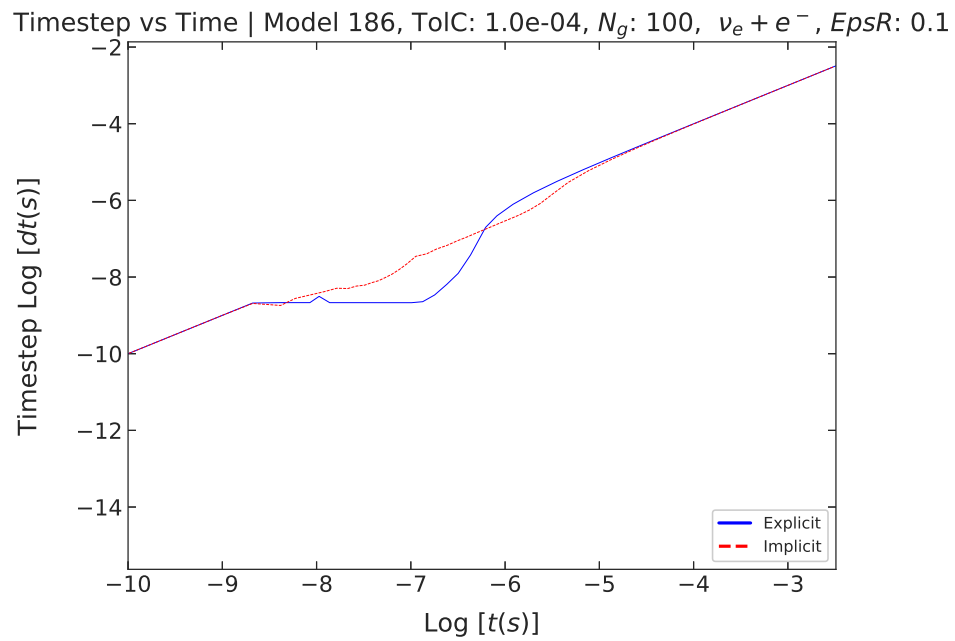


Figure 7.12: Timestep vs. time for Network Size 100.

7.1.5 Network Size 130

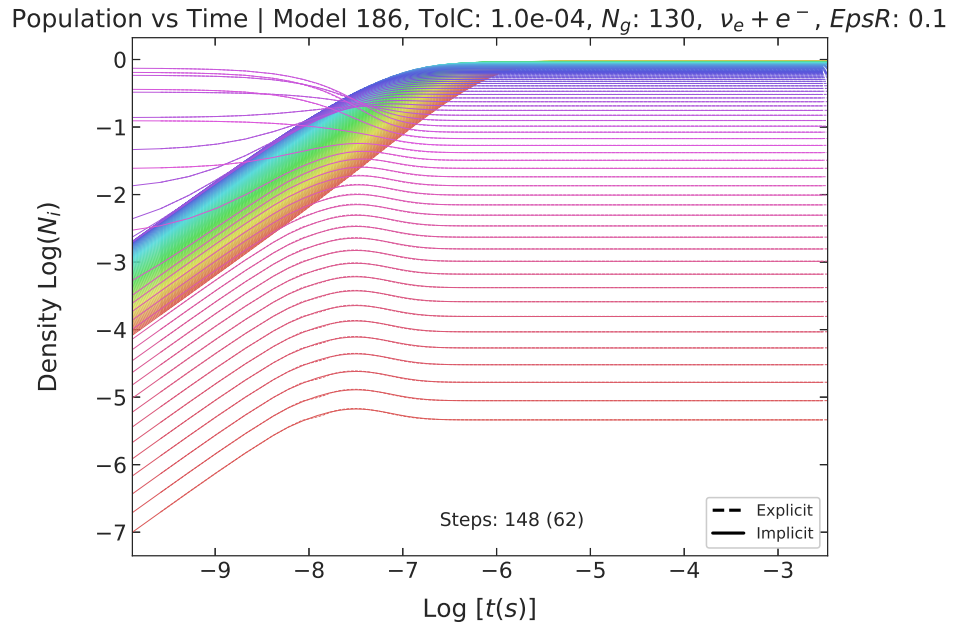


Figure 7.13: Population vs. time for Network Size 160.

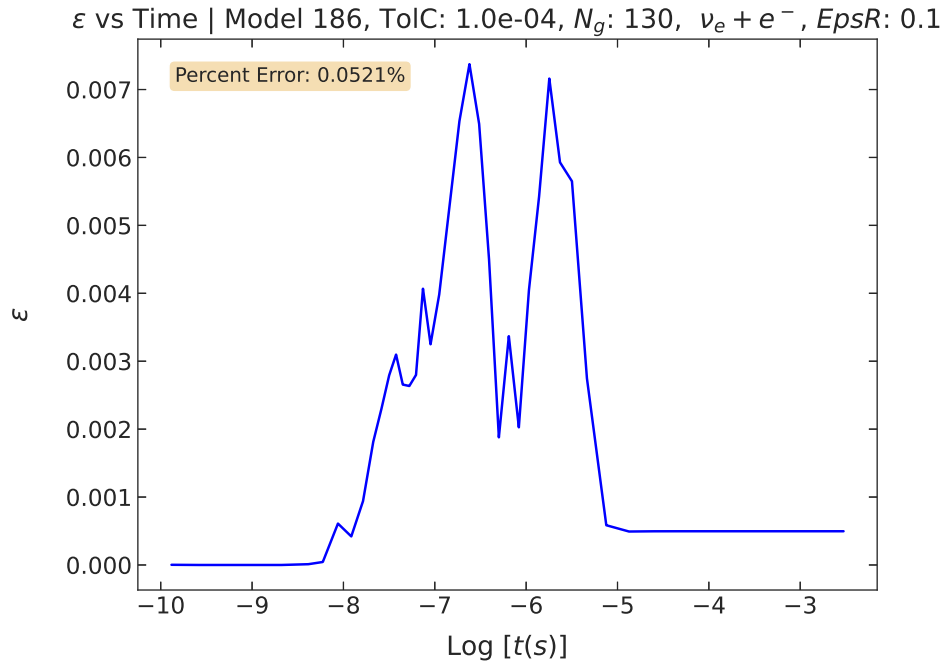


Figure 7.14: Epsilon vs. time for Network Size 160.

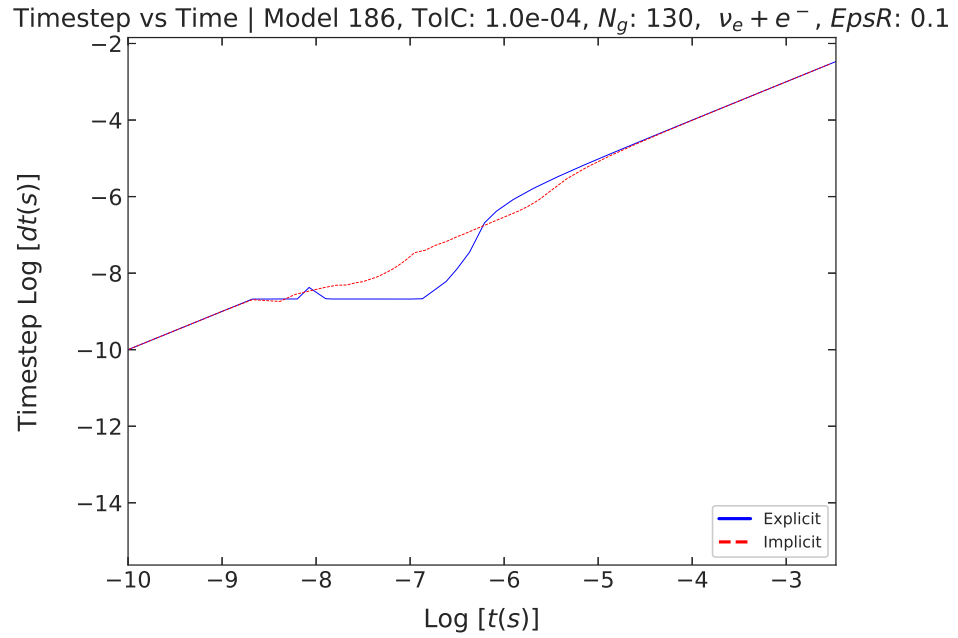


Figure 7.15: Timestep vs. time for Network Size 160.

7.1.6 Network Size 160

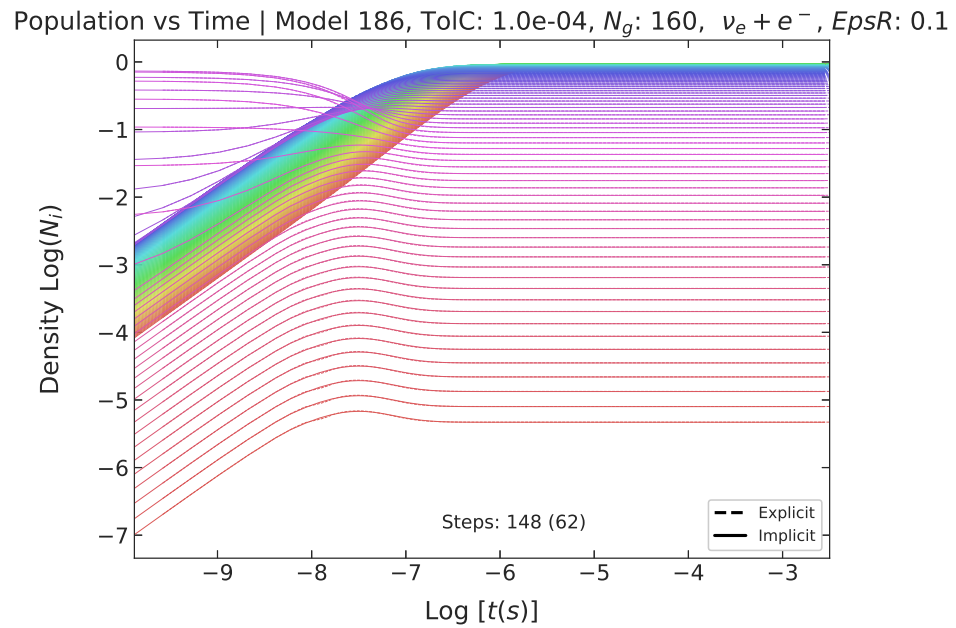


Figure 7.16: Population vs. time for Network Size 160.

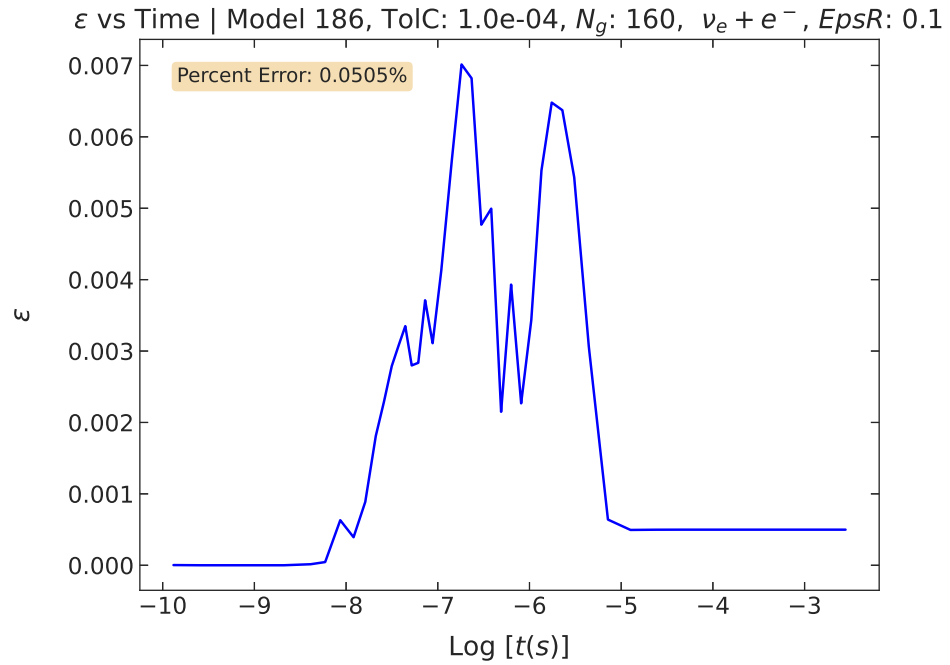


Figure 7.17: Epsilon vs. time for Network Size 160.

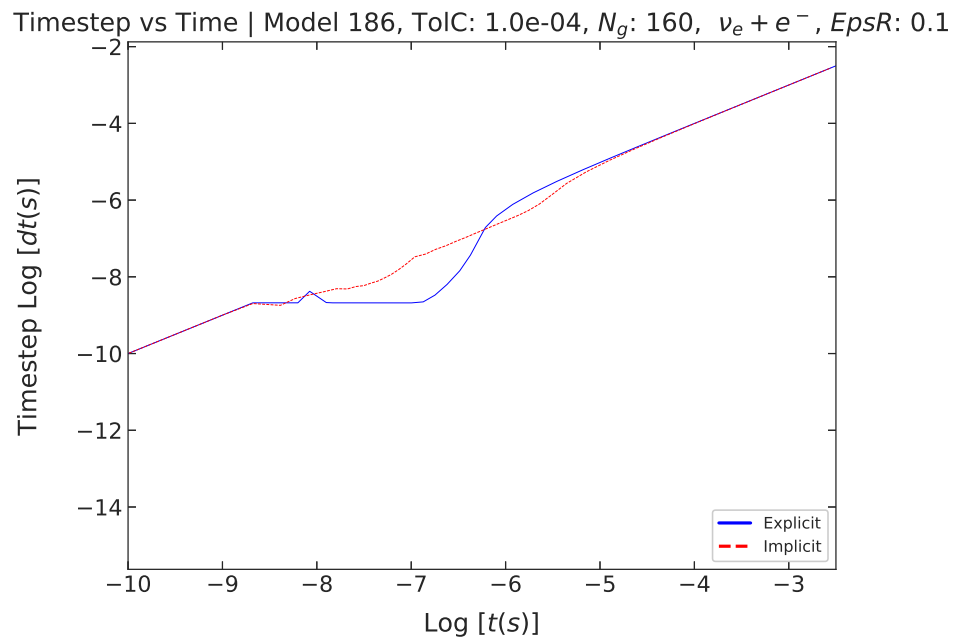


Figure 7.18: Timestep vs. time for Network Size 160.

7.1.7 Network Size 180

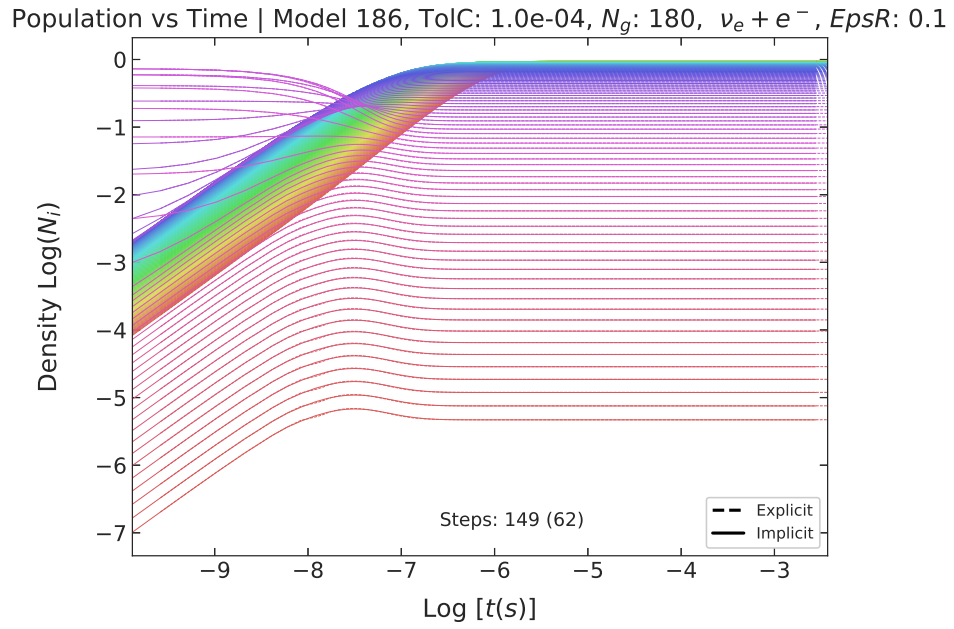


Figure 7.19: Population vs. time for Network Size 180.

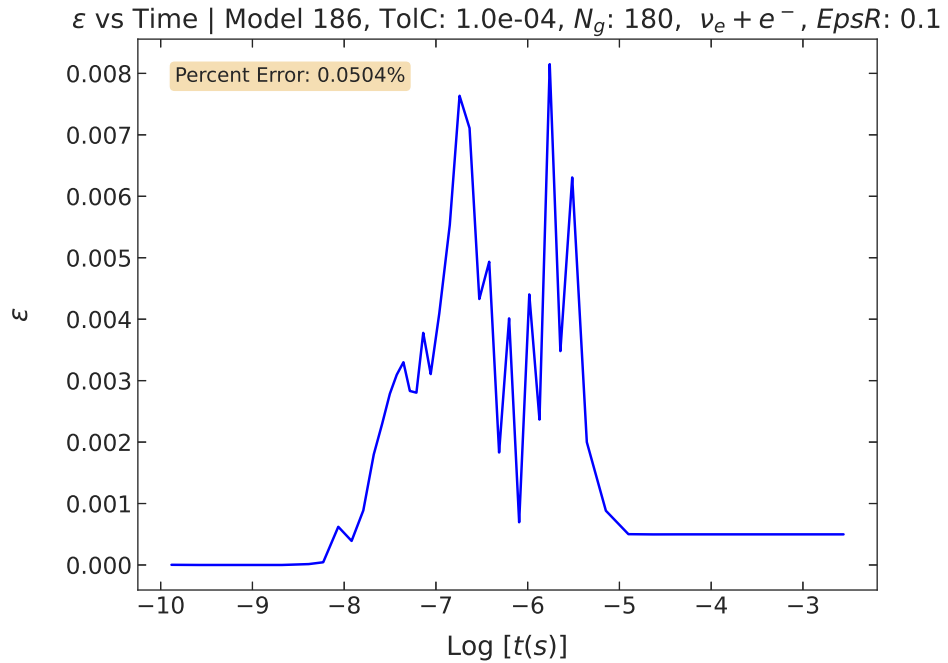


Figure 7.20: Epsilon vs. time for Network Size 180.

Additionally, we can display one of our cases (180 Size Network) in a heatmap to illustrate the differences in the scattering kernels.

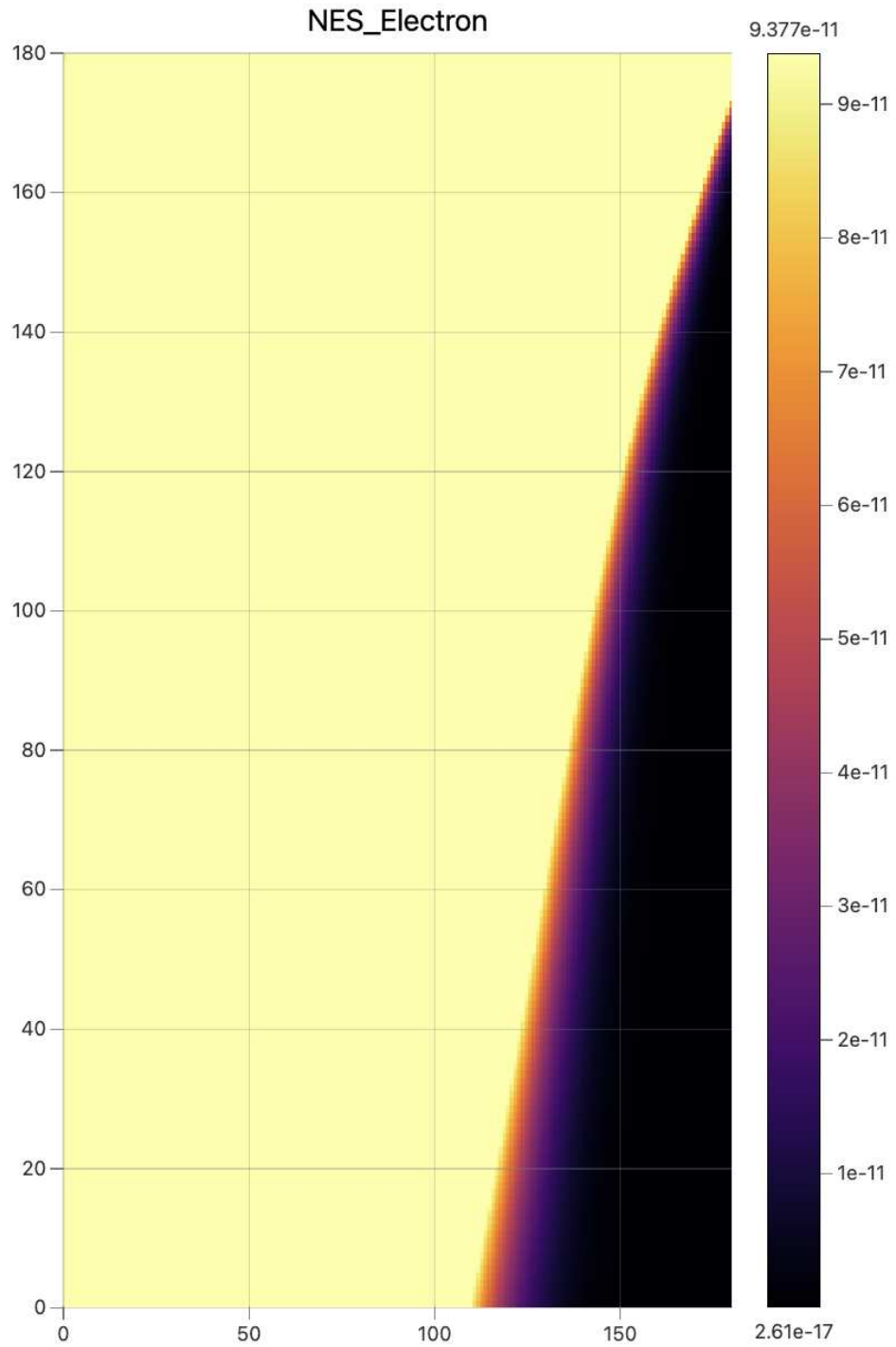


Figure 7.21: Heat map of Scattering Rates for a 180 Size Network

The error from these figures is tabulated into table 7.1.

Network Size	Explicit Steps	Backward Euler Steps	Error (%)
40	140	61	0.0503
50	142	62	0.0506
80	146	62	0.0538
100	147	62	0.0544
130	148	62	0.0521
160	148	62	0.0505
180	149	62	0.0504

Table 7.1: Comparison of Explicit Asymptotic and Backward Euler Steps with Error across Network Sizes.

It is observed that the number of steps required for both algorithms increases marginally as the network size increases. Importantly, the error remains approximately equal across the various network sizes, which indicates that the precision of the algorithms is not compromised as the networks scale in size while maintaining competitive time stepping.

We can compare the wall clock time for the explicit methods for these various sizes to the wall clock time for the backward Euler method.

Network Size	Time (Explicit Asymptotic)	Time (LU Solver)
40	211 ms	800 ms
50	319 ms	1220 ms
60	450 ms	1780 ms
70	611 ms	2484 ms
80	784 ms	3308 ms
90	984 ms	4298 ms
100	1208 ms	5751 ms
130	2049 ms	1028 ms
160	3078 ms	16997 ms
180	3873 ms	22931 ms

Table 7.2: Comparison of simulation times for explicit asymptotic and LU solver methods across network sizes.

Using table 7.2 we can derive our speed-up factors:

Network Size	Time (Backward Euler)	Time (Explicit Asymptotic)	Speed Up Factor
40	800 ms	211 ms	≈ 4
50	1220 ms	319 ms	≈ 4
60	1789 ms	450 ms	≈ 4
70	2484 ms	611 ms	≈ 4
80	3308 ms	784 ms	≈ 4.2
90	4298 ms	984 ms	≈ 4.33
100	5451 ms	1208 ms	≈ 4.5
130	10280 ms	2049 ms	≈ 5
160	16997 ms	3078 ms	≈ 5.5
180	22931 ms	3873 ms	≈ 6

Table 7.3: Comparison of computational time and speed up factor for different network sizes

While we used the LU solver in the figures presented in this chapter, we can also show that LU is the most consistent compared to other solvers used in backward Euler. It is important to note we use the LU solver in the backward Euler method for consistency.

Network Size	Time (QR)	Time (Cholesky)	Time (LU)
40	874 ms	2205 ms	800 ms
50	1328 ms	3463 ms	1220 ms
60	1895 ms	5431 ms	1789 ms
70	2647 ms	7998 ms	2484 ms
80	3461 ms	11207 ms	3308 ms
90	4501 ms	15173 ms	4298 ms
100	5714 ms	20044 ms	5451 ms
130	9643 ms	41092 ms	10280 ms
160	15604 ms	73308 ms	16997 ms
180	20646 ms	101942 ms	22931 ms

Table 7.4: Comparison of Simulation Times for Different Implicit Solvers across Network Sizes.

These results from tables 7.4 and 7.3 can be illustrated in the following figures:

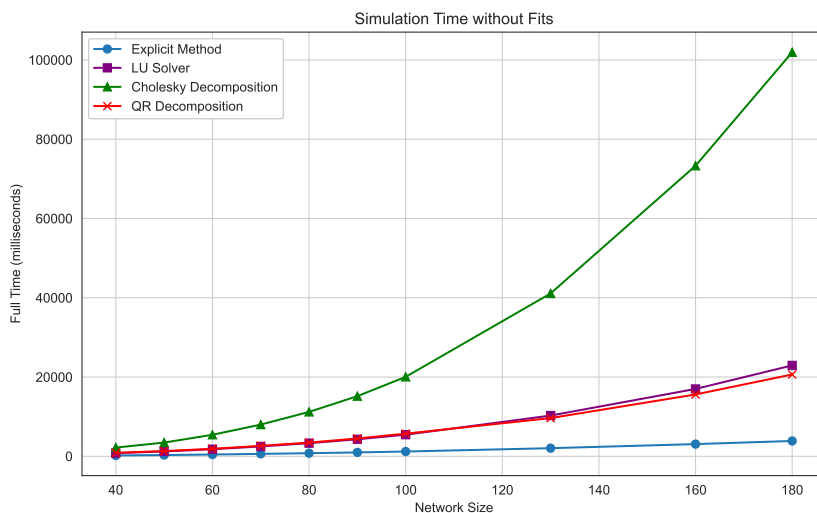


Figure 7.22: Full wall clock times. Includes times for different implicit solvers, along with polynomial fits to show the trends for each method.

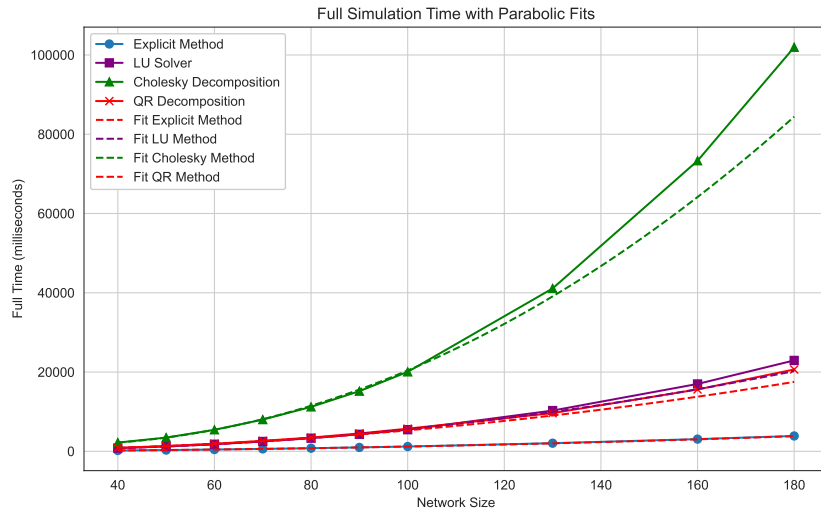


Figure 7.23: Full wall clock times from 7.22 with polynomial Fits for the first 3 points.

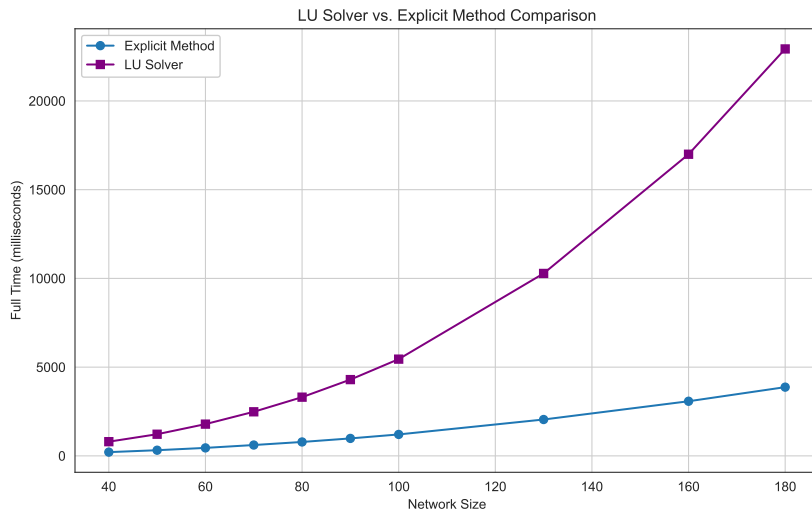


Figure 7.24: LU solver vs. explicit method comparison. LU solver is used in all calculations from 7.

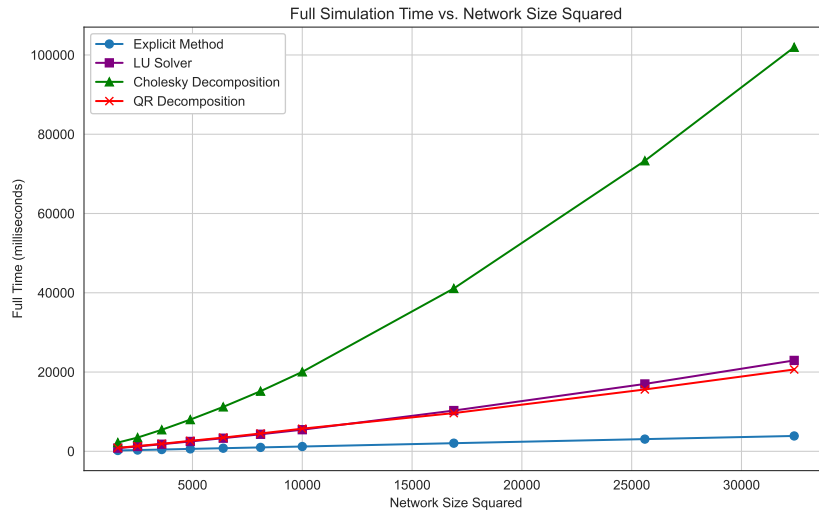


Figure 7.25: Full simulation time vs. network Size squared. This can represent the computational cost and general trends for Network Sizes.

For a larger network, while the number of steps does increase for computation, but the error stays very constant. This gives the strongest indication of the effectiveness of the methods used numerically, precisely the Explicit Asymptotic and Backward Euler methods, as depicted in table 7.1.

On the other hand, from tables 7.2 and 7.4, computation times for the LU solver increase quadratically with network size, sacrificing speed and reliability for larger networks. On the other hand, Cholesky solvers are computationally intensive, and they would be the most preferred in cases where numerical stability is of core importance, especially with the expanding size of the network.

The QR solver proves a viable alternative and outperforms the Cholesky method in smaller networks due to the balance in computation time and accuracy. It is seen that the computational times with respect to these solvers in Figures 7.22, 7.23, and 7.25 grow polynomially with respect to network size, especially for Cholesky and QR solvers. This trend underlines the significant aspect of choice of the appropriate solver for the network size and the computational load to be expected.

These results overall indicate the scaling calculations of the explicit algebraic algorithms, with network size have a much stronger advantage than those of the implicit methods, in both cases having a quadratic dependence on size. The scaling of the implicit method has a much steeper increase in computational costs, as indicated by a stronger curvature of its scaling parabola. This difference means that explicit methods are much more efficient for large networks. The likely reasons for such a higher curvature, or the increased increase in computational demand for implicit methods,

presumably lies in the enhanced complexity and an increased number of matrix inversions at each step, which act non-linearly on computation time. Such a result underscores the potential of algebraic explicit schemes in treating large-scale simulations, and it points in a straightforward way toward more computationally viable and scalable solutions for complex models of neutrino interaction.

Chapter 8

Conclusion

In our model of neutrino-electron scattering ($\nu_e + e^-$), we have shown that the explicit asymptotic approximation yields controlled errors and operates at speeds 1-3 times faster than traditional implicit methods (backward Euler) for networks with 40 neutrino energy bins. We have also shown that this efficiency increases for larger network sizes, demonstrating that these methods tend to scale better than implicit methods with network size. Given that explicit methods are generally more efficient per time step as they avoid the need for matrix inversions—the explicit asymptotic approach to neutrino transport presents a potential for enhanced speed and efficiency in many large-scale simulations.

We have given an introduction to scattering of various neutrino flavors using FENN from (ν_e), electron anti-neutrinos ($\bar{\nu}_e$), and muon/tau neutrinos ($\nu_{\mu,\tau}$) and their anti-particles ($\bar{\nu}_{\mu,\tau}$). In a full neutrino transport scheme these methods would be more systematically considered, and this lays groundwork for flexibility to include the full neutrino transport regimes in future work.

Additionally, we have verified that for larger networks these methods may scale better than implicit methods, because of the absence of matrix inversions. Therefore, we advocate for the use of algebraically stabilized explicit methods, capable of integrating realistic neutrino (and thermonuclear) networks within multidimensional hydrodynamics on current high-performance platforms.

The C++ codebase FENN: “Fast Explicit Neutrino Networks” will be released to the astrophysics community as documented open-source code for the rapid solution of large kinetic networks coupled to fluid dynamics, and to the broader scientific community as an open-source template for disciplines benefiting from the scalability and efficiency of algebraically stabilized explicit integration, especially when deployed on modern GPUs.

First introduced for Neutrino Networks by (Cole et al., 2024), these methods have shown potential performance in terms of effectively introducing far greater efficiency on GPU architectures than that exhibited by more traditional implicit approaches. The explicit methods show better performance when scaling the the neutrino networks, especially when ported to GPUs, because of efficient parallel processing. Most importantly, the ability to perform well for networks sizes that are larger than the standard 40 energy bins is paramount since it can be used to handle the large and complex nature of simulations with more efficiency. On the other hand, explicit methods architecture reduces dependence between computational elements and hence makes better use of the parallelism of the GPU.

Further work will be needed to optimize and port the FENN codebase to GPU environments. This move is expected to bring significant gains in performance, specifically with the processing speed and ability of handling larger datasets more effectively.

Additionally, alternative approximations such as Quasi Steady State (Guidry and Harris, 2013) and Partial Equilibrium (Guidry et al., 2013a) can be applied to certain time periods of the integration to best approximate the full integration. All the calculations done in this thesis run a full Explicit Asymptotic integration over the entire network, however we can better approximate this by using combinations of all three methods. In future work, we hope to address this as well by incorporating the already established methods for thermonuclear networks into the neutrino networks addressed by FENN.

Bibliography

- Brey, N. (2022). Analysis of controlled approximations for explicit integration of stiff thermonuclear networks. MS thesis, University of Tennessee; https://trace.tennessee.edu/utk_gradthes/9259. 1
- Bruenn, S. W. (1985). *App. J. Supp.*, 58:771. ix, 4, 7
- Chari, R., Cole, A., Guidry, M., Brey, N., Endeve, E., and Crowley, R. (2024). Advancing Astrophysical Models through FENN: Algebraically Stabilized Explicit Integration for Neutrino Electron Scattering in Stellar Explosions and Mergers. In *American Astronomical Society Meeting Abstracts*, volume 56 of *American Astronomical Society Meeting Abstracts*, page 135.05. 3, 16
- Chupryna, V. (2008). Explicit methods in the nuclear burning problem for supernova ia models. doctoral thesis, University of Tennessee; https://trace.tennessee.edu/utk_graddiss/484. 1
- Cole, A., Chari, R., Brey, N., Crowley, R., Guidry, M., and Endeve, E. (2024). Controlled and Parallelizable Approximation for Evolution Populations and Neutrino Distributions in Stellar Explosions and Mergers. In *American Astronomical Society Meeting Abstracts*, volume 56 of *American Astronomical Society Meeting Abstracts*, page 260.34. 82
- Feger, E. (2011). Evaluating explicit methods for solving astrophysical nuclear reaction networks. doctoral thesis, University of Tennessee; https://trace.tennessee.edu/utk_graddiss/1048. 1
- Gear, C. W. (1971). *Numerical Initial Value Problems in Ordinary Differential Equations*. Prentice Hall, Englewood Cliffs, N. J. 1
- Guidry, M., Brey, N., Billings, J., and Hix, R. (2023). A controlled approximation for solving large kinetic networks coupled to fluid dynamics. Manuscript in preparation. 1
- Guidry, M. W. (2012). *J. Comp. Phys.*, 231:5266. 1, 2, 3, 12

- Guidry, M. W. (2016). Efficient gpu acceleration for integrating large thermonuclear networks in astrophysics. In *EPJ Web of Conferences* **109**, page 06003. EDP Sciences. [1](#)
- Guidry, M. W., Billings, J. J., and Hix, W. R. (2013a). *Comput. Sci. Disc.*, 6:015003. [1](#), [82](#)
- Guidry, M. W., Budiardja, R., Feger, E., Billings, J. J., Hix, W. R., Messer, O. E. B., Roche, K. J., McMahon, E., and He, M. (2013b). *Comput. Sci. Disc.*, 6:015001. [1](#), [12](#), [29](#)
- Guidry, M. W. and Harris, J. A. (2013). *Comput. Sci. Disc.*, 6:015002. [1](#), [82](#)
- Haidar, A., Brock, B., Tomov, S., Guidry, M., Billings, J. J., Shyles, D., and Dongarra, J. (2016). Performance analysis and acceleration of explicit integration for large kinetic networks using batched gpu computations. IEEE High Performance Extreme Computing Conference, HPEC. [1](#)
- Haidar, A., Dong, T., Tomov, S., Luszczek, P., and Dongarra, J. (2015). Framework for batched and gpu-resident factorization algorithms to block householder transformations. ISC High Performance, Springer Frankfurt. [1](#)
- Hix, W. R. and Thielemann, F. K. (1999). *J. Comp. Appl. Math.*, 109:321. [29](#)
- Lackey-Stewart, A. (2020). An explicit asymptotic approach applied to neutrino-electron scattering in the neutrino transport problem. MS thesis, University of Tennessee; https://trace.tennessee.edu/utk_gradthes/5845. [8](#), [12](#), [19](#), [52](#)
- Lackey-Stewart, A., Chari, R., Cole, A., Brey, N., Gregory, K., Crowley, R., Guidry, M., and Endeve, E. (2024). Fast explicit solutions for neutrino-electron scattering: Explicit asymptotic methods. *Phys. Rev. D*, 109:103019. [3](#), [9](#), [11](#), [16](#), [28](#), [30](#), [52](#)
- Lambert, J. (1991). *Numerical Methods for Ordinary Differential Equations*. Wiley, New York. [1](#)
- Mezzacappa, A. and Bruenn, S. W. (1993). Stellar Core Collapse: A Boltzmann Treatment of Neutrino-Electron Scattering. *APJ*, 410:740. [7](#)
- Oran, E. and Boris, J. (2005). *Numerical Simulation of Reactive Flow*. Cambridge University Press, Cambridge. [1](#)
- Press, W., Teukolsky, S., Vetterling, W., and Flannery, B. (1992). *Numerical Recipes in Fortran*. Cambridge University Press, Cambridge. [1](#)
- Smit, J. M. and Cernohorsky, J. (1996). *A & A*, 311:347. [8](#)

Yueh, W. R. and Buchler, J. R. (1976). Scattering functions for neutrino transport. *Astrophysics and Space Science*, 39(2):429–435. [6](#)

Appendix A

Supernova Conditions

Model	r	ρ	T	Y_e
1	2.28E+07	1.00E+08	6.91E+09	0.4980
2	2.25E+07	1.02E+08	6.92E+09	0.4980
3	2.22E+07	1.04E+08	6.94E+09	0.4980
4	2.20E+07	1.06E+08	6.96E+09	0.4979
5	2.17E+07	1.07E+08	6.98E+09	0.4979
6	2.14E+07	1.09E+08	6.99E+09	0.4979
7	2.12E+07	1.11E+08	7.01E+09	0.4979
8	2.10E+07	1.13E+08	7.03E+09	0.4978
9	2.07E+07	1.14E+08	7.04E+09	0.4978
10	2.05E+07	1.16E+08	7.06E+09	0.4978
11	2.02E+07	1.18E+08	7.07E+09	0.4978
12	2.00E+07	1.20E+08	7.09E+09	0.4977
13	1.98E+07	1.22E+08	7.11E+09	0.4977
14	1.95E+07	1.24E+08	7.13E+09	0.4977
15	1.93E+07	1.26E+08	7.15E+09	0.4977
16	1.90E+07	1.29E+08	7.17E+09	0.4977
17	1.88E+07	1.30E+08	7.20E+09	0.4977
18	1.86E+07	1.33E+08	7.21E+09	0.4977

Continued on next page

Table A.1 – continued from previous page

Model	r	ρ	T	Y_e
19	1.84E+07	1.35E+08	7.28E+09	0.4976
20	1.82E+07	1.37E+08	7.21E+09	0.4976
21	1.80E+07	1.50E+08	7.41E+09	0.4976
22	1.77E+07	2.59E+08	8.60E+09	0.4976
23	1.75E+07	6.22E+08	1.16E+10	0.4976
24	1.73E+07	1.03E+09	1.46E+10	0.4975
25	1.71E+07	1.34E+09	1.52E+10	0.4968
26	1.69E+07	1.54E+09	1.54E+10	0.4961
27	1.67E+07	1.62E+09	1.56E+10	0.4951
28	1.65E+07	1.70E+09	1.60E+10	0.4937
29	1.63E+07	1.78E+09	1.62E+10	0.4918
30	1.61E+07	1.92E+09	1.64E+10	0.4902
31	1.59E+07	2.06E+09	1.65E+10	0.4882
32	1.57E+07	2.17E+09	1.68E+10	0.4852
33	1.55E+07	2.28E+09	1.72E+10	0.4819
34	1.53E+07	2.42E+09	1.74E+10	0.4794
35	1.51E+07	2.61E+09	1.75E+10	0.4757
36	1.50E+07	2.75E+09	1.78E+10	0.4709
37	1.48E+07	2.85E+09	1.82E+10	0.4659
38	1.46E+07	2.99E+09	1.86E+10	0.4612
39	1.44E+07	3.20E+09	1.87E+10	0.4557
40	1.42E+07	3.41E+09	1.90E+10	0.4492
41	1.40E+07	3.51E+09	1.96E+10	0.4422
42	1.39E+07	3.65E+09	2.00E+10	0.4347
43	1.37E+07	3.85E+09	2.04E+10	0.4274
44	1.35E+07	4.04E+09	2.08E+10	0.4193
45	1.34E+07	4.19E+09	2.14E+10	0.4104
46	1.32E+07	4.29E+09	2.23E+10	0.4012
47	1.30E+07	4.42E+09	2.31E+10	0.3927
48	1.29E+07	4.62E+09	2.37E+10	0.3837

Continued on next page

Table A.1 – continued from previous page

Model	r	ρ	T	Y_e
49	1.27E+07	4.77E+09	2.45E+10	0.3748
50	1.25E+07	4.89E+09	2.54E+10	0.3661
51	1.24E+07	5.02E+09	2.63E+10	0.3581
52	1.22E+07	5.20E+09	2.70E+10	0.3502
53	1.21E+07	5.40E+09	2.76E+10	0.3427
54	1.19E+07	5.60E+09	2.83E+10	0.3358
55	1.18E+07	5.81E+09	2.89E+10	0.3293
56	1.16E+07	6.02E+09	2.96E+10	0.3233
57	1.15E+07	6.23E+09	3.02E+10	0.3178
58	1.13E+07	6.44E+09	3.09E+10	0.3135
59	1.12E+07	6.66E+09	3.16E+10	0.3095
60	1.10E+07	6.94E+09	3.21E+10	0.3055
61	1.09E+07	7.25E+09	3.26E+10	0.3018
62	1.07E+07	7.56E+09	3.31E+10	0.2986
63	1.06E+07	7.86E+09	3.37E+10	0.2962
64	1.05E+07	8.20E+09	3.42E+10	0.2939
65	1.03E+07	8.57E+09	3.47E+10	0.2915
66	1.02E+07	8.99E+09	3.51E+10	0.2888
67	1.00E+07	9.43E+09	3.56E+10	0.2865
68	9.92E+06	9.89E+09	3.61E+10	0.2845
69	9.79E+06	1.04E+10	3.66E+10	0.2829
70	9.66E+06	1.08E+10	3.71E+10	0.2811
71	9.53E+06	1.14E+10	3.76E+10	0.2790
72	9.40E+06	1.20E+10	3.80E+10	0.2766
73	9.28E+06	1.27E+10	3.84E+10	0.2739
74	9.15E+06	1.34E+10	3.88E+10	0.2709
75	9.03E+06	1.43E+10	3.92E+10	0.2677
76	8.90E+06	1.52E+10	3.96E+10	0.2643
77	8.78E+06	1.61E+10	4.00E+10	0.2606
78	8.66E+06	1.72E+10	4.03E+10	0.2568

Continued on next page

Table A.1 – continued from previous page

Model	r	ρ	T	Y_e
79	8.54E+06	1.84E+10	4.07E+10	0.2530
80	8.43E+06	1.96E+10	4.10E+10	0.2490
81	8.31E+06	2.10E+10	4.14E+10	0.2451
82	8.20E+06	2.25E+10	4.18E+10	0.2409
83	8.08E+06	2.41E+10	4.22E+10	0.2367
84	7.97E+06	2.59E+10	4.25E+10	0.2327
85	7.86E+06	2.78E+10	4.29E+10	0.2286
86	7.75E+06	2.99E+10	4.33E+10	0.2247
87	7.64E+06	3.22E+10	4.37E+10	0.2206
88	7.53E+06	3.46E+10	4.41E+10	0.2167
89	7.42E+06	3.73E+10	4.45E+10	0.2127
90	7.32E+06	4.03E+10	4.50E+10	0.2089
91	7.21E+06	4.34E+10	4.54E+10	0.2053
92	7.11E+06	4.69E+10	4.59E+10	0.2017
93	7.01E+06	5.06E+10	4.64E+10	0.1982
94	6.91E+06	5.47E+10	4.70E+10	0.1947
95	6.81E+06	5.92E+10	4.75E+10	0.1912
96	6.71E+06	6.40E+10	4.81E+10	0.1881
97	6.61E+06	6.93E+10	4.87E+10	0.1851
98	6.51E+06	7.50E+10	4.93E+10	0.1820
99	6.42E+06	8.12E+10	5.00E+10	0.1789
100	6.32E+06	8.80E+10	5.06E+10	0.1762
101	6.23E+06	9.53E+10	5.14E+10	0.1737
102	6.13E+06	1.04E+11	5.21E+10	0.1718
103	6.04E+06	1.12E+11	5.28E+10	0.1692
104	5.95E+06	1.22E+11	5.36E+10	0.1667
105	5.86E+06	1.33E+11	5.45E+10	0.1641
106	5.77E+06	1.44E+11	5.53E+10	0.1615
107	5.68E+06	1.57E+11	5.62E+10	0.1589
108	5.59E+06	1.70E+11	5.71E+10	0.1573

Continued on next page

Table A.1 – continued from previous page

Model	r	ρ	T	Y_e
109	5.51E+06	1.85E+11	5.81E+10	0.1557
110	5.42E+06	2.01E+11	5.91E+10	0.1540
111	5.34E+06	2.18E+11	6.02E+10	0.1524
112	5.25E+06	2.38E+11	6.13E+10	0.1507
113	5.17E+06	2.58E+11	6.24E+10	0.1489
114	5.08E+06	2.81E+11	6.36E+10	0.1473
115	5.00E+06	3.05E+11	6.48E+10	0.1464
116	4.92E+06	3.31E+11	6.61E+10	0.1453
117	4.84E+06	3.60E+11	6.75E+10	0.1441
118	4.76E+06	3.91E+11	6.89E+10	0.1429
119	4.69E+06	4.25E+11	7.03E+10	0.1416
120	4.61E+06	4.62E+11	7.18E+10	0.1408
121	4.53E+06	5.01E+11	7.34E+10	0.1402
122	4.46E+06	5.44E+11	7.50E+10	0.1397
123	4.38E+06	5.90E+11	7.66E+10	0.1390
124	4.31E+06	6.41E+11	7.83E+10	0.1382
125	4.23E+06	6.97E+11	8.01E+10	0.1375
126	4.16E+06	7.56E+11	8.19E+10	0.1374
127	4.09E+06	8.20E+11	8.38E+10	0.1370
128	4.02E+06	8.91E+11	8.57E+10	0.1365
129	3.95E+06	9.68E+11	8.77E+10	0.1358
130	3.88E+06	1.05E+12	8.97E+10	0.1352
131	3.81E+06	1.14E+12	9.17E+10	0.1350
132	3.74E+06	1.24E+12	9.38E+10	0.1347
133	3.67E+06	1.35E+12	9.60E+10	0.1341
134	3.61E+06	1.47E+12	9.82E+10	0.1333
135	3.54E+06	1.60E+12	1.00E+11	0.1325
136	3.48E+06	1.74E+12	1.03E+11	0.1322
137	3.41E+06	1.90E+12	1.05E+11	0.1317
138	3.35E+06	2.07E+12	1.08E+11	0.1310

Continued on next page

Table A.1 – continued from previous page

Model	r	ρ	T	Y_e
139	3.28E+06	2.26E+12	1.10E+11	0.1300
140	3.22E+06	2.47E+12	1.12E+11	0.1290
141	3.16E+06	2.70E+12	1.15E+11	0.1286
142	3.10E+06	2.95E+12	1.18E+11	0.1281
143	3.04E+06	3.23E+12	1.21E+11	0.1274
144	2.98E+06	3.53E+12	1.24E+11	0.1267
145	2.92E+06	3.86E+12	1.26E+11	0.1260
146	2.86E+06	4.22E+12	1.30E+11	0.1260
147	2.80E+06	4.61E+12	1.33E+11	0.1261
148	2.74E+06	5.03E+12	1.36E+11	0.1261
149	2.68E+06	5.49E+12	1.40E+11	0.1262
150	2.63E+06	5.98E+12	1.44E+11	0.1269
151	2.57E+06	6.50E+12	1.48E+11	0.1280
152	2.52E+06	7.06E+12	1.53E+11	0.1291
153	2.46E+06	7.67E+12	1.57E+11	0.1302
154	2.41E+06	8.31E+12	1.62E+11	0.1321
155	2.35E+06	8.98E+12	1.67E+11	0.1341
156	2.30E+06	9.70E+12	1.72E+11	0.1361
157	2.25E+06	1.05E+13	1.78E+11	0.1379
158	2.20E+06	1.13E+13	1.84E+11	0.1407
159	2.14E+06	1.22E+13	1.89E+11	0.1438
160	2.09E+06	1.31E+13	1.95E+11	0.1468
161	2.04E+06	1.41E+13	2.01E+11	0.1497
162	1.99E+06	1.51E+13	2.07E+11	0.1535
163	1.94E+06	1.62E+13	2.13E+11	0.1571
164	1.89E+06	1.74E+13	2.20E+11	0.1606
165	1.85E+06	1.87E+13	2.26E+11	0.1648
166	1.80E+06	2.00E+13	2.32E+11	0.1696
167	1.75E+06	2.15E+13	2.39E+11	0.1746
168	1.70E+06	2.30E+13	2.45E+11	0.1794

Continued on next page

Table A.1 – continued from previous page

Model	r	ρ	T	Y_e
169	1.66E+06	2.47E+13	2.52E+11	0.1849
170	1.61E+06	2.65E+13	2.58E+11	0.1914
171	1.57E+06	2.84E+13	2.64E+11	0.1979
172	1.52E+06	3.04E+13	2.70E+11	0.2054
173	1.48E+06	3.26E+13	2.76E+11	0.2133
174	1.43E+06	3.50E+13	2.82E+11	0.2218
175	1.39E+06	3.76E+13	2.86E+11	0.2317
176	1.35E+06	4.04E+13	2.91E+11	0.2422
177	1.30E+06	4.34E+13	2.94E+11	0.2537
178	1.26E+06	4.69E+13	2.97E+11	0.2656
179	1.22E+06	5.09E+13	2.98E+11	0.2775
180	1.18E+06	5.57E+13	2.98E+11	0.2888
181	1.14E+06	6.19E+13	2.95E+11	0.2976
182	1.10E+06	7.01E+13	2.90E+11	0.3023
183	1.06E+06	8.19E+13	2.81E+11	0.3002
184	1.02E+06	9.93E+13	2.68E+11	0.2902
185	9.77E+05	1.23E+14	2.51E+11	0.2747
186	9.39E+05	1.52E+14	2.30E+11	0.2599
187	9.00E+05	1.81E+14	2.09E+11	0.2490
188	8.62E+05	2.08E+14	1.88E+11	0.2422
189	8.24E+05	2.32E+14	1.70E+11	0.2387
190	7.87E+05	2.52E+14	1.56E+11	0.2376
191	7.50E+05	2.70E+14	1.45E+11	0.2382
192	7.14E+05	2.86E+14	1.38E+11	0.2397
193	6.78E+05	2.99E+14	1.34E+11	0.2421
194	6.42E+05	3.12E+14	1.32E+11	0.2446
195	6.06E+05	3.22E+14	1.32E+11	0.2471
196	5.72E+05	3.32E+14	1.33E+11	0.2493
197	5.37E+05	3.42E+14	1.34E+11	0.2511
198	5.03E+05	3.51E+14	1.35E+11	0.2522

Continued on next page

Table A.1 – continued from previous page

Model	r	ρ	T	Y_e
199	4.69E+05	3.59E+14	1.34E+11	0.2529
200	4.35E+05	3.67E+14	1.32E+11	0.2533
201	4.02E+05	3.74E+14	1.30E+11	0.2534
202	3.69E+05	3.81E+14	1.29E+11	0.2533
203	3.36E+05	3.87E+14	1.29E+11	0.2532
204	3.04E+05	3.92E+14	1.28E+11	0.2530
205	2.72E+05	3.97E+14	1.28E+11	0.2528
206	2.41E+05	4.01E+14	1.28E+11	0.2526
207	2.10E+05	4.04E+14	1.27E+11	0.2524
208	1.79E+05	4.07E+14	1.27E+11	0.2522
209	1.48E+05	4.10E+14	1.26E+11	0.2521
210	1.18E+05	4.12E+14	1.26E+11	0.2520
211	8.79E+04	4.13E+14	1.26E+11	0.2519
212	5.83E+04	4.14E+14	1.26E+11	0.2518
213	2.90E+04	4.15E+14	1.26E+11	0.2518

Centers 1-10	Centers 11-20	Centers 21-30	Centers 31-40	Centers 41-50
1	3.2028	10.258	32.855	105.23
1.1234	3.5982	11.525	36.911	118.22
1.2621	4.0424	12.947	41.468	132.81
1.4179	4.5415	14.546	46.587	149.21
1.593	5.1021	16.341	52.338	167.63
1.7896	5.732	18.359	58.799	188.32
2.0106	6.4396	20.625	66.058	211.57
2.2588	7.2345	23.171	74.213	237.69
2.5376	8.1276	26.031	83.374	267.03
2.8509	9.131	29.245	93.667	300

Table A.2: Energy Grid for a 50-Species Network.

Widths 1-10	Widths 11-20	Widths 21-30	Widths 31-40	Widths 41-50
1	0.35194	1.1272	3.6103	11.563
0.12345	0.39539	1.2664	4.056	12.991
0.13869	0.4442	1.4227	4.5567	14.594
0.15581	0.49903	1.5983	5.1192	16.396
0.17504	0.56064	1.7956	5.7511	18.42
0.19665	0.62985	2.0173	6.4611	20.694
0.22093	0.70761	2.2663	7.2587	23.249
0.2482	0.79496	2.5461	8.1548	26.119
0.27885	0.8931	2.8604	9.1615	29.343
0.31327	1.0033	3.2136	10.293	32.965

Table A.3: Energy Widths for a 50-Species Network.

Vita

Raghav Chari was born in Charlottesville, Virginia, in September of 2003. He graduated from Panther Creek High School in 2021. During his high school years, he concurrently engaged in research at UNC Greensboro, focusing on “Be” stars. In 2021, he enrolled in the University of Tennessee, Knoxville’s Department of Physics & Astronomy, where he began his pursuit of a Bachelor of Science in Physics. In his third year, he was accepted into the College Scholars program, through which he is also pursuing a Bachelor of Arts in the Philosophy of Physics. Throughout his undergraduate career, Raghav has been actively involved in computational astrophysics research. He has also served as a Teaching Assistant for undergraduate physics courses. Following his graduation, he plans to pursue a Ph.D. in Physics.